Strong-field Breit-Wheeler pair production in short laser pulses

Inaugural-Dissertation

zur Erlangung des Doktorgrades
der Mathematisch-Naturwissenschaftlichen Fakultät
der Heinrich-Heine-Universität Düsseldorf

vorgelegt von

Martin Josef Alexander Jansen
aus Neuss

Düsseldorf, Januar 2017

aus dem Institut für Theoretische Physik I
der Heinrich-Heine-Universität Düsseldorf

Gedruckt mit der Genehmigung der
Mathematisch-Naturwissenschaftlichen Fakultät der
Heinrich-Heine-Universität Düsseldorf

Referent: Prof. Dr. Dr. Carsten Müller

Koreferent: Prof. Dr. Reinhold Egger

Tag der mündlichen Prüfung: 10.02.2017

Abstract

The current progress in high-intensity laser technology provides experimental access to unprecedented high field strengths and thus allows to explore the interaction between light and matter in new regimes. Presently emerging facilities, like the Extreme Light Infrastructure, offer prospects to probe scenarios where the theory of quantum electrodynamics (QED) predicts the occurrence of novel effects. Despite being one of the best established physical theories today, QED is still awaiting systematic experimental verification in time-dependent fields of high strength. This could be achieved by dedicated experiments aiming at a variety of strong-field phenomena, like the Breit-Wheeler process.

Predicted by Breit and Wheeler in 1934, the collision of two energetic photons can lead to the creation of an electron-positron pair. Early theoretical studies have shown that upon application of a coherent light source, the strong-field Breit-Wheeler (SFBW) process can be induced as a multiphoton reaction. In these studies, the laser field was treated as an infinitely extended plane wave. However, employing modern high-intensity lasers, the highest intensities are reached in very short pulses, comprising only few optical cycles. Therefore, the question arises to which extent the process is affected by the properties of the laser field, in particular by the finite duration and the spectral composition.

In this thesis, we study the SFBW process in short laser pulses and acquire answers to these questions. Our approach is based on detailed S-matrix calculations in the framework of laser-dressed QED, allowing us to obtain numerical predictions for the process probability in various parameter constellations. The analysis of the corresponding results has given rise to general insights about the process, which shall be presented in detail. In particular, a new quantitative model for multiphoton processes in short laser pulses is developed, which clearly reveals and explains the connection between the properties of the laser field and the energy spectrum of the produced particles.

Moreover, focusing on the quantum nature of the process, the relevance of interferences shall be investigated. Following the multiphoton approach, distinct interference effects arising in the particle spectra can be detected and understood, revealing a characteristic dependence on the carrier-envelope phase of the laser pulse. Besides, further expanding our model approach allows us to examine general properties of multiphoton-interference processes driven by pulsed laser fields with a continuous frequency spectrum.

In addition, the influence of the particle's spin on the SFBW process is inspected by way of comparison between predictions from full Dirac theory and scalar theory, respectively. Facilitating a simplified theoretical treatment, the scalar case can be regarded as an approximation to the Dirac case. Our study examines various regimes and includes an intuitive approach to the underlying principle. This way, we also gain information on the applicability of the spinless approximation.

Finally, we regard an extended scenario involving a second laser pulse which arrives with a variable delay. The contributions from both pulses to the pair-creation process induce pronounced interference effects, which are intrinsically different to the multiphoton interferences. Inspecting the influence of the delay time, further fundamental properties of the SFBW process can be analyzed and understood from a complementary perspective.

The present study enhances the understanding of several aspects inherent to the SFBW process. Furthermore, some of our concepts and insights can be applied to other strong-field phenomena, such as nonlinear Compton scattering, as well.

Zusammenfassung

Der aktuelle Fortschritt in der Hochintensitätslasertechnologie ermöglicht sehr hohe Feldstärken und erlaubt somit die Wechselwirkung von Licht und Materie in neuen Regimen zu untersuchen. Gegenwärtig entstehende Forschungseinrichtungen, wie die *Extreme Light Infrastructre*, eröffnen die Aussicht auf Experimente, in denen die Quantenelektrodynamik (QED) das Auftreten neuartiger Effekte vorhersagt. Obwohl sie eine der bestetablierten Theorien der heutigen Physik ist, steht bei zeitabhängigen Feldern hoher Feldstärke eine systematische experimentelle Überprüfung noch aus. Diese könnte durch spezielle Experimente erbracht werden, die auf eine Vielzahl von Starkfeldphänomenen abzielen, wie zum Beispiel den Breit-Wheeler Prozess.

Wie schon 1934 durch Breit und Wheeler vorhergesagt, kann die Kollision zweier energetischer Photonen zu der Erzeugung eines Elektron-Positron-Paares führen. Frühe theoretische Studien haben gezeigt, dass, sofern eine kohärente Lichtquelle beteiligt ist, der Breit-Wheeler Prozess in starken Feldern (der SFBW Prozess) als Multiphotonenreaktion stattfinden kann. In diesen Studien war das Laserfeld als eine unendlich ausgedehnte, ebene Welle beschrieben. In modernen, hoch intensiven Lasern wird die höchste Intensität jedoch in sehr kurzen Pulsen erzeugt, die nur wenige optische Zyklen umfassen. Es stellt sich daher die Frage, in welchem Maß der Prozess von den Eigenschaften des Laserfeldes beeinflusst wird, insbesondere von der endlichen Länge und der spektralen Zusammensetzung.

In dieser Dissertation studieren wir den SFBW Prozess in kurzen Laserpulsen und erarbeiten Antworten zu diesen Fragen. Unser Ansatz basiert auf detaillierten S-Matrix-Rechnungen im Rahmen der Starkfeld-QED. Dieser ermöglicht es uns, numerische Vorhersagen für die Prozesswahrscheinlichkeit in verschiedenen Parameterkonstellationen zu erhalten. Die Analyse der zugehörigen Ergebnisse hat allgemeine Einblicke in den Prozess ermöglicht, welche ausführlich präsentiert werden. Insbesondere wird ein neues quantitatives Modell für Multiphotonenprozesse in kurzen Laserpulsen entwickelt, welches die Verbindung zwischen den Eigenschaften des Laserfeldes und dem Energiespektrum der erzeugten Teilchen klar aufzeigt und erklärt.

Zudem wird mit Blick auf die quantenmechanischen Eigenschaften des Prozesses die Bedeutung von Interferenzen untersucht. Dem Multiphotonenansatz folgend können ausgeprägte Interferenzeffekte in den Teilchenspektren detektiert und verstanden werden, wobei eine charakteristische Abhängigkeit von der Phasenlage zwischen der Trägerfrequenz und der Einhüllenden des Laserpulses (*carrier-envelope phase*, CEP) zu Tage tritt. Außerdem ermöglicht eine Erweiterung unseres Modellansatzes die Untersuchung allgemeiner Eigenschaften von Multiphotoneninterferenzprozessen, wie sie durch gepulste Laserfelder mit kontinuierlichen Frequenzspektren induziert werden.

Weitergehend wird der Einfluss des Teilchenspins in dem SFBW Prozess anhand eines Vergleiches von Vorhersagen aus der umfangreicheren Theorie nach Dirac und der skalaren Theorie untersucht. Da sie eine vereinfachte theoretische Behandlung ermöglicht, wird die skalare Theorie zuweilen als eine Näherung für die Dirac'sche Theorie verwendet. Wir betrachten verschiedene Regime und entwickeln einen intuitiven Zugang zu dem zugrunde liegenden Prinzip. Auf diesem Weg erhalten wir zudem Informationen über die Anwendbarkeit dieser Näherung.

Schließlich analysieren wir ein erweitertes Szenario, in dem ein zweiter Laserpuls mit einer

variablen Zeitverzögerung Berücksichtigung findet. Die Beiträge der beiden Pulse zu dem Paarerzeugungsprozess induzieren deutliche Interferenzeffekte, welche sich fundamental von den Multiphotoneninterferenzen unterscheiden. Indem wir die Abhängigkeit von der Zeitverzögerung untersuchen, können wir weitere grundlegende Eigenschaften des SFBW Prozesses studieren und aus einer komplementären Perspektive verstehen.
Diese Arbeit erweitert das Verständnis einiger Aspekte des SFBW Prozesses. Darüber hinaus können manche unserer Konzepte und Erkenntnisse auch auf andere Phänomene in starken Laserfeldern, wie z.B. die nichtlineare Comptonstreuung, übertragen werden.

Eidesstattliche Versicherung

Ich versichere an Eides Statt, dass die Dissertation von mir selbstständig und ohne unzulässige fremde Hilfe unter Beachtung der “Grundsätze zur Sicherung guter wissenschaftlicher Praxis an der Heinrich-Heine-Universität Düsseldorf” erstellt worden ist.

Hiermit erkläre ich, dass ich bisher weder diese noch eine andere Dissertationsschrift einer anderen Fakultät vorgelegt habe.

Düsseldorf,

Contents

1 Introduction **1**
- 1.1 Overview and motivation . . . 1
- 1.2 Structure of this thesis and my contribution . . . 4
- 1.3 Acknowledgments . . . 5
- 1.4 Publications . . . 5

2 Theoretical Framework **7**
- 2.1 Preparations . . . 7
  - 2.1.1 Charged particles in a strong laser field . . . 7
    - 2.1.1.1 Classical description . . . 7
    - 2.1.1.2 Quantum description . . . 8
  - 2.1.2 Plane-wave laser fields of finite extent . . . 9
  - 2.1.3 Gamma quantum . . . 10
- 2.2 Strong-Field Breit-Wheeler pair production of scalar particles . . . 10
  - 2.2.1 The pair-creation probability . . . 10
  - 2.2.2 Kinematical constraints . . . 14
  - 2.2.3 Energy-momentum balance . . . 15
  - 2.2.4 Differential probabilities . . . 17
- 2.3 Production of Dirac particles . . . 18
  - 2.3.1 The pair-production probability . . . 18
  - 2.3.2 The spinor properties . . . 19

3 Modeling the particle spectrum **21**
- 3.1 Introduction . . . 21
- 3.2 Concepts from the multichromatic case . . . 21
  - 3.2.1 Pair-creation amplitude . . . 21
  - 3.2.2 Probabilities and interferences . . . 22
- 3.3 P model . . . 24
  - 3.3.1 Definitions . . . 24
  - 3.3.2 Outline . . . 25
  - 3.3.3 Photon-finding probability . . . 26
- 3.4 Numerical examples . . . 28
  - 3.4.1 Multiphoton processes . . . 28
  - 3.4.2 Emission processes . . . 29
- 3.5 Conclusion . . . 31

4 CEP and interference effects **33**
- 4.1 CEP effects: Analytical approach . . . 33
  - 4.1.1 Continuous generalization of the multichromatic field . . . 33
  - 4.1.2 CEP signatures in the pulse spectrum . . . 34
  - 4.1.3 CEP effects in the energy spectra of the produced particles . . . 35
- 4.2 CEP and interference effects: Numerical examples . . . 35
  - 4.2.1 Detailed examples . . . 35

4.2.2 Further details on the interference terms 37
4.3 Interference processes driven by continuous spectra 38
4.3.1 S model 38
4.3.2 Self-interferences 39
4.3.3 Interferences in bichromatic fields of finite spectral width 40
4.4 Conclusion 42

5 Spin Effects **43**
5.1 Multiphoton processes in monochromatic fields 43
5.2 Spin effects in short pulses 46
5.2.1 Above the one-photon threshold 47
5.2.2 Just below the one-photon threshold 48
5.2.3 Deeply below the one-photon threshold 53
5.3 Summary and conclusion 56

6 Two consecutive pulses **59**
6.1 The pair-creation probability 59
6.1.1 Scalar particles in the field of two consecutive pulses 59
6.1.2 S-matrix amplitude 60
6.2 General properties 62
6.2.1 Identifying contributions from the individual pulses 62
6.2.2 The phase factor 63
6.2.3 Conclusion 64
6.3 Two-pulse interference 65
6.3.1 Two identical pulses 65
6.3.1.1 Angular distributions 65
6.3.1.2 Momentum spectra 68
6.3.1.3 Total probability 69
6.3.2 Different pulses 73
6.3.2.1 Angular distributions 73
6.3.2.2 Momentum spectra 76
6.3.2.3 Total probability 76
6.4 Conclusion 77

7 Conclusion **79**

A Appendix **81**
A.1 Classical motion of a charged particle in a laser field 81
A.2 Dirac γ matrices 82
A.3 Spinors 82
A.4 Trace technique 84
A.4.1 General concept 84
A.4.2 Traces over products of γ matrices 85
A.4.3 Refinement 85
A.4.4 Explicit application to our calculation 86
A.4.5 Explicit traces 87
A.5 Dealing with squares of δ functions 87
A.5.1 Standard treatment 87
A.5.2 Coordinate transforms 88

A.5.3 A first attempt 88
A.5.4 Treating the gamma quantum as a wave packet 89
A.6 Properties of the pulse shape 91
A.7 Fourier expanding the integrals 92

Bibliography **95**

1 Introduction

1.1 Overview and motivation

The theory of quantum electrodynamics (QED) is one of the best-established theories in today's physics. For example, energy levels in atomic physics could be predicted very accurately. However, for high electromagnetic field intensities, it is not so well tested. Seeking for fundamental verification, presently emerging experimental facilities can probe the area of strong-field QED aiming at a variety of interesting effects.
One the most intriguing predictions of QED is the creation of electron-positron pairs due to the collision of two high-energy photons. Predicted by Breit and Wheeler [BW34] in 1934, this process contradicts the superposition principle of classical electrodynamics. Instead, the two photons annihilate and are converted into matter, albeit with a small probability.
Shortly after the invention of the laser in 1960, theoreticians began to investigate the situation when a strong laser field collides with high-energy photons [Rei62, NNR65]. In analogy to processes known from atomic physics, they found that the strong-field Breit-Wheeler (SFBW) pair-creation process can be induced as a multiphoton reaction, i.e. several laser photons can participate and thus reduce the required energy per individual photon. Symbolically, the process can be written as

$$\omega_\gamma + n\omega \to e^+e^- \,, \tag{1.1}$$

where ω_γ denotes the frequency of the high-energy (gamma) photon, which collides with n laser photons of frequency ω.
A corresponding experiment could first be conducted in 1997 at the Stanford Linear Accelerator Center (SLAC) [BFHS+97]. There, a highly energetic electron beam (47 GeV) was brought into collision with an optical laser pulse ($\omega = 2.35$ eV) with an intensity on the order of $10^{18}\mathrm{W/cm}^2$ and picosecond duration. The produced positrons were attributed to a two-stage process: First, one laser photon was scattered off the electron beam and produced a high-energy photon ($\omega_\gamma \approx 29$ GeV) by means of Compton scattering. Next, this Compton photon collided with (on average) five laser photons, leading to electron-positron pairs due to the multiphoton Breit-Wheeler process. The experimental results were found in agreement with theoretical results obtained from strong-field QED [HMK10].
The successful experiment and the ongoing progress of high-intensity laser technology has triggered substantial theoretical effort with regard to strong-field QED phenomena; see [EKK09, DPMHK12] for a review. It is worth mentioning that the SLAC experiment has probed only one distinct case in the broad parameter space inherent to the SFBW process. Theoretical studies have predicted that the process properties exhibit pronounced qualitative differences in different regimes, which shall be briefly addressed in the following.
In the early theoretical investigations of the SFBW process [Rei62, NR64a, NR64b, NNR65, NR67, Rit85], the laser field was treated as an infinitely extended, monochromatic field (IPW). Following the historical path, the different interaction regimes can broadly be distinguished by means of the Lorentz-invariant field-strength parameter $\xi = |eA_0|/m$, where A_0 denotes the amplitude of the vector potential describing the IPW laser field.[1]

[1] A precise definition will be given in Sec. 2.1.2. Throughout this work, m and e denote the mass and

For $\xi \ll 1$, the probability of the process involving n laser photons scales as ξ^{2n}, giving particular weight to the process requiring the smallest possible photon number. In this regime, the effect of the laser field on the produced particles is (negligibly) small, and the process could in principle be treated theoretically by pursuing a perturbative approach. The minimum number of necessary laser photons can be deduced from the invariant threshold condition

$$n\omega\omega_\gamma > m^2 \,, \tag{1.2}$$

which follows from the energy-momentum balance associated with reaction (1.1). Throughout this work, the gamma quantum is assumed to collide head-on with the laser beam. For the SLAC experiment, this condition implies that at least $n = 4$ laser photons are required. However, the experiment was conducted with sufficiently high field strength ($\xi \approx 0.5$) to induce non-perturbative behavior. As we will discuss in detail, the impact of the laser field on the classical dynamics of the charged particles increases the threshold energy. In fact, this effect was strong enough to close the leading-order production channel with four photons, such that at least $n = 5$ photons had to be absorbed [Rei09, HMK10]. For slightly higher laser intensities with $\xi \lesssim 1$, the produced pairs can in principle still be understood to be created due to the absorption of individual laser photons. The total probability is obtained from many different photon-number channels, each producing particle pairs with different energies and preferred emission directions.

However, beginning at $\xi \sim 1$, the global behavior changes. Especially for $\xi \gg 1$, the SFBW process resembles the Schwinger effect [Sau31, HE36, Sch51], which describes the creation of electron-positron pairs from the vacuum upon application of a static electric field of strength E_s. When this field is very strong, it can separate virtual electron-positron pairs arising spontaneously from the QED vacuum. The scale is determined by the critical field strength $E_c = m^2/e = 1.3 \times 10^{16}$ V/cm. Acting on a particle of charge e along the distance of one Compton wavelength $\lambda_e = 1/m$, a field of strength E_c expends an electrical work equivalent to one electron rest mass m.

Phenomenologically, the resemblance becomes apparent by comparing the dependence of the total pair-creation rates on the field strength: Regarding the SFBW process, the rate scales for $\xi \gg 1$ as [Rei62, Rit85]

$$\mathcal{R}_{\text{SFBW}} \sim \begin{cases} (E')^{3/2} \exp\left(-\frac{4}{3}\frac{E_c}{E'}\right) & \text{for } E' \ll \frac{1}{2}E_c \,, \\ (E')^{2/3} & \text{for } E' \gg \frac{1}{2}E_c \,, \end{cases} \tag{1.3}$$

where $E' = \frac{\omega_\gamma \omega}{m} A_0$ is an invariant measure of the amplitude $E_0 = \omega A_0$ of the (IPW) laser electric field, which accounts for the frequency of the gamma quantum. For example in the frame of reference where $\omega_\gamma = m$, we simply have $E' = E_0$; however, we note that the gamma quantum is a key ingredient, since a single IPW laser field with uniformly aligned momentum vectors cannot create particle pairs. In comparison, the rate for the Schwinger process scales as [Sch51]

$$\mathcal{R}_{\text{Schwinger}} \sim E_s^2 \sum_{\nu=1}^{\infty} \nu^{-2} \exp\left(-\nu\pi\frac{E_c}{E_s}\right) \sim \begin{cases} E_s^2 \exp\left(-\pi\frac{E_c}{E_s}\right) & \text{for } E_s \ll E_c \,, \\ E_s^2 & \text{for } E_s/E_c \to \infty \,. \end{cases} \tag{1.4}$$

The similarity can be understood intuitively by regarding the regions of highest laser field strength E_0. When ξ is large, the local field strength can be sufficiently strong to produce pairs in a Schwinger-like fashion within a region of extent $\ell = m/(eE_0) = 1/(\omega\xi)$. Since

charge of the positron, respectively. We employ Gaussian units and set $\hbar = c = 1$.

ℓ is much shorter than the laser wavelength $2\pi/\omega$, the field appears as quasi-static. At this point, we see that the characteristic length scale of the SFBW process depends on ξ [Rit85]: While the entire length of the laser field is probed in the *multiphoton regime* where $\xi \lesssim 1$, the process happens predominantly in well-localized regions (of length $\ell \sim 1/\xi$) in the *tunneling regime* where $\xi \gtrsim 1$.
Owing to its truly non-perturbative and intriguing nature, the Schwinger effect attracts significant attention, especially from a theoretical point of view; see [GT16] for a current review. A direct experimental observation is hindered, though, by the enormous value of the critical field strength E_c. Regarding Schwinger-like pair production in the SFBW scheme, the process probability can be enhanced substantially while preserving the characteristic behavior by introducing a secondary laser field of high frequency but small intensity [SGD08]. The absorption of already one of these photons effectively reduces the tunneling distance and can thus amplify the probability tremendously. Following this concept, which is referred to as dynamical assistance, an experimental observation could be facilitated by a suitable combination of presently available radiation sources [JM13].
Further interesting effects occur also at moderate laser intensities with $\xi < 1$. For example, several decades after the first studies, the SFBW process has been investigated theoretically in bichromatic laser fields comprising two laser modes of different frequency and amplitude [NF00, WX14, JM15]. Assuming a stable phase relation between the two modes, particle pairs can be created via absorbing photons in various combinations. When the laser frequencies are chosen in a commensurate ratio, different photon combinations can give rise to kinematically equivalent pairs. These contributions add up coherently and can thus be subject to pronounced interference effects, even with regard to the total number of produced pairs.[2] Similar to multiphoton-interference effects arising in atomic physics, the relative phase between the two laser modes offers a means of coherent phase control on the pair-creation process. Taking advantage of their sensitive and volatile nature, the interference effects could be probed in experimentally demanding measurements providing further verification of strong-field QED.
Other aspects of interest are, for example, spin and polarization effects. The broad diversity of phenomena related to the SFBW process motivates ongoing research, ultimately aiming at an improved understanding of the structure of the QED vacuum.
The current technological development of high-power lasers offers good prospects for corresponding experimental studies. Laser intensities up to the order of 10^{25} W/cm^2 (corresponding to $\xi \sim 1000$) are envisaged in the near future, for example at the Extreme Light Infrastructure (ELI) in Romania [ELI]. With regard to the SFBW process, potential sources of high-energy radiation, besides Compton scattering, are X-ray free-electron lasers (XFELs), or plasma-based high-harmonic generation [Gib96, RadBB$^+$12] requiring powerful optical lasers. The HIBEF project [Hib] at DESY in Hamburg will soon provide a combined setup comprising the European XFEL [DES] and a powerful optical laser, offering possibilities for an experimental investigation of the SFBW process.
The highest laser intensities are achieved by focusing and compressing the laser energy to narrow regions and very short durations. Accordingly, theoretical studies began to account for the actual shape of the laser pulse, see, e.g., [HIM10, TTKH12, KK12a, MHKDP15, DP16] for the SFBW process. The corresponding field configuration is depicted schematically in Fig. 1.1. Regarding the multiphoton regime, the broad frequency spectrum inher-

[2] We note that similar effects occur in related processes, such as the Bethe-Heitler process, where the gamma quantum is replaced by a highly relativistic nucleus. Here, however, we will focus on the Breit-Wheeler process. The references in this introduction comprise only a small selection, which is primarily motivated by conceptual similarities with the present work.

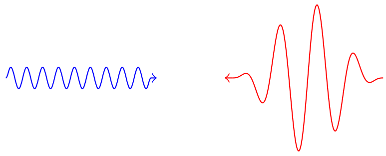

Figure 1.1: Schematic illustration of the field configuration for the SFBW process: The gamma quantum (blue) collides with a short laser pulse (red).

ent to these short pulses facilitates a multitude of production channels, inducing significant differences in the particle spectra in comparison to the case of an IPW laser field. The question arises, how the pulse shape affects the process and in particular how the connection between the pulse spectrum and the energy spectrum of the produced particles is established. Furthermore, given the prominent role of interference effects arising in bichromatic fields, it is not clear if they persist when a short pulse is employed, and how they can be controlled.

The present work provides answers to these questions and investigates various other aspects of the SFBW process in short laser pulses. Our method relies on explicit S-matrix calculations in the framework of laser-dressed QED. The laser pulse is described as a short pulse with a finite duration and a homogeneous structure in the transverse plane, which means that focusing effects are neglected. This approach facilitates the use of Volkov states [Wol35], which describe the quantum dynamics of the charged particles inside the laser field non-perturbatively and allow us to derive analytical expressions for the pair-creation probability.[3]

The influence of the pulse properties on the process is examined in detail. A new model approach for multiphoton processes in short pulses is developed, allowing us to understand the structure of the particle spectra and to detect interference effects. Furthermore, the role of the particle spin in the process is investigated. To this end, we compare predictions from the usual Dirac theory with those obtained from Klein-Gordon theory. In particular, we address the question to which extent the spin sensitivity is affected by the pulse duration.

Finally, we investigate a situation in which the laser field is composed of two individual pulses arriving with a variable time delay. The contributions from both pulses to the pair-production process induce pronounced interference effects, which are intrinsically different to the multiphoton interferences. Inspecting the influence of the delay time, further fundamental properties of the SFBW process can be analyzed and understood from a complementary perspective.

Overall, this work provides a detailed investigation of the SFBW process in short pulses, including intuitive approaches to the underlying physics.

1.2 Structure of this thesis and my contribution

This thesis is structured as follows: In Chap. 2, we present the theoretical description of the SFBW process in a short laser pulse. We will derive analytical expressions for the pair-creation probabilities for scalar and for Dirac particles, respectively. Numerical evaluations of these expressions allow us to explore the properties and the behavior of the

[3] We note that the recent publication [DP16] presents an approximate analytical treatment which accounts for focusing effects.

process in various parameter constellations, where we place our focus on the multiphoton regime of moderate laser intensities. In Chap. 3, we develop a model approach for multiphoton processes originating from the broad frequency spectrum of the pulse. Providing quantitative estimates for the probabilities of different pair-production channels, this approach allows us to understand the energy spectra of the produced particles and serves as a basic tool for our forthcoming analysis. In Chap. 4, we investigate the role of interference effects arising between these production channels. In this context, the influence of the carrier-envelope phase of the laser pulse is analyzed in detail. Furthermore, we address the general question to which extent interference effects, which can induce very pronounced signatures in idealized bichromatic fields, are affected by the spectral broadening inherent to actual radiation sources. In Chap. 5, the role of the particle's spin in the pair-production process is examined. Starting from analytical expressions obtained for IPW laser fields, the impact of the pulse duration on the SFBW process is studied, as well. In Chap. 6, the laser field is generalized to two independent, copropagating pulses with a variable time delay. We extend the S-matrix treatment for scalar particles, and explore the impact of the time delay. This way, the interaction between pair-production processes originating from the individual pulses is analyzed.

All analytical calculations presented in the main part of this thesis have been conducted by myself. Starting from the S-matrix calculation for Dirac particles in [KK12a], I have refined several details of the calculation, e.g. the introduction of a damping in the context of the Boca-Florescu transformation, and applied the trace technique. I have extended the calculation for scalar particles and generalized it for the case of a double pulse with a variable time delay.

In order to compute the pair-production probabilities, I have developed a new C^{++} code and corresponding Matlab scripts for the evaluation. The only external input are the spin-resolved Dirac results in Chap. 5, which were contributed by Dr. Katarzyna Krajewska and Prof. Jerzy Z. Kamiński from the University of Warsaw, Poland.

The model approaches were developed by myself, in particular the P model in Chap. 3, the angular-momentum model in Chap. 5, and the Gaussian model for the delay dependence in Chap. 6. The same holds for the analytical investigation of interference effects in Chap. 4.

1.3 Acknowledgments

I would like to thank Prof. Carsten Müller for his advice and support. Furthermore, I am grateful for discussions with Matthias Dellweg, Prof. Jerzy Z. Kamiński, Dr. Katarzyna Krajewska, Dr. Sebastian Meuren, Dr. Selym Villalba-Chávez, and Dr. Alexander Voitkiv. Finally, I thank Elvira Gröters and Eugen Bleile for their support in the institute.

The two exchange visits to the University of Warsaw in November 2014 and December 2015 were financed by the EU 7th Framework Programme under Grant No. 316244.

1.4 Publications

The results of my work on the SFBW process have led to the following publications:

- M.J.A. Jansen and C. Müller: *Strong-field Breit-Wheeler pair production in short laser pulses: Identifying multiphoton interference and carrier-envelope-phase effects*, Phys. Rev. D. **93**, 053011 (2016), [JM16a].

- M.J.A. Jansen, J.Z. Kamiński, K. Krajewska, and C. Müller: *Strong-field Breit-Wheeler pair production in short laser pulses: Relevance of spin effects*, Phys. Rev. D **94**, 013010 (2016), [JKKM16].
- M.J.A. Jansen and C. Müller: *Strong-field Breit-Wheeler pair production in two consecutive laser pulses with variable time delay*, accepted for publication in Phys. Lett. B (2016), preprint [JM16b].

The results published in the first two articles are presented in Chapters 3,4, and 5 of this thesis. The third article is based on the results presented in Chap. 6.
Besides, during the time of my Ph.D. work, two further articles regarding the SFBW process in two infinitely extended monochromatic fields were published:

- M.J.A. Jansen and C. Müller: *Strongly enhanced pair production in combined high- and low-frequency laser fields*, Phys. Rev. A **88**, 052125 (2013), [JM13].
- M.J.A. Jansen and C. Müller: *Pair Creation of Scalar Particles in Intense Bichromatic Laser Fields*, J. Phys. Conf. Ser. **594**, 012051 (2015), [JM15].

These results were primarily elaborated in the course of my Master's thesis [Jan13].

2 Theoretical Framework

This chapter provides the theoretical framework for a detailed description of the strong-field Breit-Wheeler process induced by a single ultrashort high-intensity pulse. The case of two consecutive pulses will be fully addressed in Chap. 6. After the major constituents of the process are introduced in the first section, we will present the analytical derivation of the pair-production probability for scalar and spinor particles, respectively. Furthermore, general properties, in particular regarding the kinematical situation, are investigated. The latter apply both to the scalar and to the spinor case.

2.1 Preparations

In this section, we introduce and examine the basic constituents of the strong-field Breit-Wheeler scenario. We will characterize the laser field and the high-energy gamma quantum, and revisit the dynamics of charged particles in this environment.

2.1.1 Charged particles in a strong laser field

Beginning with the classical behavior, this section contains a brief review of the dynamics of charged particles being subject to a strong laser field. In comparison, the effect of the gamma quantum can be neglected.
We restrict ourselves to plane-wave fronted laser fields, where all field modes share a common propagation direction, which will be chosen along the z axis. The space-time dependence of the field is entirely determined by the phase variable $\eta = k \cdot x = \omega(t-z)$, where k^μ denotes the wave four-vector for a characteristic mode with frequency ω, and $x^\mu = (t, \mathbf{r})$ denotes the space-time coordinates. Hence, the laser field can be described by a vector potential $\mathcal{A}^\mu(\eta)$, where a gauge is chosen with $\partial \cdot \mathcal{A} = 0$ and $\mathcal{A}^0 = 0$.

2.1.1.1 Classical description

The classical dynamics of a point-like particle with mass m and charge $-e$ in a laser field given by $\mathcal{A}^\mu$ are governed by the equation of motion

$$m\frac{du^\mu}{d\tau} = -e\mathcal{F}^\mu{}_\nu u^\nu \tag{2.1}$$

with the particle's four-velocity $u^\mu = dx^\mu/d\tau$, its proper time τ and the field-strength tensor $\mathcal{F}^{\mu\nu} = \partial^\mu \mathcal{A}^\nu - \partial^\nu \mathcal{A}^\mu$. We employ the metric tensor $g^{\mu\nu} = \mathrm{diag}(+1, -1, -1, -1)$. Due to the restriction to a common propagation direction for all field modes, the equation of motion can readily be integrated, see App. A.1.
Assuming a laser pulse of finite duration, with $\mathcal{A}^\mu(0) = 0$, the kinetical momentum $p^\mu(\eta) = mu^\mu(\eta)$ of the particle in the laser field follows as

$$p^\mu(\eta) = p_0^\mu + e\mathcal{A}^\mu(\eta) - \left(ep_0 \cdot \mathcal{A}(\eta) + \frac{e^2}{2}\mathcal{A}^2(\eta)\right)\frac{k^\mu}{k \cdot p_0} \tag{2.2}$$

where $p_0^\mu = p^\mu(0)$ denotes the particle's initial four-momentum.

The form of Eq. (2.2) allows a direct conclusion: When the laser pulse has passed the particle, i.e. when $\mathcal{A}^\mu(\eta) = 0$ again, the particle has its initial momentum p_0^μ again. There is no net effect of the laser field on the particle momentum.
Hence, with regard to the pair-creation process, p_0^μ can equally be understood as the final momentum of a particle. In a purely classical consideration, the particle may be thought of to be created at a certain point η_b with a momentum in agreement with $p^\mu(\eta_b)$ as given by Eq. (2.2). However, due to the quantum nature of the pair-creation process, the point η_b cannot be specified. Instead, in order to formulate conservation laws, it is helpful to employ the average momentum

$$q^\mu = p_0^\mu + \langle e\mathcal{A}^\mu \rangle - \left\langle ep_0 \cdot \mathcal{A} + \frac{e^2}{2}\mathcal{A}^2 \right\rangle \frac{k^\mu}{k \cdot p_0}\,, \tag{2.3}$$

where $\langle \dots \rangle$ denotes a phase average. A particle being detected outside the laser field with momentum p_0^μ possesses an average momentum q^μ inside the field. These momenta q^μ are referred to as laser-dressed momenta, and they are employed in the theoretical treatments of various strong-field QED processes.[1] They can be ascribed an effective, laser-dressed mass

$$m_* = \sqrt{q^2} = \sqrt{m^2 + e^2\langle \mathcal{A} \rangle^2 - e^2 \langle \mathcal{A}^2 \rangle}. \tag{2.4}$$

2.1.1.2 Quantum description

In the framework of relativistic quantum mechanics, the dynamics of a scalar particle in the laser field can be described by the Klein-Gordon equation

$$\left[\frac{\partial^2}{\partial t^2} + (-i\boldsymbol{\nabla} + e\boldsymbol{\mathcal{A}})^2 + m^2\right]\Psi = 0\,. \tag{2.5}$$

For a particle (anti-particle) with free four-momentum p_-^μ (p_+^μ), it is solved by the Gordon-Volkov states[2]

$$\Psi_{p_\pm} = \sqrt{\frac{m}{VE_{p_\pm}}} e^{i[\pm p_\pm \cdot x + \Lambda_\pm]} \tag{2.6}$$

with

$$\Lambda_\pm = \frac{1}{k \cdot p_\pm} \int_0^{k\cdot x} \left[ep_\pm \cdot \mathcal{A}(\eta) \mp \frac{e^2}{2}\mathcal{A}^2(\eta)\right] d\eta \tag{2.7}$$

and with $p_\pm^\mu = (E_{p_\pm}, \mathbf{p}_\pm)$, $E_{p_\pm} = \sqrt{m^2 + \mathbf{p}_\pm^2}$ and a normalizing volume V. As we will see in the course of this work, the phase factor $\Lambda_\pm$ is closely related to the classical dynamics of the particle in the laser field. In fact, the entire phase of the Gordon-Volkov states can be associated with the classical action of the particle in the laser field. Conversely, outside the pulse, $\Lambda_\pm$ is constant. Consequently, far away from the pulse, the Gordon-Volkov state $\Psi_{p_\pm}$ behaves asymptotically like a usual plane-wave momentum Eigenstate

[1] Despite the dressed momenta being expressed in terms of the vector potential, they are derived from the classical dynamics, which solely depend on the electric and magnetic fields. Hence, when another gauge is chosen, the expression for the dressed momenta may look different, but the dressed momenta themselves should eventually be the same.

[2] The Gordon-Volkov states can for example be found in [EKK09]. In comparison, we have included an additional factor of $\sqrt{2m}$ in the prefactor. Our choice is motivated by a normalization constraint based on the charge density. Accordingly, we account for the different prefactor by reducing the interaction Hamiltonian (see Eq. (2.15) below) by the factor $2m$. One may argue that this is a more natural choice, since, this way, the interaction Hamiltonian has consistent dimensionality, and resembles the non-relativistic expression, c.p. [Gre00], p. 14.

with Eigenvalue $\mp p_\pm$. In the following, we will formally describe the pair-production process as the transition of an electron from the negative-energy initial state Ψ_{p_+} to the positive-energy final state Ψ_{p_-}. The unoccupied initial state then describes a positron with asymptotic momentum $+p_+$.
The spin of the particles can be accounted for by employing the full Dirac equation

$$\left[i\partial\!\!\!/ + e\mathcal{A}\!\!\!/ - m\right]\Psi = 0\,, \tag{2.8}$$

where Feynman slash notation indicates four-products with Dirac gamma matrices, see App. A.2 for further details on the conventions. It is solved by the Dirac-Volkov states (see, e.g., [BLP80])

$$\Psi^{(1/2)}_{p_\pm s_\pm} = \sqrt{\frac{m}{VE_{p_\pm}}}\left[1 \pm \frac{e k\!\!\!/ \mathcal{A}\!\!\!/}{2k\cdot p_\pm}\right] w_{p_\pm s_\pm} e^{i[\pm p_\pm\cdot x + \Lambda_\pm]}\,. \tag{2.9}$$

The free spinors $w_{p_\pm s_\pm}$ are presented in App. A.3. The symbols $s_\pm$ denote the particles' spin state. The form of the Volkov states reveals that the spin returns to its initial orientation after the particle has left the laser pulse.
With regard to our following calculation, we note that the Dirac-Volkov states can be shown (see, e.g., [Zak05] and [BF10]) to form an orthogonal basis of the solutions to the Dirac equation (2.8). The analogue holds in the scalar case [Boc11].

2.1.2 Plane-wave laser fields of finite extent

In order to model a laser pulse of finite extent, we introduce a vector potential of the form

$$\mathcal{A}^\mu = A_0 f(\eta)\mathcal{X}_{[0,2\pi]}(\eta)\epsilon^\mu \tag{2.10}$$

where the characteristic function $\mathcal{X}_{[0,2\pi]}(\eta)$ restricts the phase $\eta = k\cdot x$ to the interval $[0, 2\pi]$. Here, the fundamental wave four-vector $k^\mu = \omega_b(1, 0, 0, 1)$ is defined for the basic frequency ω_b. The space-time dependence of the field, as well as its spectral composition, is determined by the function $f(\eta)$, which will remain unspecified for the following derivation. Employing a real polarization vector ϵ^μ with $\epsilon\cdot k = 0$, the field is linearly polarized. Having plane wave fronts, this field is homogeneous in the transverse plane, yet finite along the longitudinal direction. Neglecting focusing effects, this approach allows us to model a finite laser pulse.
Our numerical examples in chapters 3 – 6 will be presented for a specific choice of the shape function, which is defined by means of its derivative

$$f'(\eta) = \sin^2(\eta/2)\sin(N_{\text{osc}}\eta + \chi)\,. \tag{2.11}$$

The shape is determined by the $\sin^2$-envelope which comprises a number N_{osc} of harmonic oscillations. In order to fulfill Maxwell's equations, the number of cycles has to be restricted to $N_{\text{osc}} \geq 2$. Otherwise, the vector potential in Eq. (2.10) would not be continuous. The relative phase between the oscillations and the envelope is controlled by the carrier-envelope phase χ. The spectrum of this pulse obtains its dominant contribution from the central frequency $\omega_c = N_{\text{osc}}\omega_b$. Further details will be addressed below, in particular in Chap. 4 and additionally in App. A.6.

With the laser field assumed to be rather strong, depleting effects due to the absorption of individual photons can be neglected[3], which allows us to treat the laser field classically in the following discussion. The field strength will be determined by means of the Lorentz-invariant parameter

$$\xi_{\max} = \frac{eA_0}{m} \max_\eta |f(\eta)| \,. \tag{2.12}$$

This definition can also be applied to infinitely extended, monochromatic fields with $\mathcal{A}^\mu = A_0 \cos(\eta)\epsilon^\mu$, yielding the usual field-strength parameter $\xi = eA_0/m$.[4] As can be seen from Eq. (2.2), a strong laser field with $\xi \sim 1$ accelerates particles, which were initially at rest, to relativistic velocities within a single field cycle. For a monochromatic field of frequency ω, the peak intensity is $I[10^{20}\mathrm{W/cm}^2] = (\xi\omega[\mathrm{eV}]/7.5)^2$ [DPMHK12].

2.1.3 Gamma quantum

The gamma quantum is described as one single mode $\{\mathbf{k}_\gamma, \lambda_\gamma\}$ of a quantized radiation field $\hat{\mathcal{A}}^\mu$. Its absorption during the pair-production process can be expressed as an effective scattering potential

$$\mathcal{A}^\mu_\gamma = \langle 0|\hat{\mathcal{A}}^\mu|\mathbf{k}_\gamma\lambda_\gamma\rangle = \sqrt{\frac{2\pi}{V\omega_\gamma}} e^{-ik_\gamma\cdot x}\epsilon^\mu_\gamma \,. \tag{2.13}$$

Here, $k^\mu_\gamma = (\omega_\gamma, \mathbf{k}_\gamma)$ is the corresponding wave four-vector, and ϵ^μ_γ is a real polarization vector with mode index λ_γ, with $k_\gamma \cdot \epsilon_\gamma = 0$. The gamma quantum is assumed to be colliding head-on with the laser pulse.

2.2 Strong-Field Breit-Wheeler pair production of scalar particles

In this section, we present a detailed derivation of an analytical expression for the pair-creation probability of spinless particles. Additional properties, in particular the energy-momentum balance, will be addressed as well. The latter plays a crucial role for the understanding of the resulting energy spectra of the produced particles.

2.2.1 The pair-creation probability

In the framework of relativistic quantum mechanics, the creation of an electron-positron pair can formally be described as the transition of one laser-dressed electron from the negative- to the positive-energy continuum. The resulting unoccupied state then corresponds to the positron.

[3] In [SHMB16], depletion effects due to nonlinear Compton scattering and successive Breit-Wheeler pair production are estimated to become relevant when a strong laser with $eA_0/m \sim 10^3$ interacts with an electron beam with a charge of nC. There, a substantial fraction of the laser energy is transferred to the produced particles. However, in our work, we employ $eA_0/m \sim 1$.

[4] We introduce $\xi_{\max}$ at the level of the vector potential. Regarding effects which are rather caused by the laser electric field, the correspondence with the ξ parameter introduced for monochromatic fields has to be treated with care, since the pulse shape affects the derivative which connects the electric field and the vector potential: For a monochromatic field with frequency ω, the amplitudes of the electric field and of the vector potential differ by a factor ω. Conversely, the pulse envelope induces deviations from this factor, in particular for short pulses.

The probability of the process can be obtained from the S-matrix amplitude [EKK09]

$$\mathcal{S}_{p_+p_-} = -i \int d^4x \, \Psi^*_{p_-} \mathcal{H}_{\rm int} \Psi_{p_+} \tag{2.14}$$

which describes the creation of an electron with momentum p_-^μ and of a positron with momentum p_+^μ. The process is formally induced by the interaction Hamiltonian[5]

$$\mathcal{H}_{\rm int} = \frac{-ie}{2m} \left(\mathcal{A}_\gamma \cdot \overrightarrow{\partial} - \overleftarrow{\partial} \cdot \mathcal{A}_\gamma \right) - \frac{e^2}{m} \mathcal{A}_\gamma \cdot \mathcal{A} \tag{2.15}$$

which accounts for the absorption of the gamma quantum.
Inserting the Gordon-Volkov states $\Psi_{p_\pm}$ and sorting the constituents with respect to their space-time dependence, the S matrix can be brought into the form

$$\mathcal{S}_{p_+p_-} = S_0 \int d^4x \, C(\eta) e^{-iQ\cdot x - iH(\eta)} \tag{2.16}$$

with a prefactor $S_0 = iem\sqrt{\frac{2\pi}{V^3 E_{p_+} E_{p_-} \omega_\gamma}}$, a combined momentum vector

$$Q^\mu = k_\gamma^\mu - \left(p_+^\mu + p_-^\mu\right) \,, \tag{2.17}$$

and auxiliary functions

$$\begin{aligned} C(\eta) &= a + bf(\eta)\mathcal{X}_{[0,2\pi]}(\eta) \,, \\ H(\eta) &= \int_0^\eta h(\tilde{\eta}) d\tilde{\eta} \,, \\ h(\eta) &= \left[h_1 f(\eta) + h_2 f^2(\eta)\right] \mathcal{X}_{[0,2\pi]}(\eta) \,, \end{aligned} \tag{2.18}$$

which include the abbreviations[6]

$$\begin{aligned} a &= \frac{p_- - p_+}{2m} \cdot \epsilon_\gamma \,, \\ b &= \frac{eA_0}{m} \epsilon \cdot \epsilon_\gamma \,, \\ h_1 &= -eA_0 \left[\frac{\epsilon \cdot p_+}{k \cdot p_+} - \frac{\epsilon \cdot p_-}{k \cdot p_-} \right] \,, \\ h_2 &= -\frac{e^2 A_0^2}{2} \left[\frac{1}{k \cdot p_+} + \frac{1}{k \cdot p_-} \right] \,. \end{aligned} \tag{2.19}$$

As a next step, the space-time integration in Eq. (2.16) has to be carried out. To this end, we employ light-cone coordinates, which account for the space-time dependence of the laser pulse. For a given four vector x^μ, we first introduce the parallel component $x^\parallel = \mathbf{x} \cdot \mathbf{n} = z$, where the unit vector $\mathbf{n}$ denotes the laser propagation direction. The corresponding light-cone coordinates are

$$\begin{aligned} x^- &= x^0 - x^\parallel \,, \\ x^+ &= \frac{1}{2}(x^0 + x^\parallel) \,, \\ \mathbf{x}^\perp &= \mathbf{x} - x^\parallel \mathbf{n} \,. \end{aligned} \tag{2.20}$$

[5]The prefactor $(2m)^{-1}$ is chosen in accordance with the normalization of the Gordon-Volkov states in Eq. (2.6).

[6]Note that we have slightly changed the definition of S_0, $a \sim g_0$ and $b \sim g_1$ in comparison with [JKKM16].

Products between four vectors x^μ and y^μ are of the form $x \cdot y = x^- y^+ + x^+ y^- - \mathbf{x}^\perp \cdot \mathbf{y}^\perp$. Concerning the phase variable η, this means $\eta = k \cdot x = k^+ x^- = k^0 x^-$. The integration measure transforms as $d^4x = dx^- dx^+ d^2x^\perp$.
This way, the three integrations along x^+ and $\mathbf{x}^\perp$ can readily be evaluated and yield

$$\mathcal{S}_{p_+p_-} = (2\pi)^3 S_0 \delta(Q^-) \delta^{(2)}(\mathbf{Q}^\perp) \int dx^- C(k^0x^-) e^{-iQ^0x^- - iH(k^0x^-)} \,, \tag{2.21}$$

where the constraint $Q^- = 0 = Q^0 - Q^\parallel$ has been used to rewrite $Q^+ = Q^0$.
Next, we have to investigate the remaining integral

$$I = \int dx^- C(k^0x^-) e^{-iQ^0x^- - iH(k^0x^-)} \tag{2.22}$$

which we decompose according to the definition of $C(k^0x^-)$ from Eq. (2.18) into the form $I = aI_0 + bI_1$ with the integrals

$$\begin{aligned} I_0 &= \int dx^- e^{-iQ^0x^- - iH(k^0x^-)} \,, \\ I_1 &= \int dx^- f(k^0x^-) \mathcal{X}_{[0,2\pi]}(k^0x^-) e^{-iQ^0x^- - iH(k^0x^-)} \,. \end{aligned} \tag{2.23}$$

While the characteristic function restricts the integrand of I_1 to a finite phase interval, I_0 is formally unlimited. We recall that $H(k^0x^-)$ is constant outside the pulse interval $x^- \in [0, 2\pi/k^0]$. In order to regularize the integral I_0, we regard it as the limit of a series of convergent integrals, which, in this context, is referred to as the Boca-Florescu transformation [BF09]. The latter was also revisited in App. B of [KK12b]. We present a slightly modified treatment, offering a transparent way to deal with the limit process. For $\varepsilon > 0$, we introduce a damping factor $e^{-\varepsilon|x^-|}$ in order to control the asymptotic behavior of the integrand. An integration by parts yields

$$\begin{aligned} I_0(\varepsilon) &= \int dx^- e^{-iQ^0x^- - iH(k^0x^-) - \varepsilon|x^-|} \\ &= \left[\frac{e^{-iQ^0x^- - iH(k^0x^-) - \varepsilon|x^-|}}{-iQ^0 - \varepsilon \,\mathrm{sign}(x^-)} \right]_{-\infty}^{\infty} - \int dx^- \frac{-ik^0 h(k^0x^-)}{-iQ^0 - \varepsilon \,\mathrm{sign}(x^-)} e^{-iQ^0x^- - iH(k^0x^-) - \varepsilon|x^-|} \end{aligned} \tag{2.24}$$

where the surface terms vanish due to the damping. The remaining integral is restricted to a finite interval since $h(k^0x^-)$ includes the characteristic function. Accordingly, assuming weak damping $\varepsilon \ll |Q^0|$, the integral can be approximated by

$$I_0(\varepsilon) = -\frac{k^0}{Q^0} \int h(k^0x^-) e^{-iQ^0x^- - iH(k^0x^-)} dx^- + \mathcal{O}(\varepsilon/|Q^0|) \,. \tag{2.25}$$

The condition $Q^0 \neq 0$ can be verified by regarding the kinematical situation [KK12a] and will be discussed in Sec. 2.2.3. Furthermore, we will deduce a global lower bound for $|Q^0|$ for a given gamma-quantum momentum k_γ^μ. Hence, ε can be chosen sufficiently small in order to safely neglect the higher-order terms. The original integral I_0 can now be identified as

$$I_0 \equiv -\frac{k^0}{Q^0} \int h(k^0x^-) e^{-iQ^0x^- - iH(k^0x^-)} dx^- \,. \tag{2.26}$$

This way, the problematic limit $\varepsilon \to 0$ is avoided at the price of an arbitrarily small damping. This damping affects the phase coordinate $x^- = t - z$, which is naturally limited by the longitudinal extent of the interaction chamber and by the duration of the experiment.
As a result, the integral I from Eq. (2.22) can be expressed as

$$I = \int dx^- \tilde{C}(k^0 x^-) e^{-iQ^0 x^- - iH(k^0 x^-)} \tag{2.27}$$

with the new definition

$$\tilde{C}(\eta) = \left[\tilde{b} f(\eta) + \tilde{c} f^2(\eta)\right] \mathcal{X}_{[0,2\pi]}(\eta) \tag{2.28}$$

and the corresponding abbreviations

$$\begin{aligned} \tilde{b} &= b - \frac{k^0}{Q^0} h_1\, a\,, \\ \tilde{c} &= -\frac{k^0}{Q^0} h_2\, a\,. \end{aligned} \tag{2.29}$$

With both terms in $\tilde{C}(\eta)$ being affected by the characteristic function $\mathcal{X}_{[0,2\pi]}(\eta)$, the entire integration is now limited to a finite domain and can be evaluated numerically. When the laser field is infinitely extended, the integrand is usually Fourier decomposed by means of Bessel functions. This is in principle also possible for our particular shape function as defined in Eq. (2.11), but each term contains a product of about ten ordinary Bessel functions, which is barely suitable for computational purposes (see also App. A.6 and A.7).
The total pair-creation probability for Klein-Gordon particles is obtained by integrating the absolute square of the S-matrix element over all possible particle states. Additionally, assuming an unpolarized beam of gamma quanta, the average over the corresponding polarization directions is taken. Accordingly, the total pair-creation probability reads

$$\mathscr{P}^{\mathrm{KG}} = \frac{1}{2} \sum_{\lambda_\gamma} \int \frac{V d^3 p_+}{(2\pi)^3} \int \frac{V d^3 p_-}{(2\pi)^3} |\mathcal{S}_{p_+ p_-}|^2\,, \tag{2.30}$$

where $V/(2\pi)^3$ can be seen as the number of states per unit volume in the momentum space.
This expression contains the absolute square of the δ functions, which has to be treated with care. They result from the integration in light-cone coordinates, such that the associated volume is not just the normalizing volume V. Instead, it is helpful to regard the gamma quantum as a wavepacket, see for example [MHKDP15]. As presented in App. A.5, one finds that the square of $2\pi\delta(Q^-)$ yields $(k^0_\gamma/k^-_\gamma)L$, where L denotes the extent of the normalizing volume along the propagation direction of the gamma quantum. In our case of a head-on collision, the scaling factor k^0_γ/k^-_γ reduces to $\frac{1}{2}$. It can be seen as the ratio between the interaction time and the temporal extent of the gamma quantum. This way, the square of the δ functions occurring in Eq. (2.30) effectively leads to

$$\left|(2\pi)^3 \delta(Q^-) \delta^{(2)}(\mathbf{Q}^\perp)\right|^2 = \frac{1}{2} V\, (2\pi)^3 \delta(Q^-) \delta^{(2)}(\mathbf{Q}^\perp)\,. \tag{2.31}$$

As a next step, we will integrate over the electron momenta, since we are rather interested in the positron. The three conditions $Q^- = 0$ and $\mathbf{Q}^\perp = 0$ are sufficient to uniquely determine the electron momentum as a function of the gamma-quantum energy and of the positron momentum: Owing to $\mathbf{Q}^\perp = 0$, the transverse components of the electron momentum fulfill $\mathbf{p}_-^\perp = -\mathbf{p}_+^\perp$. The remaining condition $Q^- = 0$ can be rewritten in the form

$$p_-^0 = k_\gamma^- - p_+^- + p_-^\parallel \,. \tag{2.32}$$

Requiring the free particle states to be on the mass shell with $p_\pm^0 = \sqrt{m^2 + \mathbf{p}_\pm^2}$, we take the square of Eq. (2.32) and obtain a preliminary solution for the parallel component of the electron momentum

$$p_-^\parallel = \frac{m^2 + \mathbf{p}_+^\perp \cdot \mathbf{p}_+^\perp - (k_\gamma^- - p_+^-)^2}{2(k_\gamma^- - p_+^-)} \tag{2.33}$$

assuming $k_\gamma^- - p_+^- \neq 0$. Furthermore, having taken the square of Eq. (2.32), we have to make sure that the electron energy p_-^0 has the correct sign. To this end, we revisit Eq. (2.32) and insert our preliminary solution for $p_-^\parallel$, which yields

$$p_-^0 = \frac{m^2 + \mathbf{p}_+^\perp \cdot \mathbf{p}_+^\perp + (k_\gamma^- - p_+^-)^2}{2(k_\gamma^- - p_+^-)} \,. \tag{2.34}$$

Accordingly, we see that $p_-^0 > 0$ if

$$k_\gamma^- - p_+^- > 0 \,, \tag{2.35}$$

where $k_\gamma^- = 2\omega_\gamma$. This condition restricts the possible positron momenta for a given gamma-quantum energy and will be investigated in the following section. When this condition is fulfilled, Eq. (2.33) is a valid solution for $p_-^\parallel$.
Finally, in order to carry out the integration, the δ functions are expressed as a function of $\mathbf{p}_-$, which induces an additional factor $p_-^0/p_-^- > 0$ stemming from $\delta(Q^-)$, with $p_-^- = k_\gamma^- - p_+^-$. After these steps, the pair-production probability reads

$$\mathscr{P}^{\mathrm{KG}} = \frac{\alpha m^2}{16\pi^2 \omega_\gamma} \sum_{\lambda_\gamma} \int d^3p_+ \frac{1}{p_+^0 (k_\gamma^- - p_+^-)} \left| \int_0^{2\pi/k^0} dx^- \tilde{C}(k^0 x^-) e^{-iQ^0 x^- - iH(k^0 x^-)} \right|^2 \tag{2.36}$$

where $\alpha = e^2$ denotes the Feinstructure constant. The integration is understood to be restricted to those positron momenta for which the condition given by Eq.(2.35) is fulfilled. In principle, this expression can be used to compute the total pair-creation probability for any set of parameters describing the laser pulse and the gamma quantum.

2.2.2 Kinematical constraints

In the following, we will discuss the kinematical constraints which arise when the light-cone δ functions are evaluated in order to settle the electron momentum for a given combination of the gamma-quantum energy and the positron momentum.
Introducing the polar angle ϑ via $p_+^\parallel = |\mathbf{p}_+| \cos(\vartheta)$, Eq. (2.35) can be written in the form

$$\cos(\vartheta) > \frac{\sqrt{m^2 + \mathbf{p}_+^2} - k_\gamma^-}{|\mathbf{p}_+|} \tag{2.37}$$

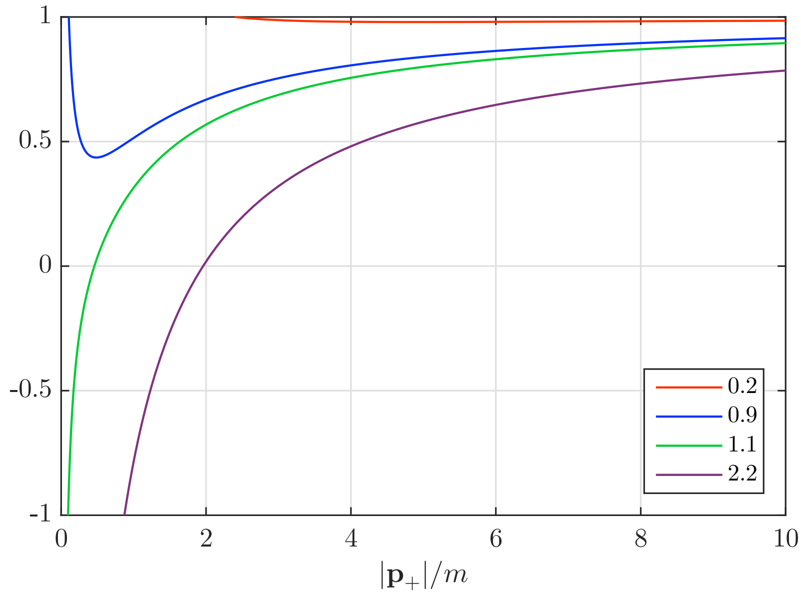

Figure 2.1: Right-hand side of Eq. (2.37) as a function of $|\mathbf{p}_+|/m$ for various values of k_γ^-/m as indicated in the legend. Pairs can only be created for values of $\cos(\vartheta)$ which are above the curves.

assuming $|\mathbf{p}_+| > 0$. Accordingly, the kinematical situation is crucially determined by the right-hand side of Eq. (2.37), which is plotted in Fig. 2.1 as a function of $|\mathbf{p}_+|$ for various values of the gamma-quantum energy. If the gamma-quantum energy is small with $k_\gamma^- = 2\omega_\gamma < m$ (see red and blue curves in Fig. 2.1), pair creation is limited to positrons with a minimum momentum $|\mathbf{p}_+| > \frac{m^2-(k_\gamma^-)^2}{2k_\gamma^-}$ which will be emitted into a narrow angular cone around the laser forward direction.
Conversely, if $k_\gamma^- > m$ (see green and purple curves), positrons with relatively small momenta $|\mathbf{p}_+| < \frac{(k_\gamma^-)^2-m^2}{2k_\gamma^-}$ can be emitted into all angular directions. Positrons with higher energies are again emitted into an increasingly narrow cone around the forward direction.
For symmetry reasons, the same consideration applies if the electron momentum was to be determined for a given combination of the gamma-quantum energy and the positron momentum. As we will see in the following, the conclusions drawn in this section still hold when the effect of the laser field on the charged particles is taken into account.

2.2.3 Energy-momentum balance

In this section, we formulate the energy-momentum balance of the process, which will eventually give access to the actually absorbed energy from the laser pulse. Additionally, the corresponding derivation gives further insight into the kinematical situation and in particular allows us to state a lower limit for $|Q^0|$.
As a first step, we notice that the requirements $\mathbf{Q}^\perp = 0$ and $Q^- = 0$ imposed by the δ functions coincide with the properties of the laser wave vector k^μ, which fulfills $\mathbf{k}^\perp = 0$ and $k^- = 0$ as well. Accordingly, Q^μ can be expressed as a multiple of k^μ, allowing us to state the requirements $\mathbf{Q}^\perp = 0$ and $Q^- = 0$ in the form

$$k_\gamma^\mu + rk^\mu = p_+^\mu + p_-^\mu \,, \tag{2.38}$$

with an unrestricted real number r. A restriction can be obtained from the square of Eq. (2.38), where the on-shell condition $p_\pm^2 = m^2$ can be used explicitly. This way, one finds $r \geq m^2/(\omega_\gamma \omega_b)$, where ω_b denotes the laser (basis) frequency associated with k^μ.
Since $Q^\mu = -rk^\mu$, we can deduce $-Q^0 \geq m^2/\omega_\gamma$, which sets the scale for the damping factor applied in our version of the Boca-Florescu transformation. Furthermore, the criterion $Q^0 \neq 0$ follows as well.
Equation (2.38) can be understood as a preliminary energy-momentum balance of the pair-creation process in the limit of small laser intensities. The δ functions restrict the momenta of the particles such that the energy-momentum balance can be fulfilled by absorbing a certain four vector rk^μ. With the spectral composition of the laser pulse being undetermined yet, this process is allowed since rk^μ could in principle be provided by one laser photon, or by a combination of several laser photons.
In the previous section, we have seen that in particular high-energy particles are emitted into the laser forward direction, which can now be understood: These processes require a large photon energy to be absorbed from the laser pulse, which is necessarily accompanied by an equally large momentum in the laser forward direction, which needs to be compensated.
With the laser field being treated classically, the actually absorbed photon energy cannot be accessed directly. Instead, we have to rely on the appropriate energy-momentum balance. For higher laser intensities, we have to take into account that the momenta of the charged particles are strongly affected by the laser field. To this end, we recall the classical dynamics of the particles and regard their dressed momenta $q_\pm^\mu$.[7] The sum of the dressed momenta is of the form

$$q_+^\mu + q_-^\mu = p_+^\mu + p_-^\mu + wk^\mu \,, \tag{2.39}$$

with

$$w = \left\langle \frac{ep_+ \cdot \mathcal{A}}{k \cdot p_+} - \frac{e^2 \mathcal{A}^2}{2k \cdot p_+} \right\rangle - \left\langle \frac{ep_- \cdot \mathcal{A}}{k \cdot p_-} + \frac{e^2 \mathcal{A}^2}{2k \cdot p_-} \right\rangle . \tag{2.40}$$

The effect of the laser field on the particles induces an additional term in the sum of the momenta which is proportional to the laser wave vector k^μ.[8] The corresponding energy (and momentum) is provided by the laser field. Accordingly, we formulate the full energy-momentum balance in the form

$$k_\gamma^\mu + r_* k^\mu = q_+^\mu + q_-^\mu \tag{2.41}$$

where $r_* = r + w$. In particular, we note that the relation imposed by $\mathbf{Q}^\perp = 0$ and $Q^- = 0$ between the free momenta $p_\pm^\mu$ and the gamma quantum k_γ^μ has remained unaffected by these steps. The new parameter r_* has to fulfill the threshold condition $r_* \geq m_*^2/(\omega_\gamma \omega_b)$ which is formulated with the laser-dressed mass of the particles. Finally, the absorbed laser photon energy follows as

$$E_L = q_+^0 + q_-^0 - k_\gamma^0 \,. \tag{2.42}$$

[7]The positron dressed momentum q_+^μ can be obtained from Eq. (2.3) by employing the free positron momentum p_+^μ and by replacing $-e \to e$. Our treatment aims at medium intensities $\xi_{\max} \leq 1$. Accordingly, the formation length of the pair-creation process (see [Rit85]) covers a substantial fraction of the pulse, which justifies to average over the full pulse length.

[8]We note that the product wk^μ is independent of the choice of the laser wave vector k^μ, since the frequency cancels in expressions $k^\mu/(k \cdot p_\pm)$.

As we shall see in the following chapters, this energy is a crucial key to the understanding of the energy spectra of the produced particles. We close this section with two additional remarks:
Equation (2.41) closely resembles the energy-momentum balance which is obtained when an infinitely extended, monochromatic laser field is employed. There, four instead of three δ functions arise. As a consequence, the parameter r_* is restricted to integer values, which further supports the picture of the particles being created via absorbing distinct laser photons, despite the classical treatment of the laser field. Furthermore, the dressed momenta arise naturally when the exponents of the Volkov states (which contain the classical action) are decomposed into purely oscillatory and linearly growing phase dependencies.
In principle, a similar decomposition can also be carried out in our case of a finite pulse, which is demonstrated in App. A.7 using the notation of the double-pulse scenario. But with the combined dressing effect being proportional to k^μ with $k^- = 0 = \mathbf{k}^\perp$, this effect is not visible for the three δ functions. Still, this detour shows why the effect of the dressing can be written as

$$w = -\left(h_1\langle f\rangle + h_2\langle f^2\rangle\right) \tag{2.43}$$

with h_1 and h_2 being introduced in Eq. (2.19) as the constituents of the combined exponent $H(\eta)$.[9] With our shape function $f(\eta)$ being restricted to the phase interval $[0, 2\pi]$, we employ the phase average in the form $\langle f\rangle = \frac{1}{2\pi}\int_0^{2\pi} f(\eta)d\eta$.

2.2.4 Differential probabilities

Starting from the expression for the total pair-production probability in Eq. (2.36), the fully differential probability

$$\frac{d^3\mathscr{P}^{\mathrm{KG}}}{dE_{p_+}d^2\Omega_{p_+}} = \frac{\alpha m^2}{16\pi^2\omega_\gamma}\sum_{\lambda_\gamma}\frac{|\mathbf{p}_+|}{k_\gamma^- - p_+^-}\left|\int_0^{2\pi/k^0} dx^-\tilde{C}(k^0x^-)e^{-iQ^0x^- - iH(k^0x^-)}\right|^2 \tag{2.44}$$

can be defined, since $d^3p_+ = E_{p_+}|\mathbf{p}_+|d^2\Omega_{p_+}dE_{p_+}$ with $d^2\Omega_{p_+} = \sin(\vartheta)d\vartheta d\varphi$, where φ denotes the azimuthal angle describing the positron emission direction with respect to ϵ^μ. The quantity $d^3\mathscr{P}^{\mathrm{KG}}/(dE_{p_+}d^2\Omega_{p_+})$ describes to which extent the creation of positrons with energy E_{p_+} and emission direction as given by ϑ and φ contribute to the total pair-creation probability. One should keep in mind that this contribution is not only determined by the probability density $\sim|\mathcal{S}_{p_+p_-}|^2$, but also by the infinitesimal volume of the surrounding phase space. The latter is sensitive to the choice of the coordinates.
As enforced by the three δ functions, the original six-dimensional integration space available in Eq. (2.30) is reduced to a three-dimensional sub-space which is now parametrized by the positron momentum. Evaluating $\delta(Q^-)$ has led to the factor p_-^0/p_-^-, which can be regarded as the Jacobian of the transform between the electron momentum and the subvolume which is defined via $Q^- = 0 = \mathbf{Q}^\perp$. This factor induces an asymmetry between the laser forward and backward direction (see, for example, Fig. 5.3 in Chap. 5), which reflects the geometry of the coordinates, rather than the properties of the process.[10]

[9] As it turns out, with regard to the dressing effect, H was defined with a counter-intuitive sign.

[10] Let us regard the following instructive example: When the positron energy is chosen with $E_{p_+} = \omega_\gamma$ in a setup with vanishingly small field strength $\xi_{\max} \ll 1$, the required laser photon energy is $E_L \approx \omega_\gamma$, such that the process closely resembles the original Breit-Wheeler process in the center-of-mass system, provided that the pulse spectrum contains a photon of frequency ω_γ. Accordingly, each particle can be expected to be produced with equal probabilities in the forward and backward direction. However, due

2.3 Production of Dirac particles

Having completed the analytical derivation of the pair-production probability in the scalar case, we will now proceed to the full calculation including the spin of the particles. Evaluating the products of the spinors and the gamma matrices requires additional steps, which can, however, be postponed by rearranging the expression. At this point, many important steps can be applied in close analogy to the scalar case.

2.3.1 The pair-production probability

Employing the Dirac-Volkov states as introduced in Eq.(2.9), the S-matrix element for the production of Dirac particles reads

$$\mathcal{S}^{(1/2)}_{p_+s_+,p_-s_-} = ie\int d^4x\,\overline{\Psi}^{(1/2)}_{p_-s_-}\not{\mathcal{A}}_\gamma\Psi^{(1/2)}_{p_+s_+}\,. \tag{2.45}$$

Similarly to the scalar case, the expression can be brought into the form

$$\mathcal{S}^{(1/2)}_{p_+s_+,p_-s_-} = S_0\int d^4x\,\mathfrak{C}(\eta)\,e^{-iQ\cdot x-iH(\eta)} \tag{2.46}$$

with S_0, Q^μ and $H(\eta)$ as given in Sec. 2.2.1. The spinors are included in the reduced matrix element

$$\mathfrak{C}(\eta) = \mathfrak{a} + \mathfrak{b}f(\eta)\mathcal{X}_{[0,2\pi]}(\eta) \tag{2.47}$$

with the new abbreviations

$$\begin{aligned}\mathfrak{a} &= \overline{w}_{p_-s_-}\not{\epsilon}_\gamma w_{p_+s_+}\,,\\ \mathfrak{b} &= \frac{eA_0}{2}\,\overline{w}_{p_-s_-}\left[\frac{\not{\epsilon}_\gamma\not{k}\not{\epsilon}}{k\cdot p_+} - \frac{\not{\epsilon}\not{k}\not{\epsilon}_\gamma}{k\cdot p_-}\right]w_{p_+s_+}\,.\end{aligned} \tag{2.48}$$

Initially, $\mathfrak{C}$ contains a further term of the form $\overline{\frac{e\not{k}\not{\mathcal{A}}}{2k\cdot p_-}}\not{\epsilon}_\gamma\frac{e\not{k}\not{\mathcal{A}}}{2k\cdot p_+}$, which can, however, be shown to vanish.[11]

We note that $\mathfrak{a}$ and $\mathfrak{b}$ can in principle be evaluated explicitly for any combination of the spin projections s_+ and s_-, yielding usual complex numbers. Hence, the calculation can now be continued in full analogy to the scalar case. Switching to light-cone coordinates, evaluating three integrals and applying the Boca-Florescu transformation, we arrive at

$$\mathcal{S}^{(1/2)}_{p_+s_+,p_-s_-} = (2\pi)^3S_0\delta(Q^-)\delta^{(2)}(\mathbf{Q}^\perp)\int dx^-\tilde{\mathfrak{C}}(k^0x^-)e^{-iQ^0x^--iH(k^0x^-)} \tag{2.49}$$

with

$$\begin{aligned}\tilde{\mathfrak{C}}(\eta) &= \left[\tilde{\mathfrak{b}}f(\eta) + \tilde{\mathfrak{c}}f^2(\eta)\right]\mathcal{X}_{[0,2\pi]}(\eta)\,,\\ \tilde{\mathfrak{b}} &= \mathfrak{b} - \frac{k^0}{Q^0}h_1\,\mathfrak{a}\,,\quad \tilde{\mathfrak{c}} = -\frac{k^0}{Q^0}h_2\,\mathfrak{a}\,.\end{aligned} \tag{2.50}$$

to the factor p_-^0/p_-^-, the differential probability for the positron $d^3\mathscr{P}^{\mathrm{KG}}/(dE_{p_+}d^2\Omega_{p_+})$ is enhanced in the backward direction. Similarly, the electron differential probability $d^3\mathscr{P}^{\mathrm{KG}}/(dE_{p_-}d^2\Omega_{p_-})$, which includes a factor p_+^0/p_+^-, is also enhanced in the backward direction. This is no contradiction, but inherent to the definition of the differential probabilities.

[11] To this end, we write $\overline{\not{k}\not{\mathcal{A}}}\not{\epsilon}_\gamma\not{k}\not{\mathcal{A}} = \not{\mathcal{A}}\not{k}\not{\epsilon}_\gamma\not{k}\not{\mathcal{A}} = -\not{\mathcal{A}}\not{\epsilon}_\gamma\not{k}\not{k}\not{\mathcal{A}} = 0$, c.p. App. A.2.

Similarly to the scalar case [compare Eq. (2.30)], the pair-production probability is obtained as

$$\mathscr{P}^{(1/2)}_{s_+,s_-} = \frac{1}{2}\sum_{\lambda_\gamma}\int\frac{Vd^3p_+}{(2\pi)^3}\int\frac{Vd^3p_-}{(2\pi)^3}|\mathcal{S}^{(1/2)}_{p_+s_+,p_-s_-}|^2\,. \tag{2.51}$$

With Q^μ being independent of the particles' spin, the remaining steps are identical to the scalar case, and we arrive at

$$\mathscr{P}^{(1/2)}_{s_+,s_-} = \frac{\alpha m^2}{16\pi^2\omega_\gamma}\sum_{\lambda_\gamma}\int d^3p_+\frac{1}{p^0_+(k^-_\gamma - p^-_+)}\left|\int_0^{2\pi/k^0} dx^-\,\tilde{\mathfrak{C}}(k^0x^-)e^{-iQ^0x^- - iH(k^0x^-)}\right|^2\,. \tag{2.52}$$

This probability still depends on the spin projections s_+ and s_-. It describes the probability that the detector measures the particles with these spin projections. Note that the actual spin orientation of the produced particles does not necessarily coincide with these projections [BLP80, IKS05].

The full pair-production probability for Dirac particles is obtained by summing over all possible spin configurations

$$\mathscr{P}^{(1/2)} = \sum_{s_+,s_-}\mathscr{P}^{(1/2)}_{s_+,s_-}\,. \tag{2.53}$$

2.3.2 The spinor properties

When the full pair-production probability is regarded, the spin properties can be treated with the usual trace technique. This technique can be applied to expressions of the form

$$\mathcal{M}(p_+,p_-) = \sum_{s_+,s_-}\left|\overline{w}_{p_-s_-}\Gamma\, w_{p_+s_+}\right|^2 \tag{2.54}$$

where Γ denotes a general matrix acting on the spinors. As presented in App. A.4, this expression can be obtained as the trace

$$\mathcal{M}(p_+,p_-) = \mathrm{Tr}\left[\Gamma\left(\frac{\not{p}_+ - m}{2m}\right)\overline{\Gamma}\left(\frac{\not{p}_- + m}{2m}\right)\right]\,. \tag{2.55}$$

The spin projections are traced out, and the resulting expression can be evaluated analytically, independent of the actual representation of the spinors. This way, the pair-production probabilities can be evaluated numerically without the need to implement spinors and matrices.

In order to apply this scheme to our calculation, we investigate the structure of our expressions in more detail. We note that $\tilde{\mathfrak{C}}(k^0x^-)$ is the only component of the spin-resolved probabilities $\mathscr{P}^{(1/2)}_{s_+,s_-}$ [see Eq. (2.52)] which depends on the spin projections $s_\pm$. Revisiting $\tilde{\mathfrak{C}}(k^0x^-)$ in Eq. (2.50), we see that the spinors are included in $\tilde{\mathfrak{b}}$ and $\tilde{\mathfrak{c}}$, which are independent of the integration variable x^-. Thus, the integrals

$$I_j = \int_0^{2\pi/k^0} dx^-\,f^j(k^0x^-)e^{-iQ^0x^- - iH(k^0x^-)} \tag{2.56}$$

can be evaluated independently of the spin states, allowing us to write

$$\int dx^-\,\tilde{\mathfrak{C}}(k^0x^-)e^{-iQ^0x^- - iH(k^0x^-)} = \tilde{\mathfrak{b}}I_1 + \tilde{\mathfrak{c}}I_2\,. \tag{2.57}$$

Hence, the full probability can be expressed as

$$\mathscr{P}^{(1/2)} = \frac{\alpha m^2}{16\pi^2\omega_\gamma} \sum_{\lambda_\gamma} \int d^3p_+ \frac{1}{p_+^0(k_\gamma^- - p_+^-)} \sum_{s_+,s_-} \left|\tilde{\mathfrak{b}} I_1 + \tilde{\mathfrak{c}} I_2\right|^2 \tag{2.58}$$

where $\sum_{s_+,s_-}\left|\tilde{\mathfrak{b}} I_1 + \tilde{\mathfrak{c}} I_2\right|^2$ can be brought into the form suggested by Eq. (2.54). The explicit calculation comprises many terms and is presented in App. A.4.4.

3 Modeling the particle spectrum

This chapter contains a new model approach for the strong-field Breit-Wheeler process in laser pulses of moderate intensity. Based on concepts generalized from bichromatic fields, this model aims at multiphoton processes being induced by the spectral components of the pulse. Providing quantitative estimates for combined emission-absorption processes in different photon-number channels, it supports the understanding of the energy spectra of the produced particles and facilitates the detection of interferences between these channels. This way, we prepare the ground for the forthcoming investigations. The content of this chapter was originally published in [JM16a].

3.1 Introduction

As we have seen in the previous chapter, the three delta functions establish a connection between the energy of the gamma quantum and the momenta of the particles, but the contribution of the laser pulse remains undetermined except for the requirement that the transferred four-momentum can be expressed as a multiple of the laser four-momentum. This means that a given process is in principle possible if the transferred energy can be delivered by a combination of laser photons. We recall that the actually required laser energy has to be deduced externally by regarding the classical behavior of the charged particles in the laser field. The resulting expression remains compatible with the original constraints imposed by the delta functions.
Once the required energy for a given pair-production process is known, the question arises which combination of laser photons plays a dominant role for the process. In the following, we present our model approach which allows us to identify the dominant photon-number channels. Furthermore, the structure of the pair-creation spectra can be understood this way. In addition, this approach allows us to detect and understand interferences between different photon-number channels. The latter exhibit a distinct dependence on the carrier-envelope phase of the laser pulse, which shall be examined in detail in the next chapter.

3.2 Concepts from the multichromatic case

In order to understand the various production channels and the corresponding interferences facilitated by a pulse of moderate intensity, we revisit concepts known from explicit S-matrix calculations in bichromatic laser fields and apply them to a multichromatic field with M discrete modes. Finally, the case of a pulse with a continuous spectrum can be regarded as the limit of $M \to \infty$.

3.2.1 Pair-creation amplitude

We regard a multichromatic field composed of M discrete modes which propagate in a common direction and are polarized along a common axis. The latter property simplifies the notation, but it is not used explicitly in the analysis.[1] The modes are characterized by

[1]For example in [NF00], a bichromatic calculation has been presented for arbitrary angles between the polarization vectors.

means of their frequencies ω_j (which are assumed pairwise different), amplitudes a_j, and phase shifts δ_j. Suppressing the spatial dependence in the notation, the combined vector potential in dimensionless units reads

$$\xi(t) = \sum_{j=1}^{M} \xi_j \cos(\omega_j t - \delta_j) \tag{3.1}$$

with amplitude parameters $\xi_j = \frac{ea_j}{m}$.
Generalizing the procedure established for mono- and bichromatic fields (see, e.g., [NNR65, Rei80, Rit85, NF00, EKK09, JM13]), the pair-creation amplitude is Fourier decomposed as

$$\mathcal{S} = \sum_{n_1=-\infty}^{\infty} \cdots \sum_{n_M=-\infty}^{\infty} \mathcal{S}(n_1, \dots, n_M)\,, \tag{3.2}$$

with partial amplitudes which can be brought into the form

$$\mathcal{S}(\bar{n}) = \mathcal{S}_0(\bar{n})\, \delta(q_+^0 + q_-^0 - \omega_\gamma - \sum_{j=1}^{M} n_j \omega_j)\, e^{i\varphi(\bar{n})}\,. \tag{3.3}$$

Here, the multiindex $\bar{n} = (n_1, \dots, n_M)$ has been introduced to shorten the notation. The phase shifts of the field modes appear explicitly in the amplitude phase term

$$\varphi(\bar{n}) = \sum_{j=1}^{M} n_j \delta_j\,. \tag{3.4}$$

The creation of a pair with dressed particle energies $q_\pm^0$ requires the energy $q_+^0 + q_-^0 - \omega_\gamma$ to be absorbed from the laser field. The δ functions in the partial amplitudes allow only those processes, where this energy can be provided by a sum of integer multiples of the mode frequencies. At this point, despite the classical treatment of the laser field, the concept of laser photons comes into this consideration. As the photon numbers n_j in Eq. (3.2) are not necessarily positive, the creation of a pair can be accompanied by the emission of photons into the laser field [WX14, AVCM14]. For certain parameter constellations, in particular if the energy of the dominant laser modes exceeds the actually required energy, these can be the most probable production channels, as will be shown in an example below.
As a preparation for the following steps, we sort the various production channels by the total number N of photons being interchanged with the laser field. To this end, we introduce the symbol $|\bar{n}| = \sum_{j=1}^{M} |n_j|$ and rearrange the summation of the partial amplitudes in the form

$$\mathcal{S} = \sum_{\bar{n}} \mathcal{S}(\bar{n}) = \sum_{N=1}^{\infty} \sum_{|\bar{n}|=N} \mathcal{S}(\bar{n}) = \sum_{N=1}^{\infty} \mathcal{S}(N) \tag{3.5}$$

with the N-photon amplitude $\mathcal{S}(N) = \sum_{|\bar{n}|=N} \mathcal{S}(\bar{n})$ which accounts for processes involving a total number N of laser photons.

3.2.2 Probabilities and interferences

In the following, we shall investigate the corresponding pair-production probability which is obtained from the absolute square of the amplitude $\mathcal{S}$. Further continuing our approach, we divide the resulting expression into contributions with equal and non-equal photon numbers and obtain

$$|\mathcal{S}|^2 = \sum_N \left[\mathcal{S}(N)\mathcal{S}^*(N) + \sum_{N' \neq N} \mathcal{S}(N)\mathcal{S}^*(N')\right]. \tag{3.6}$$

The full pair-production probability follows as the integration over all possible particle states. At this point, we continue regarding the particle momenta as fixed external parameters and introduce the fully differential probabilities $\mathcal{P}_N = \mathcal{S}(N)\mathcal{S}^*(N)$ and $\mathcal{P}_{NN'} = \mathcal{S}(N)\mathcal{S}^*(N') + \mathcal{S}(N')\mathcal{S}^*(N)$. The latter describes interferences between channels of different photon numbers N and $N' \neq N$. However, as will be shown shortly, also the first term can contain interferences.

As a general criterion for interferences between two processes with photon combinations $\bar{n}$ and $\bar{n}'$, the total photon energies need to be identical [NF00, AM13, WX14, JM15], which means

$$\sum_{j=1}^{M} n_j\omega_j = \sum_{j=1}^{M} n_j'\omega_j \,. \tag{3.7}$$

Under this condition, both processes are induced by the same absorbed energy as well as the same absorbed momentum. Accordingly, the particles are produced in the same final states.[2] When a bichromatic field is employed, and when emission processes can be neglected, this criterion can only be fulfilled for $N \neq N'$.[3] However, in particular for a laser field with many modes, interferences can as well arise between channels with equal total numbers of interchanged photons, which we shall refer to as self-interferences (SI). Decomposing the N-photon probability at the level of individual photon contributions as characterized by $\bar{n}$ and $\bar{n}'$ in the form

$$\mathcal{P}_N = \sum_{|\bar{n}|=N} \left[\mathcal{S}(\bar{n})\mathcal{S}^*(\bar{n}) + \sum_{\substack{|\bar{n}'|=N \\ \bar{n}' \neq \bar{n}}} \mathcal{S}(\bar{n})\mathcal{S}^*(\bar{n}')\right], \tag{3.8}$$

we first recognize the ordinary N-photon probability $\mathcal{P}_N^{\mathrm{ord}} = \sum_{|\bar{n}|=N} \mathcal{S}(\bar{n})\mathcal{S}^*(\bar{n})$. The remaining term gives the (N-photon) self-interference probability

$$\mathcal{P}_N^{\mathrm{SI}} = \sum_{|\bar{n}|=N} \sum_{\substack{|\bar{n}'|=N \\ \bar{n}' \neq \bar{n}}} \mathcal{S}(\bar{n})\mathcal{S}^*(\bar{n}'), \tag{3.9}$$

which accounts for interferences between contributions of different combinations of the same total number N of photons. In contrast to the usual interferences between different photon-number channels, the self-interference terms are lacking a characteristic phase dependence, as will be discussed below.

[2] In principle, the angular momentum of the photons needs to be compensated by the particles, as well, and may thus induce different behavior depending on the difference between the number of absorbed photons, see also Sec. 5.1. This approach may provide further insight into the selection rule for interference effects in the total production rates formulated in [JM15], which was based on the analytical properties of the interference terms.

[3] In a bichromatic field with modes ω_1 and ω_2, condition Eq. (3.7) imposes the following restriction when the number of absorbed photons is supposed to be changed by an integer l (neglecting emission processes): $n_1\omega_1 + n_2\omega_2 \doteq (n_1 + l)\omega_1 + (n_2 - l)\omega_2 = n_1\omega_1 + n_2\omega_2 + l(\omega_1 - \omega_2)$. This can only be fulfilled for $l = 0$. However, this line of arguing breaks down when the net number n_j of photons interchanged with a given mode becomes negative, since the total number of absorbed photons then includes $|n_j|$.

In order to further approach the interference terms between channels of photon numbers N and $N' \neq N$, we assume that the complex phase $\arg[\mathcal{S}_0(\bar{n})]$ of the partial amplitudes remains constant under variations of the photon combination $\bar{n}$, except for phase jumps by π, i.e. changes in sign. For example, in the case of a bichromatic field with orthogonally polarized modes, this condition is fulfilled.[4] Thus, the interference term can be written in the form

$$\mathcal{P}_{NN'} = 2 \sum_{\substack{|\bar{n}|=N \\ |\bar{n}'|=N'}} |\mathcal{S}_0(\bar{n})||\mathcal{S}_0(\bar{n}')|\sigma_{\bar{n},\bar{n}'} \cos\left[\varphi(\bar{n}) - \varphi(\bar{n}')\right] , \tag{3.10}$$

where the δ functions are suppressed, and where $\sigma_{\bar{n},\bar{n}'} = \cos(\arg[\mathcal{S}_0(\bar{n})] - \arg[\mathcal{S}_0(\bar{n}')]) = \pm 1$ absorbs signs. At this point, the role of the optical phase shifts δ_j becomes apparent. They are included in the combined phases φ and can thus induce strong modulating effects on the interference terms. If the amplitude phases depend only on the total number N of exchanged photons, such that we may write $\varphi(\bar{n}) = \varphi(N)$, a common interference phase

$$\phi_{NN'} = \varphi(N) - \varphi(N') \tag{3.11}$$

can be introduced. In particular for the case of a pulse, several of its properties can be derived analytically and shall be presented below.

3.3 P model

Aiming at the energy spectra of the created particles in the multiphoton regime, we will now develop our model approach which produces quantitative estimates for the ordinary production channels introduced in the previous section. Neglecting the self-interference terms, this approach facilitates straightforward implementation and still accurately reproduces several properties of the actual particle spectra. Furthermore, it allows us to estimate the magnitude and phase of interference terms between different photon-number channels.

The name “P model” indicates that this approach is based on the probabilities of the various production channels. In Sec. 4.3.1, we will develop another approach starting from the S-matrix amplitudes, which is referred to as “S model”.

3.3.1 Definitions

In order to employ our previously developed concepts in the forthcoming derivation, we introduce the full pair-production probability $\mathscr{P}$ in the form

$$\mathscr{P} = \frac{1}{2} \sum_{\lambda_\gamma} \sum_{s_+,s_-} \int \frac{V d^3 p_+}{(2\pi)^3} \int \frac{V d^3 p_-}{(2\pi)^3} \mathcal{P} \, , \tag{3.12}$$

where $\mathcal{P}$ denotes the fully differential probabilities from Sec. 3.2.2. This way, also the partial probabilities for specific photon-number channels can be obtained from $\mathcal{P}_N$ or $\mathcal{P}_{NN'}$.

We will regard positron spectra which are defined as follows: For fixed positron emission direction, the pair-creation probabilities are evaluated for various positron energies. These

[4] Due to these sign changes, the typical interference phase term $\cos\left(\sum_j \Delta n_j \delta_j\right)$ obtained in a bichromatic field does not contain sufficient information to tell if the term leads to constructive or destructive interference.

results are then presented as a function of the required laser photon energy E_L. The corresponding differential probability is referred to by the symbol $d\mathscr{P}$, which is defined as

$$d\mathscr{P} = \frac{d^3\mathscr{P}}{dE_{p_+} d^2\Omega_{p_+}} \frac{\partial E_{p_+}}{\partial E_L} \,. \tag{3.13}$$

This definition can be applied for the full calculation (see previous chapter) and also for the partial probabilities from Sec. 3.2.2.[5]

3.3.2 Outline

The probability $\mathcal{P}_{\bar{n}}^{\mathrm{ord}} = \mathcal{S}(\bar{n})\mathcal{S}^*(\bar{n})$ can be understood as the probability to create a certain particle pair from the photon combination $\bar{n}$, without interferences. Regarding a specific energy spectrum, the actually produced pair is characterized by the required photon energy E_L. The model idea is to decompose the pair-creation probability into the probability $\varrho_{\bar{n}}(E_L)$ to find the specific photon combination $\bar{n}$ in the pulse spectrum, and the probability $p_{\bar{n}}(E_L)$ to create the pair from these photons. Accordingly, we begin with

$$d\mathscr{P}_{\bar{n}}^{\mathrm{ord}}(E_L) \approx p_{\bar{n}}(E_L)\varrho_{\bar{n}}(E_L) \,. \tag{3.14}$$

Similar to the δ function in Eq. (3.3), the quantity $\varrho_{\bar{n}}(E_L)$ determines if the laser field can in principle provide the required photon combination. Additionally, it accounts quantitatively for the spectral composition of the field. The field intensity then determines the pair-creation probability $p_{\bar{n}}(E_L)$.

In order to further develop the model, the pair-creation probability $p_{\bar{n}}(E_L)$ is assumed to be independent of the actual photon combination $\bar{n}$. Instead, only the total number of involved laser photons $N = |\bar{n}|$ is accounted for, allowing us to write $p_{\bar{n}}(E_L) \approx p_N(E_L)$. This way, the probability of the ordinary N-photon channel can be expressed in the form

$$d\mathscr{P}_{N}^{\mathrm{ord}}(E_L) \approx p_N(E_L)\varrho_N(E_L) \,, \tag{3.15}$$

where $\varrho_N(E_L) = \sum_{|\bar{n}|=N} \varrho_{\bar{n}}(E_L)$ is the probability to find any combination of N photons that sum up to the required energy E_L. At this point, the spectral properties of the laser field have effectively been separated from the pair-creation probability.

As a last simplification, the pair-creation probability $p_N(E_L)$ is assumed to be essentially determined by the perturbative intensity scaling [Rit85], which means

$$p_N(E_L) \approx \mathsf{p}_0\, \xi_{\max}^{2N} \,, \tag{3.16}$$

where p_0 can be regarded as a global prefactor for a given positron energy spectrum.

Following this approach, also interference terms can be modeled by

$$d\mathscr{P}_{NN'} \approx 2\, \mathsf{p}_0\, \xi_{\max}^{N+N'} \sqrt{\varrho_N \varrho_{N'}} \cos(\phi_{NN'}) \,, \tag{3.17}$$

[5] The definition in Eq. (3.13) differs from $\frac{d^3\mathscr{P}}{dE_L d^2\Omega_{p_+}}$, which includes up to two different positron energies for a given value of E_L. This is a purely kinematical effect which can be illustrated in the following example. Let us regard the creation of a pair with emission directions along the collision axis. In the c.m. frame, both particles have the same energies and propagate in opposite directions. When the same process is observed in a frame which is boosted along the collision axis, both particles may travel in the same direction, but with different energies. Next, we note that the kinematics of the process are invariant under exchange of the two particles, in particular the required energy remains the same. Thus, two different energy solutions arise for positrons being emitted in the same direction.

when sign changes induced by $\sigma_{\bar{n},\bar{n}'}$ in Eq. (3.10) are neglected. Accordingly, the global sign of the interference term remains undetermined.
As a next step, we will discuss the photon-finding probabilities ϱ_N, which shall be treated without further simplifications. Subsequent numerical examples will show that this model approach nicely reproduces various features of the particle energy spectra and allows us to detect and understand interference effects.
We note that a related model approach for pair-production in short pulses has been presented in [NSKT12]. There, the full probability is equally decomposed into multiphoton processes. Cross sections obtained in monochromatic fields are, as an approximation, convoluted with the pulse spectrum. In contrast, our approach emphasizes the spectral properties of the pulse, while the pair-production probabilities are approximated. Hence, the models are conceptually different.

3.3.3 Photon-finding probability

In the following, we shall determine the probabilities of multiphoton processes driven by a laser pulse with a continuous frequency spectrum. The pulse is assumed to be plane-wave fronted, with its electric field being described by a real-valued function $f(t)$. As before, the spatial dependence is suppressed in the notation.
We begin with the probability to find a single photon of given energy ω in the pulse spectrum. To this end, we regard the total pulse energy $\mathcal{E}$ and apply Plancharel's theorem in the form

$$\mathcal{E} \sim \int_{-\infty}^{\infty} dt\, |f(t)|^2 \sim \int_{0}^{\infty} d\omega |\hat{f}(\omega)|^2 \tag{3.18}$$

where $\hat{f}(\omega) = \int_{-\infty}^{\infty} f(t) e^{i\omega t} dt$ denotes the Fourier transform of $f(t)$. Our results will be normalized in the end, allowing us to drop the prefactors for a moment. This equation can be read in the form $d\mathcal{E} \sim |\hat{f}(\omega)|^2 d\omega$ and thus allows us to deduce the spectral energy density $|\hat{f}(\omega)|^2$. Introducing photons to this initially classical calculation, we obtain the photon number density $\frac{1}{\omega}|\hat{f}(\omega)|^2$. Employing a proper normalization, these steps give rise to the probability density

$$\varrho(\omega) = \frac{1}{N_\varrho} \frac{1}{\omega} |\hat{f}(\omega)|^2 \tag{3.19}$$

to find one photon of frequency ω in the pulse spectrum, which will be referred to as photon-finding probability. The normalization condition requires $N_\varrho = \int_0^\infty \frac{1}{\omega}|\hat{f}(\omega)|^2 d\omega$. At this point, one-photon processes can be accessed via the P model, since $\varrho_1(\omega) = \varrho(\omega)$.
Next, we regard the probability to find any combination of $N > 1$ photons that sum up to the energy ω. When emission processes can be neglected, the corresponding probability density reads

$$\varrho_N(\omega) = \frac{1}{N!} \int d\omega_1 \int d\omega_2 \cdots \int d\omega_N\, \varrho(\omega_1)\varrho(\omega_2)\cdots\varrho(\omega_N)\, \delta\Big(\omega - \sum_{j=1}^{N} \omega_j\Big)\,, \tag{3.20}$$

with the frequencies being assumed pairwise different, and $\varrho(\omega)$ being defined to vanish for non-positive frequencies. In particular with regard to numerical evaluations, it is convenient to recast this expression into the recursive form

$$\varrho_N(\omega) = \frac{1}{N} \int_0^{\omega} d\omega' \varrho(\omega - \omega')\varrho_{N-1}(\omega')\,. \tag{3.21}$$

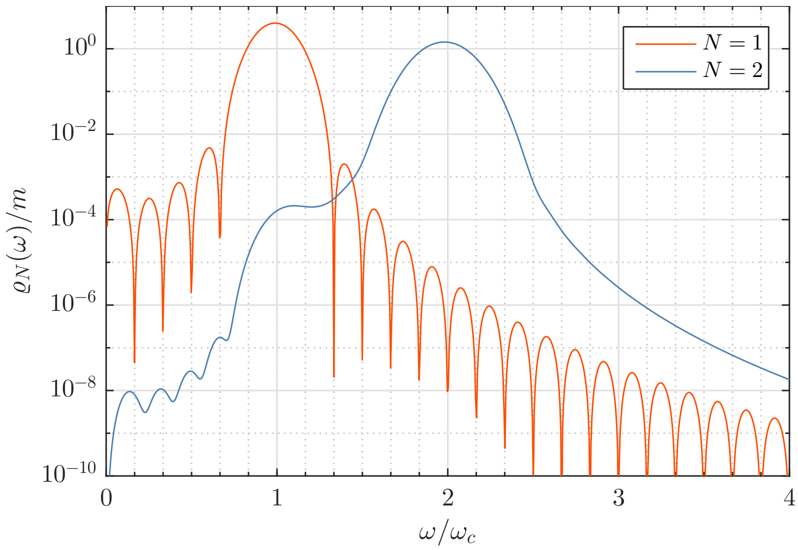

Figure 3.1: Photon-finding probability densities $\varrho_N(\omega)$ for $N = 1$ (red) and $N = 2$ (blue) based on Eq. (3.21), i.e. without emission processes, for a short pulse pulse with a shape function given by Eq. (2.11) with $N_{\text{osc}} = 6$, $\omega_c = m$ and $\chi = 0$. Subticks indicate integer multiples of the basic frequency $\omega_b = \omega_c/N_{\text{osc}}$.

This quantity will be referred to as multiphoton-finding probability and allows us to estimate the probabilities of ordinary multiphoton channels with arbitrary high photon numbers. Due to the recursive form, increasing the photon number by one requires one further integration.

In Fig. 3.1, we present a typical example of the one- and two-photon-finding probability densities obtained for our standard pulse shape given by Eq. (2.11). For the one-photon case, the probability is sharply peaked at the central pulse frequency ω_c. The characteristic zeros in ϱ_1 at most integer multiples of the basic frequency $\omega_b = \omega_c/N_{\text{osc}}$ are caused by the window function $\mathcal{X}_{[0,2\pi]}(\eta)$, see App. A.6. In contrast, the two-photon probability has its maximum at $\omega = 2\omega_c$, where processes may be induced by two of the most-probable photons with frequencies around ω_c. As a general property following from the folding structure, the dominant peak becomes broader and the finer structure disappears as the photon number is increased.

Finally, we include emission processes, which can be treated in analogy to general absorption and stimulated emission processes. Neglecting degeneracies, the probabilities of both processes are the same, and proportional to the photon density at the transition frequency. Following our model approach, we assume the corresponding pair-creation probabilities $p_{\bar{n}}$ to be well approximated by p_N, such that only the photon-finding probabilities have to be generalized. To this end, we include negatively weighted photons into the summation of N photons with total energy ω via

$$\varrho_N(\omega) = \frac{1}{N}\int_{-\infty}^{\infty} d\omega' \varrho(|\omega - \omega'|)\varrho_{N-1}(|\omega'|)\,. \tag{3.22}$$

After this step, also emission processes are covered by the P model. Their importance can be estimated by numerically comparing Eqs. (3.21) and (3.22) and will be discussed in Sec. 3.4.2.

3.4 Numerical examples

The following two examples will demonstrate the performance of the P model. We begin with a typical positron spectrum [cp. Eq. (3.13)] obtained in a six-cycle, medium-intensity pulse with $\xi_{\max} = 0.1$ revealing clear signatures of multiphoton processes. The second example focuses on emission processes occurring in a pulse of significantly higher amplitude and frequency. All examples in the present and in the following chapter are based on the full Dirac equation and are summed over the spin configurations of particles.
The numerical calculations are carried out in a frame of reference where the central laser frequency and the gamma-quantum energy are of the same order. The corresponding experimental parameters could be realized by employing a Nd:YAG laser with $\omega_c \approx 2.4$ eV and peak intensity $\sim 10^{17}$ W/cm^2. Additionally, gamma quanta of ~ 300 GeV are required, which could in principle be created by Compton backscattering off an ultra-energetic electron beam. The required energies are within the intended scope of XCELS [XCE].

3.4.1 Multiphoton processes

Figure 3.2 depicts our first exemplary positron energy spectrum (black line) as a function of the absorbed laser photon energy E_L in units of the central laser frequency ω_c. The corresponding positron energy is indicated at the top axis. The energy spectrum exhibits a series of broad peaks centered around integer values of E_L/ω_c (see also [HIM10, JSL$^+$12, KK12a, KGA14]). Especially for higher energies, additional fast oscillations occur. As a general trend, the spectrum decays rapidly as the energy grows.
In the following, we shall see how the P model can reproduce these properties and thus support their understanding. We begin with the model estimate for the one-photon channel, which is obtained from the pulse spectrum and amplitude as described above. The remaining parameter p_0 is determined by fitting the model expression to the high-energy part of the positron spectrum, which yields $\mathsf{p}_0 \approx 7.0 \times 10^{-5}$. The red line in Fig. 3.2 depicts the resulting estimate, which agrees nicely with the pair-production probability in the low- and high-energy parts of the spectrum.
The energy dependence of the model estimate reflects the spectral composition of the pulse. Accordingly, a dominant peak occurs at the central frequency ω_c, while higher photon energies are accompanied with much smaller probabilities. The fast oscillations are induced by the finite length of the pulse and are addressed in further detail in App. A.6.
Comparing the actual pair-production spectrum and the model expression for the one-photon channel, the approximate shape of the first broad peak at $E_L \approx \omega_c$ and also of the neighboring subpeaks are nicely reproduced. In the high-energy part, almost complete agreement is found for a broad range of energies comprising many fast oscillations.[6] Based on the good agreement, positrons at both ends of the spectrum are understood to be produced via absorption of one laser photon.
Including higher photon numbers, also the central part of the spectrum can be reproduced to good extent by our model. For the parameters under investigation, the contributions of emission processes are negligible. Employing the same value for p_0 as for the one-photon channel, the model estimates for the two-, three- and four-photon channels agree well with the broad peaks at $E_L/\omega_c \approx 2, 3$ and 4. The latter exhibit an oscillating substructure which becomes increasingly pronounced for higher photon numbers and will be addressed

[6] Note that dressing effects are relevant here. When they are neglected while determining the absorbed energy E_L, the fast oscillations are offset.

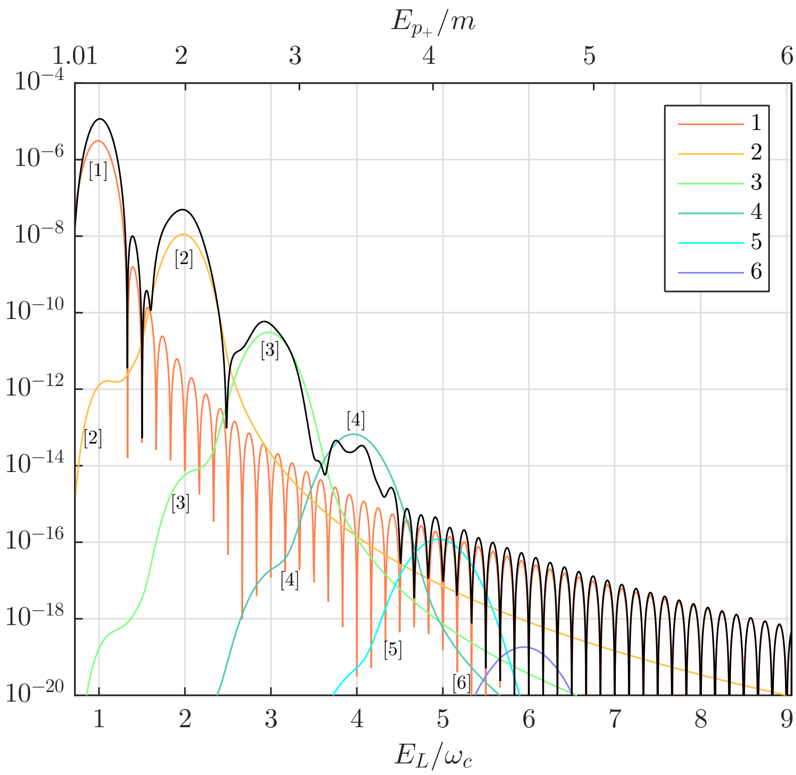

Figure 3.2: Energy spectrum of positrons $d\mathscr{P} = \frac{d^3\mathscr{P}}{dE_{p_+}d^2\Omega_{p_+}}\frac{\partial E_{p_+}}{\partial E_L}(E_L)$ (black line) in units of $1/m$ as a function of the required laser photon energy E_L in units of the central laser frequency ω_c. Top axis shows the corresponding positron energy. Colored lines depict model estimates for partial probabilities induced by the absorption of different numbers N of laser photons as indicated in the legend and by the symbols $[N]$. These positrons with $\varphi = \frac{\pi}{4}$, $\vartheta = 0.3\pi$ result from the head-on collision of a laser pulse with $\xi_{\max} = 0.1$, $N_{\text{osc}} = 6$, $\omega_c = 0.9m$ and $\chi = 0$ and a gamma quantum of energy $\omega_\gamma = 3.015m$. Originally published in [JM16a].

in Sec. 4.2. Again, the good agreement allows us to identify the dominant pair-production channels with corresponding multiphoton peaks.
The global structure of the particle spectrum is determined by the interplay between the perturbative intensity scaling and the fall-off of the photon-finding probability, which scales as $(E_L/\omega_c)^{-9}$ for the current pulse profile. For the parameters employed in Fig. 3.2, the model expressions for the five- and six-photon channels lie clearly below the one-photon tail, implying that these channels are only of minor importance. Consequently, the number of absorbed laser photons of the dominant pair-production channel at a certain required photon energy E_L cannot necessarily be deduced from the ratio E_L/ω_c alone.
This example has shown that the P model works well, which reveals that the structure of the particle spectrum is strongly determined by the pulse spectrum.

3.4.2 Emission processes

In order to enhance the relative importance of emission processes in this example, the laser amplitude and frequency are increased significantly with $\xi_{\max} = 0.5$ and $\omega_c = 3.6m$. The resulting positron spectrum is depicted in Fig. 3.3 (black line) and compared to model

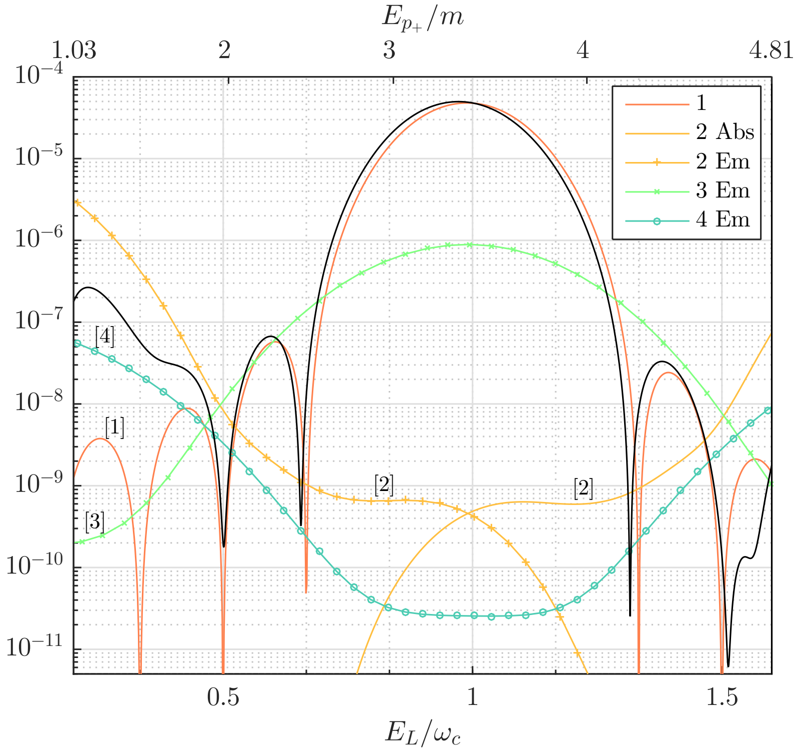

Figure 3.3: Positron energy spectrum $d\mathscr{P}$ (black line) in units of $1/m$ obtained for $\omega_c = 3.6m$ and $\xi_{\text{max}} = 0.5$ in order to demonstrate emission processes at low energies. Remaining parameters are identical to Fig. 3.2. The colored lines depict model estimates for processes involving a total number N of laser photons, where N is indicated in the legend and by the labels $[N]$. The solid lines correspond to absorption-only processes, while the symbol lines show processes where at least one photon is emitted into the laser wave. The model expressions for the three and four photon absorption-only processes are too small to be seen here. Subticks indicate laser photon energies E_L which correspond to integer multiples of the laser basis frequency ω_b. Originally published in [JM16a].

estimates for various production channels. The indicated photon numbers denote the total number of photons being interchanged with the laser field. The model expressions are presented both for the absorption-only case (solid lines) and for the case in which at least one photon is emitted (symbol lines). Unlike in the previous example, the remaining parameter p_0 was chosen in order to obtain good agreement at the one-photon peak, with $\mathsf{p}_0 \approx 1.7 \times 10^{-4}$.

When emission processes are included in a production channel of fixed total number of involved photons, additional broad peaks appear at lower energies. Since emitting instead of absorbing one photon reduces the resulting energy by two photon energies, these peaks are offset by an even number of central frequencies from the major peak in the absorption-only case.

As Fig. 3.3 shows, the pair-production probabilities in the low-energy part of the positron spectrum exceed the model estimate for the one-photon channel by more than two orders of magnitude, in particular when the required energy falls into the spectral hole at $\omega_c/3 = 2\omega_b$ (see red curve in Fig. 3.1). Instead, significant contributions arise from channels with two or four photons, where one or two photons are emitted into the laser wave. In

this scenario, even smallest fractions of the enormous central frequency are sufficient to produce a particle pair. Thus, the low-energetic positrons are predominantly produced via absorbing one photon of the central laser frequency and releasing the excess energy by emitting another photon into the laser field.
When the laser amplitude is reduced, the relative weight of processes with higher photon number decreases, and the particle spectrum approaches the shape of the one-photon channel.

3.5 Conclusion

In this chapter, we have presented a new quantitative model for the SFBW process driven by a short laser pulse with medium intensity. The good performance of our model approach shows, besides, that for $\xi_{\max} < 1$, the process can indeed be understood as being induced by individual photons stemming from the pulse. For higher field intensities $\xi_{\max} \gg 1$, the SFBW process increasingly resembles the Schwinger effect, which is rather sensitive to the local field strength [Rit85, MKDP16]. Therefore, our approach explicitly aims at medium intensities. The model supports the understanding of the pair-production process and shall be employed as a basic tool for the following investigations. In principle, it can be applied to other multiphoton processes driven by laser pulses, as well, and can easily be extended to higher photon numbers.
Regarding the SFBW process, we have investigated the energy spectra of the produced particles, which possess a rich structure. Employing our multiphoton approach, the position of the main peaks and their approximate shapes can be understood. Besides, fine structures were observed in some of the peaks. They will be addressed in the following chapter, revealing carrier-envelope-phase and interference effects.

4 CEP and interference effects

This chapter contains a detailed investigation of the effects caused by the carrier-envelope phase (CEP) of the laser pulse on the pair-creation probability in the multiphoton regime. The CEP is introduced as the relative phase between the pulse envelope and the underlying harmonic oscillation, cp. Eq. (2.11). Thus, it directly affects the temporal shape of the resulting pulse. This effect is depicted in the left panel of Fig. 4.1, where we present the pulse shape $f'(\eta)$ for a pulse with $N_{\mathrm{osc}} = 6$ field cycles and two distinct values of the CEP. Furthermore, and more important for us, the CEP also affects the spectral properties of the pulse. The corresponding spectral densities are presented in the right panel of Fig. 4.1.[1] While the broad central peak remains virtually invariant under variations of the CEP χ, the spectral density depends on χ at both ends of the spectrum. Additionally, as will be discussed in the following section, the CEP leaves characteristic imprints on the quantum phases of the different pair-production channels. As a consequence, interference terms obtain a distinct CEP dependence, which facilitates their detection.
We will first continue our analytical approach in order to understand the effects of the CEP on the pair-creation spectra. As a next step, these effects will be investigated in detail by regarding numerically computed examples, where interferences between different production channels can be detected.
Finally, we will regard interference effects driven by continuous spectra from a slightly more distanced view. In this context, the role of self-interference terms shall be addressed, as well as the question to which extent the unavoidable spectral broadening of radiation sources affects interference effects. The contents of Secs. 4.1 and 4.2 were originally published in [JM16a].

4.1 CEP effects: Analytical approach

In order to develop an analytical approach to effects caused by the carrier-envelope phase, we will first generalize the multichromatic field to the case of a pulse with a continuous spectrum. In particular, we will establish a connection between the phase shifts δ_j, which are crucial for interferences, and the spectral phase of a pulse. Next, the effects of the CEP on the spectral phase and on the pulse spectrum in general will be discussed. Finally, these findings will be combined with our concepts developed in Chap. 3 in order to understand the effects of the CEP on the pair-creation process.

4.1.1 Continuous generalization of the multichromatic field

As we shall see in the following, the multichromatic field as introduced in Eq. (3.1) can straightforwardly be generalized to the case of a continuous spectrum. To this end, we regard a plane-wave fronted pulse being defined by its vector potential $A(t)$, again dropping the spatial dependence in the notation. Its Fourier decomposition can be brought into the

[1] Here, "spectral density" refers to the absolute value squared of the Fourier transform of f'. We note that the visual appearance of the zeros in the spectral density depends on the choice of the numerical grid. Different to other plots such as Fig. 3.1, the grid employed in Fig. 4.1 was chosen in order to match the zeros.

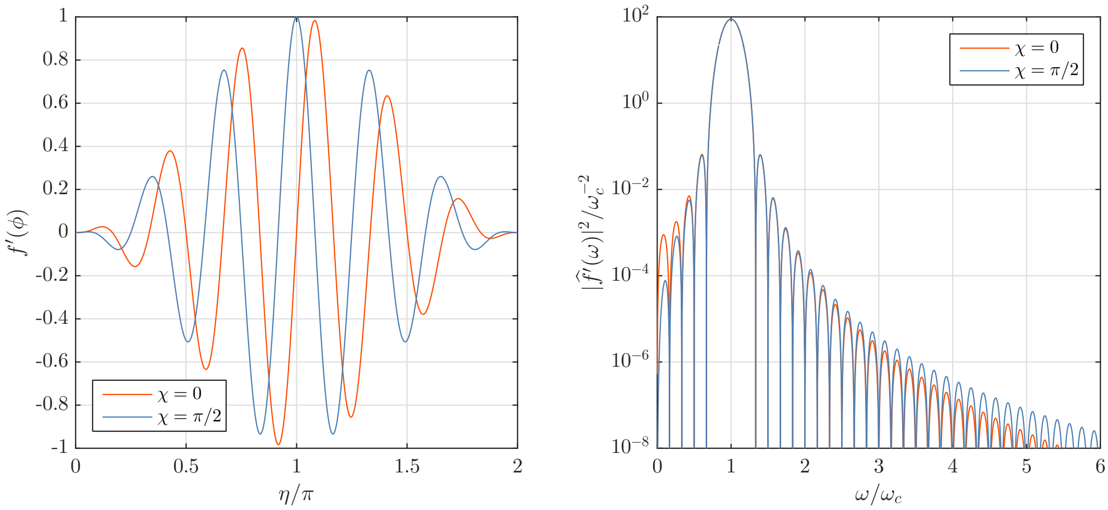

Figure 4.1: Pulse shape as determined by Eq. (2.11) for different values of the CEP χ in real space (left) and Fourier space (right). Here, we regard a pulse with $N_{\text{osc}} = 6$ field cycles. Due to the factor ω_c^2, the rescaled Fourier transforms are independent of the central frequency ω_c.

form

$$A(t) = \frac{1}{\pi} \int_0^\infty |\hat{A}(\omega)| \cos(\omega t - \phi_\omega) d\omega \tag{4.1}$$

which can already be considered the continuous generalization of the multichromatic field in Eq. (3.1). The comparison also shows that the phase shift δ_j can be associated with the spectral phase $\phi_\omega = \arg \hat{A}(\omega)$ of the corresponding frequency mode. The latter can as well be expressed by the spectral phase of the electric field $E(t)$, leading to the relation

$$\delta_j \mathrel{\widehat{=}} \arg \hat{A}(\omega) = \arg \hat{E}(\omega) - \pi/2\,. \tag{4.2}$$

4.1.2 CEP signatures in the pulse spectrum

The effect of the CEP on the pulse spectrum will now be investigated for the exemplary case of a plane-wave fronted pulse with an electric field of the form

$$E(t) \sim f_{\text{env}}(t) \cos(\omega_c t + \chi)\,. \tag{4.3}$$

The shape of this pulse is determined by the envelope function $f_{\text{env}}(t)$ which is independent of the CEP χ. The pulse spectrum can be written as

$$\hat{E}(\omega) \sim \hat{f}_{\text{env}}(\omega + \omega_c) e^{i\chi} + \hat{f}_{\text{env}}(\omega - \omega_c) e^{-i\chi} \tag{4.4}$$

which reveals the explicit dependence on the CEP.
The CEP dependence becomes particularly straightforward, if the first term can be neglected, which requires two conditions: (i) the spectral width of the pulse needs to be small, i.e. the pulse length should not be extremely short; (ii) the regarded frequencies ω should be close to the central frequency ω_c. Under these assumptions, the spectral phase depends linearly on the CEP, while the photon density remains invariant.
In the general case, for example in the high-energy part of spectrum, both the spectral phase and the photon density exhibit a more complicated CEP dependence. The properties of our standard pulse shape are discussed in more detail in App. A.6.

4.1.3 CEP effects in the energy spectra of the produced particles

Our previously developed concepts shall now be combined in order to understand the influence of the CEP on the pair-production spectra. To this end, the pulse shape can remain unspecified, but the spectral width is assumed to be in accordance with condition (i). As a consequence, the simplified CEP dependence applies for those processes which are induced by photons with frequencies around the central frequency. Regarding the particle spectra, this condition is fulfilled in an interval which begins at $E_L \approx \omega_c$ (when emission processes can be neglected). It typically comprises several multiphoton peaks and extends to the energy where the one-photon process becomes noticeable again.
In this inner part of the spectrum, the relevant multiphoton-finding probabilities are essentially independent of the carrier-envelope phase. Conversely, the linear CEP dependence of the spectral phase is conveyed to the phase shifts, which modulate the interference terms. If the envelope function is invariant under time reversal ($t \to -t$), its Fourier transform is real-valued, such that neighboring modes are subject to the same spectral phase, except for phase jumps by π which are caused by sign changes. This allows us to continue combining individual channels into photon-number channels. Regarding interference terms between (absorption-only) channels with N and N' photons, we can thus deduce that the interference phase [cp. Eq. (3.11)] obtains a $(N - N')\chi$ dependence.[2] Depending on the probabilities of the participating channels, this phase can lead to pronounced interference effects with a distinct signature. When emission processes are included, the interference phase can in principle be treated similarly to the absorption-only case, but, as seen in Eq. (3.4), the phase of emitted photons contributes with inverted sign. On the other hand, self-interference terms cannot be detected this way, since the CEP dependence of their phase vanishes identically.
In the outer parts of the spectrum, additional CEP effects are caused by the high-energy CEP dependence of the photon density, which directly affects the resulting pair-production probabilities. Furthermore, also the interference phases can become more involved.
The following numerical examples are based on our usual pulse shape in Eq. (2.11) which fulfills the above criteria.

4.2 CEP and interference effects: Numerical examples

Guided by our analytical approach, we will now inspect CEP effects occurring in numerically computed particle spectra, in particular aiming at interference effects.

4.2.1 Detailed examples

In Fig. 4.2, we present numerically computed positron spectra for various values of the CEP χ at constant maximum pulse amplitude ξ_{max}. Following the P model, this normalization is chosen in order to keep the probabilities of the dominant production channels constant. The pulse energy, however, depends on χ. The panels depict positron spectra for increasing values of the pulse amplitude with $\xi_{\mathrm{max}} = 0.05$ (left), $\xi_{\mathrm{max}} = 0.1$ (center) and $\xi_{\mathrm{max}} = 0.2$ (right). Each increment of ξ_{max} leads to one more multiphoton peak before the one-photon tail begins. These last peaks correspond to photon numbers $\tilde{N} = 3, 4$ and 5, respectively. As expected from our previous discussion, the CEP induces local modifications in the particle spectra, while their overall structure as determined by the multiphoton peaks and the one-photon tail is preserved. Quantitatively strong CEP effects arise between

[2]Further details concerning the sign changes will be discussed in Sec. 4.2.2 below.

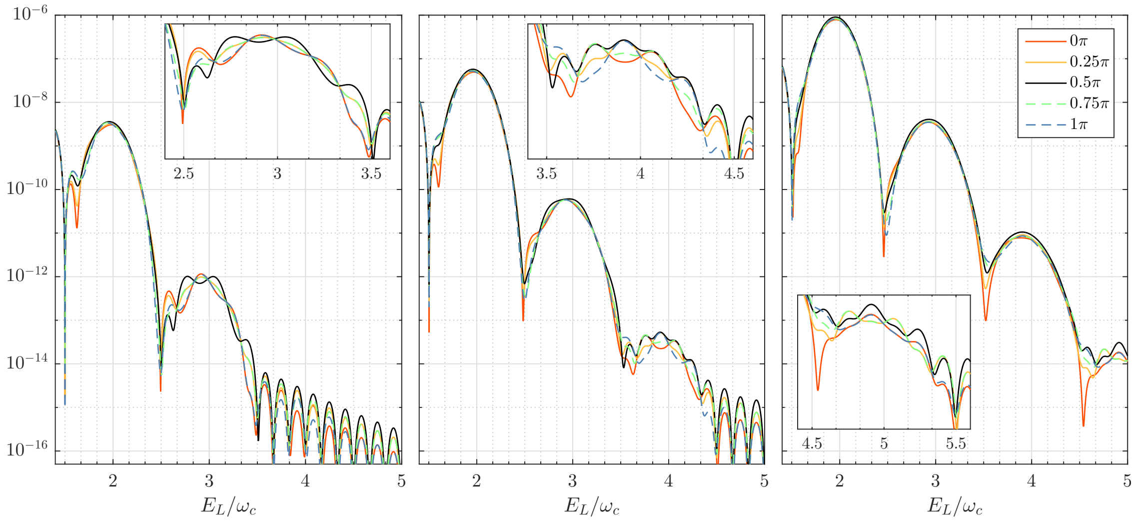

Figure 4.2: Positron energy spectra $d\mathscr{P}$ in units of $1/m$ for various values of the carrier-envelope phase as indicated in the legend and for $\xi_{\max} = 0.05$ (left), $\xi_{\max} = 0.1$ (center) and $\xi_{\max} = 0.2$ (right). Remaining parameters are the same as in Fig. 3.2. The inlets show the respective last multiphoton peak before the one-photon tail begins. Subticks indicate laser photon energies E_L which correspond to integer multiples of the laser basis frequency ω_b. Originally published in [JM16a].

neighboring multiphoton peaks, affecting the pair-creation probability by about one order of magnitude. As depicted in the inlets, the peaks associated with $\tilde{N}$ are modulated by small oscillations with a scale given by the laser basic frequency ω_b. These oscillations, as well as the one-photon tail, exhibit also a strong dependence on the CEP.

In the following, these effects shall be explained by employing our recently developed concepts. With $N_{\text{osc}} = 6$, the pulse shape complies with condition (i). Condition (ii) is fulfilled for those processes which are not affected by the high-energy CEP dependence of the one-photon channel, which begins at $E_L \approx 3\omega_c$ (cp. Fig. 4.1). The appearance of the corresponding CEP effects depends on the strengths of the competing multiphoton channels. For $\xi_{\max} = 0.05$ (left panel), the inner part of the particle spectrum can thus be extended to $E_L \approx 3.5\omega_c$. For the stronger laser amplitudes employed in the center and the right panel, the upper extent can be chosen as $E_L \approx 4.5\omega_c$.

In the inner parts, the distinct CEP effects can be attributed to interference effects. At energies in between the broad multiphoton peaks, the probabilities of neighboring multiphoton channels are of the same order. Thus, strong interference terms arise, with their phase revealing a linear dependence on the CEP. This is the main origin of the CEP effects which are visible at energies $E_L \gtrsim 1.5\omega_c$ in all panels of Fig. 4.2, at $E_L \gtrsim 2.5\omega_c$ in the center and right panel and at $E_L \gtrsim 3.5\omega_c$ in the right panel. The CEP effects were checked by a Fourier analysis of $d\mathscr{P}(\chi)$ for constant values of E_L. They can become more involved when interferences with other photon-number channels become noticeable.

The broad multiphoton peaks are also subject to interference effects. For a given particle spectrum, the interferences become stronger as the number of photons grows. This can already be anticipated from Fig. 3.2, where the difference between the probabilities of the photon-number channels can be seen to decrease for higher photon numbers. Conversely, regarding a given multiphoton peak, increasing the pulse amplitude $\xi_{\max}$ enhances this difference and thus weakens the interference effects. The small spectral oscillations disappear as well, which leads to the conclusion that they are mainly caused by interferences. When the ordinary interferences are suppressed due to the lack of competing processes, effects caused by self-interference terms could be expected to become visible. However, the isolated multiphoton peaks are almost invariant under the CEP, which is in good agreement with our analytical approach predicting the corresponding interference phase to be independent of the CEP. On the downside, this means that these terms cannot be accessed in this analysis.

The peak associated with $\tilde{N}$ exhibits particularly strong CEP effects (see the inlets of Fig. 4.2). Here, interferences arise predominantly between the channel with $\tilde{N}$ photons and the one-photon channel, with their interference phase revealing a $(\tilde{N}-1)\chi$ dependence. These interferences are the main origin of the CEP sensitivity of the spectral oscillations. In the right panel, the high-energy CEP dependence of the one-photon channel additionally enhances the pair-creation probability for $\chi = \pi/2$ as compared to $\chi = 0, \pi$. Therefore, the inner part of this spectrum is defined to end at $E_L \approx 4.5\omega_c$.

The corresponding spectral oscillations shall now be discussed in more detail. In the left panel, they almost disappear for $\chi = \pi/4$ and $\chi = 3\pi/4$. With their original periodicity being $\omega_b/2$, the remaining pattern has a periodicity of ω_b. The center panel reveals a similar behavior, with smallest deviations from the original shape of the multiphoton peak for $\chi = \pi/2$. In the right panel, the corresponding situation would appear for $\chi = \pi/8$ (not shown).

These observations can be traced back to the finite temporal length of the pulse profile, which leaves strong signatures in the entire pulse spectrum. The Fourier transform of the characteristic function is of the form $\mathrm{sinc}(\pi\omega/\omega_b)$. As a consequence, the photon density vanishes at integer values of E_L/ω_b (except for energies in the main central peak; see. Fig. 3.1), while the spectral phase jumps by π (cp. App. A.6). Both of these effects are reflected in the particle spectra: The one-photon process is clearly affected by the zeros of the photon density, and the interference phases obtain a discrete energy dependence (see the following subsection for further details).

Hence, the shape of the spectral oscillations is determined by the one-photon channel and additionally modulated by the energy-dependent interference phase. The latter is of the form $(\tilde{N} - 1)\chi + j\pi$, where the integer j is increased when E_L passes an integer multiple of ω_b. When the interference term vanishes for a certain CEP, the remaining oscillatory pattern arises due to the incoherent addition of the one-photon channel on top of the multiphoton peak.

The one-photon tail lies in the outer part and exhibits CEP effects which are mostly caused by the high-energy CEP dependence of the photon density. In addition, they can arise from interferences involving, for example, the weak channel with $\tilde{N} + 1$ photons.

4.2.2 Further details on the interference terms

In the following, the interference phases will be discussed in more detail. We begin by addressing the jumps of the spectral phase caused by the finite length of the pulse.

Let us regard the interference terms in Eq. (3.10), which are modulated by the phases $\varphi(\bar{n})$. The latter are determined by the spectral phases of the involved photons [cp. Eq. (4.2)]. In the inner part of the particle spectrum (cp. Sec. 4.1.3), the spectral phase of a relevant photon with frequency $\omega \equiv \omega_j$ is given by

$$\phi_{\omega_j} = -\chi + \ell_j\pi + \mathrm{const}\,. \tag{4.5}$$

The integer ℓ_j is zero for $\omega_j \approx \omega_c$ and counts the number of sign changes which occur whenever ω_j passes integer multiples of the basic frequency ω_b outside the the main peak, which is situated in the interval $(\omega_c - 2\omega_b, \omega_c + 2\omega_b)$, see Figs. 3.1 and 3.3. The constant introduced in Eq. (4.5) is independent of ω_j and χ. For any given photon combination $\bar{n}$ of N photons, we define the total number of sign changes $\ell_{\bar{n}} = \sum_{j=1}^{N} \ell_j$.
The full interference term in Eq. (3.10) can now be decomposed into contributions from different photon combinations $(\bar{n}, \bar{n}')$ which shall be sorted by the number of sign changes $\Delta\ell_{\bar{n},\bar{n}'} = \ell_{\bar{n}} - \ell_{\bar{n}'}$. Here, we can also account for $\sigma_{\bar{n},\bar{n}'}$ [see Eq. (3.10)], which can induce further sign changes. Altogether, the full interference term $\mathcal{P}_{NN'}$ can now be separated into two contributions: one with constructive interference, the other one with destructive interference. With $\Delta\ell_{\bar{n},\bar{n}'}$ being independent of χ in the inner part, and assuming the same for $\sigma_{\bar{n},\bar{n}'}$, both interference terms obtain an effective interference phase of $(N - N')\chi$.
When the high-energy CEP dependence has to be taken into account (see e.g. the right panel of Fig. 4.2), i.e. when the first term in Eq. (4.4) has to be included, the interference phase can deviate from the linear CEP dependence. However, in our numerical computations, these deviations were found to have only small impact on the appearance of the corresponding cosine term.

4.3 Interference processes driven by continuous spectra

In this section, we will regard interferences between multiphoton processes driven by a continuous spectrum from a more generalized viewpoint. We will first discuss the relevance of self-interference terms (i.e. interferences between processes with equal total numbers of photons) in a general field with a continuous spectrum. To this end, we develop an alternative model approach in close analogy to the P Model, with the major difference being that the present model is based on the amplitude of the process, rather than the probability. This model supports the understanding of the special role played by self-interference terms.
Afterwards, we will briefly discuss the situation of a bichromatic field, which is a workhorse for theoretical studies on interference effects in strong-field QED (see, e.g., [NF00, KK12c, AM13, JM15]). We will address the question to which extent the spectral broadening of the fields, which is unavoidable in actual experiments, may affect the appearance of interference effects.

4.3.1 S model

In order to approach self-interference terms, a model similar to the P model shall now be developed based on the S-matrix amplitude. As before, we begin with a multichromatic field and regard the one-photon amplitude $\mathcal{S}(N=1)$ which has been introduced in Eq. (3.5). In analogy to the decomposition employed in Eq. (3.3), we bring $\mathcal{S}(N=1)$ into the form

$$\mathcal{S}_1 = \sum_{j=1}^{M} s(j)\, \delta(q_+^0 + q_-^0 - \omega_\gamma - \omega_j)\, \xi_j \,. \tag{4.6}$$

Here, however, the perturbative intensity scaling is expressively taken into account, while the phase shifts $e^{i\delta_j}$ have been absorbed into the factor $s(j)$. The transition to a continuous spectrum is achieved via $\sum_j \xi_j \to \int_0^\infty |\xi(\omega)| d\omega$, with $\xi(\omega) = \frac{1}{\pi} \int_{-\infty}^{\infty} \xi(t) e^{i\omega t} dt$, which yields

$$\mathcal{S}_1 = \int_0^\infty d\omega\, s(\omega)\, \delta(q_+^0 + q_-^0 - \omega_\gamma - \omega)\, |\xi(\omega)|\,. \tag{4.7}$$

Effectively, the δ function disappears after this step. This is in line with the observation that employing a pulse instead of a multichromatic field leads to three instead of four δ functions in the S matrix.

In the same manner, the N-photon amplitude $\mathcal{S}(N)$ can be expressed (for absorption-only processes) as

$$\begin{aligned}\mathcal{S}_N = \frac{1}{N!}\int_0^\infty d\omega_1 \ldots \int_0^\infty d\omega_N\, s(\omega_1,\ldots,\omega_N)\, \delta(q_+^0 + q_-^0 - \omega_\gamma - \sum_{j=1}^N \omega_j) \\ \times |\xi(\omega_1)| \ldots |\xi(\omega_N)|\,.\end{aligned} \tag{4.8}$$

This expression has the same convolution structure as the multiphoton-finding probability in Eq. (3.20). It can be used to obtain numerical estimates for the S-matrix amplitude by regarding $s(\omega_1,\ldots,\omega_N)$ as a global prefactor. In principle, the optical phase shifts could be obtained from the spectral phase and could thus be incorporated as well. Emission processes can be included in analogy to the method employed in the P model.

The resulting model expressions for the probabilities reproduce the particle spectra to good extent as well. In contrast to the P model, this model includes the ordinary terms and the self-interference terms. However, the latter cannot be accessed directly, as shall be discussed further below. Furthermore, with the models being based on rather different approaches, a comparison of the numerical estimates does not necessarily deliver relevant information.

4.3.2 Self-interferences

As introduced in Sec. 3.2.2, self-interferences are interferences between different combinations of the same total number of involved laser photons. Thus, they arise in channels with at least two photons. Following the S model, we will now regard the structure of the S-matrix amplitudes for processes with one or two photons stemming from a laser field with an unspecified shape.

Starting with the one-photon amplitude, the integration in Eq. (4.7) is carried out and yields

$$\mathcal{S}_1 = s(E_L)|\xi(E_L)|\,, \tag{4.9}$$

where $E_L = q_+^0 + q_-^0 - \omega_\gamma$ denotes the required energy from the laser photon.[3] Thus, the pair-production amplitude is proportional to the Fourier transform of $\xi(t)$ evaluated at the required energy.

Similarly, the two-photon amplitude following from Eq. (4.8) can be written as

$$\mathcal{S}_2 = \frac{1}{2}\int d\omega\, s(\omega, E_L - \omega)|\xi(\omega)|\,|\xi(E_L - \omega)| \tag{4.10}$$

where ω denotes the frequency of the first photon, while $E_L - \omega$ is the frequency of the second photon. For the following discussion, we note that the two-photon amplitude is of the form

$$\mathcal{S}_2 = \int d\omega\, g(\omega) \tag{4.11}$$

[3]If E_L depends on the laser frequency, the factor resulting from the derivative which occurs, when the δ function is evaluated, is absorbed into $s(E_L)$.

where $g(\omega)$ is a complex-valued function, which can be assumed to be continuous, at least piecewise. From now on, we drop the explicit dependence on the required energy E_L, which is regarded as a fixed external parameter.
The corresponding differential probability for the two-photon processes

$$\mathcal{P}_2 = |\mathcal{S}_2|^2 = \int \int d\omega d\omega' \, g(\omega) g^*(\omega') \tag{4.12}$$

can be understood as a two-dimensional integration. Here, contributions with $\omega = \omega'$ are the ordinary, interference-free, two-photon processes. Conversely, contributions with $\omega \neq \omega'$ are the two-photon self-interferences.
Mathematically speaking, the integration domain with $\omega = \omega'$ has a vanishing weight in the two-dimensional integration. Usually, this means that the corresponding contribution to the integral vanishes. In order to deliver a finite contribution, the integrand needed singularities like $\delta(\omega - \omega')$. But the latter is not compatible with the structure of Eq. (4.12), since both integrals are independent of each other. Hence, from this point of view, the full two-photon probability cannot be reduced to the ordinary processes. Instead, the self-interference terms give a sizable contribution.
This finding is further corroborated by the following picture. Temporarily regarding a multichromatic field, the two-photon amplitude Eq. (4.11) arises as a discrete sum $\mathcal{S}_2 = \sum_j g_j$. Therefore, the self-interference terms can be obtained from the discretized version of Eq. (4.12) as

$$\mathcal{P}_2^{\mathrm{SI}} = \sum_j g_j \left(\mathcal{S}_2 - g_j\right)^* . \tag{4.13}$$

If the field is composed of many modes, allowing us to assume that $\mathcal{S}_2 - g_j \approx \mathcal{S}_2$, we see that $\mathcal{P}_2^{\mathrm{SI}} \approx \mathcal{P}_2$. This assumption is particularly well fulfilled in the case of a continuous spectrum. As a final illustrative example, one may think of $g(\omega)$ being a Gaussian function. Thus, the integrand of the probability $\mathcal{P}_2$ [see Eq. (4.12)] is spherically symmetric, completely eliminating the special role of the main diagonal.
In conclusion, the self-interference terms are natural constituents of processes driven by a continuous spectrum. In contrast to the usual interferences between different photon-number channels, the self-interference terms are lacking a characteristic phase dependence which could be investigated in parameter scans. Instead, they silently contribute to the process probability. Moreover, when we regard the transition from a multichromatic field towards a continuous spectrum, the weight of the usual diagonal terms vanishes. In fact, at least when the spectral phase is virtually independent of the frequency, their role is assumed by the self-interference terms.
Finally we note that the P model follows a different approach, since the integrations are carried out at the level of the probability. There, the full probabilities are approximated by the combination of the diagonal terms and the phenomenological factor p_0.

4.3.3 Interferences in bichromatic fields of finite spectral width

Bichromatic fields arise as the superposition of two co-propagating monochromatic fields with different frequencies and amplitudes. When these fields are employed in scattering experiments, photons can be interchanged with both fields. In particular, interferences between different process channels can arise. The phase of these interferences can usually be controlled by the relative phase shift between the two monochromatic modes, leading to pronounced interference effects. In the following, we will briefly address the question

to which extent these interferences are affected by the finite spectral broadening which is unavoidable in the laser fields employed in actual experiments.
At first glance, one might suspect that interferences are suppressed. Regarding a given constellation of photons, each with a differently detuned energy, the interference criterion Eq. (3.7) cannot be fulfilled. However, employing our approach presented in Sec. 3.2, we will first sort the photon combinations according to their total energy. This way, we can expect to find suitable interference partners. Following this path, we will explore the situation in more detail, in particular with regard to the question if the characteristic dependence on the optical phases persist.
To this end, we introduce a bichromatic field with a basic frequency ω_B and a higher harmonic ω_H. The spectral shape including the broadening is described by functions $\xi_B(\omega)$ and $\xi_H(\omega)$, which give rise to the full field in the form

$$\xi(\omega) = \xi_B(\omega) + \xi_H(\omega)\,. \tag{4.14}$$

This decomposition is naturally repeated in the process amplitudes as introduced in the previous section. Starting from Eq. (4.9), the one-photon amplitude can be written as

$$\mathcal{S}_1 = \mathcal{S}_1^B + \mathcal{S}_1^H \tag{4.15}$$

where the superscripts denote the spectral origin of the involved photon. Analogously, the two-photon amplitude introduced in Eq. (4.10) can be brought into the form

$$\mathcal{S}_2 = \mathcal{S}_2^{BB} + \mathcal{S}_2^{BH} + \mathcal{S}_2^{HH}\,. \tag{4.16}$$

where for example the first term is of the form

$$\mathcal{S}_2^{BB} = \frac{1}{2}\int d\omega\, s(\omega, E_L - \omega)|\xi_B(\omega)||\xi_B(E_L - \omega)|\,. \tag{4.17}$$

The following discussion requires a closer look at the energetic situation. We assume the spectral broadening to be much smaller than the difference between the modes ω_B and ω_H. Accordingly, if a process requires a certain energy E_L, only one of the respective terms in Eqs. (4.15) and (4.16) will deliver the relevant contribution. As an example, let us regard the case where $\omega_H = 2\omega_B$. If the required energy E_L is close to ω_H, it can be provided by either two photons from the basic mode ω_B, or by one photon from the higher harmonic ω_H. The relevant terms are $\mathcal{S}_1 \approx \mathcal{S}_1^H$ and $\mathcal{S}_2 \approx \mathcal{S}_2^{BB}$. The resulting probability thus reads

$$\mathcal{P} \approx |\mathcal{S}_1^H + \mathcal{S}_2^{BB}|^2 = |\mathcal{S}_1^H|^2 + 2\Re\left(\mathcal{S}_1^H \mathcal{S}_2^{*BB}\right) + |\mathcal{S}_2^{BB}|^2\,. \tag{4.18}$$

The structure of the probability is similar to the well-known case of a bichromatic field, where the relative phase shift between the two modes induces a distinct phase term. Here, with $\mathcal{S}_2^{*BB}$ being composed of the superposition of many contributions, the question arises if these distinct phase effects are preserved. This question can be answered by following our discussion in Sec. 4.1: If the spectral phase of the laser field is practically constant across the spectral range around ω_B, or if it depends only linearly on the frequency, all contributions to $\mathcal{S}_2^{*BB}$ enter with a common photon phase. As a consequence, we can expect to obtain a similar dependence on the relative phase shift between (the spectral ranges around) ω_H and ω_B as in the original bichromatic case. The self-interference terms inherent to $|\mathcal{S}_2^{BB}|^2$ are independent of this phase shift.
In conclusion, we expect pronounced interference effects to persist despite a certain degree of spectral broadening. We have found a quantitative criterion which aims at the spectral properties, in particular the spectral phase, of the radiation source. This criterion has to be compared with the actual experimental situation.

4.4 Conclusion

In this chapter, we have seen that the pair-production process driven by a short pulse of moderate intensity is subject to pronounced interference effects between different production channels. These channels arise due to the broad spectrum of the pulse, which allows to deliver the required photon energy by different combinations of photons. When channels of different total numbers of photons interfere, the interference phases obtain a characteristic dependence on the CEP of the laser pulse, which can be detected in the energy spectra of the produced particles. These effects reflect the analogy between the CEP of a continuous pulse and the relative phase shift in bichromatic fields.
Further effects caused by the CEP comprise the probability of the multiphoton channels, and in particular the symmetry properties of the laser field. The latter effects will be discussed in Chap. 6.
In addition, we have employed our analytical approach in order to explore the general properties of interference processes driven by short pulses. We have found that in addition to the above-mentioned interferences, also interferences between combinations of the same total number of photons (self-interferences) arise. From a mathematical perspective, these terms provide important contributions to the full probability. However, at least for the pair-production process, they are lacking a characteristic dependence on the CEP (or on any other accessible parameter), and can therefore hardly be detected. Regarding the experimental observation of general multiphoton interferences, we have investigated the question if interference effects persist despite the spectral broadening inherent to experimental radiation sources. We have found that the spectral broadening does not necessarily suppress interferences.

5 Spin Effects

Being a truly non-classical entity, the spin is responsible for the fundamental properties of matter. Regarding for example the periodic table, the chemical and the physical properties of the elements are, at their core, determined by the Pauli exclusion principle, which applies to the occupation of the electronic shells as well as to the formation of the nuclei. Regarding charged (fermionic) elementary particles such as the electron, the spin induces a magnetic moment, which affects the properties of individual atoms and molecules, for example via spin-orbit coupling, as well as collective phenomena such as ferromagnetism. In this chapter, the role of the particles' spin in the pair-production process shall be investigated. To this end, a comparison will be established between the probabilities obtained starting from the Klein-Gordon (KG) equation and from the full Dirac equation. Characteristic differences and similarities arise, which shall be examined. The analysis is supported by the P Model and by the insights gained in the previous chapters. The basic understanding emerges from a consideration of the pair-production rates obtained for multiphoton processes in monochromatic fields. In the course of this chapter, the influence of the pulse duration is studied in detail.
The two inequivalent spin configurations for Dirac particles are distinguished by means of the label $s = |s_+ + s_-|$, which gives the absolute value of the sum of the spin quantum numbers in $\mathscr{P}_{s_+,s_-}$, and has the values $s = 0$ and $s = 1$. For Dirac particles, the multiphoton pair-production rates have been derived in the course of this work. For scalar particles, the main derivation was presented in [Jan13].[1] We present results which were originally published in [JKKM16] as well as additional results and analysis.

5.1 Multiphoton processes in monochromatic fields

We begin our investigation of spin effects by regarding multiphoton processes in monochromatic fields. In combination with the P-Model approach, the resulting properties and insights can be transferred to the case of a short laser pulse. As a major advantage, the corresponding pair-creation rates can be expressed in closed analytical form for several limiting cases and thus allow direct access to the properties of the underlying pair-creation process. These rates are obtained from an S-matrix approach employing the Volkov states. Hence, the action of the laser field on the particles is fully taken into account. For small field strengths, the analytical expressions for the rates can be Taylor expanded in the field-strength parameter ξ. The leading order term scales as ξ^{2N} for a N-photon process and should coincide with a corresponding calculation within perturbation theory, where the laser field is treated as a quantized radiation field. This can explicitly be verified for the one-photon process; and for a more general treatment, we refer to [BV80, BV81].
A further simplification can be achieved by evaluating the expressions in the center-of-mass (c.m.) frame, where the frequencies of the gamma quantum and of the laser field can both be described by the particles' c.m. velocity β.[2] We begin our discussion by regarding the

[1] A related derivation for the production probability of scalar particles due to the absorption of two energetic photons can be found in [AB65], though with some minor misprints.

[2] For a N-photon process, the energy balance in the c.m. frame reads $N\omega_c' = \omega_\gamma' = E_{p_+'} = E_{p_-'} = m/\sqrt{1-\beta^2}$.

behavior close to the energetic threshold, where the particles are produced with vanishing velocities $\beta = 0$. In the following, we present the rates $\mathscr{R}_N$ for the N-photon process in terms of a common prefactor $\alpha m \xi^{2N}$.
For the usual Breit-Wheeler process initiated by the head-on collision of two linearly polarized photons with polarization vectors $\mathbf{e}_1$ and $\mathbf{e}_2$, we obtain the following rates for the production of low-energy KG and Dirac particles, respectively:

$$\mathscr{R}^{\mathrm{KG}}_{1,\mathrm{pol}} = \frac{1}{4}\beta(\mathbf{e}_1 \cdot \mathbf{e}_2)^2 + \mathcal{O}(\beta^3)\,, \tag{5.1}$$

$$\mathscr{R}^{\mathrm{DI}}_{1,\mathrm{pol}} = \frac{1}{2}\beta(\mathbf{e}_1 \times \mathbf{e}_2)^2 + \mathcal{O}(\beta^3)\,. \tag{5.2}$$

For Dirac particles, the leading-order term stems from the contribution with $s = 0$. Despite the similar β scaling, the comparison between KG and Dirac reveals a striking difference concerning the dependence on the relative orientation of the photon polarization vectors: For parallel alignment, the production rate for scalar particles reaches its maximum, while production of Dirac particles is completely suppressed. Conversely, in the orthogonal case, the situation is reversed.
In order to enhance the similarity between Dirac and KG, we will regard a beam of unpolarized gamma quanta (by taking the average of the polarization direction of the gamma quantum) in the following. For the one-photon process, we obtain

$$\mathscr{R}^{\mathrm{KG}}_{1} = \frac{1}{8}\beta - \frac{11}{48}\beta^3 + \mathcal{O}(\beta^5)\,, \tag{5.3}$$

$$\mathscr{R}^{(0)}_{1} = \frac{1}{4}\beta - \frac{1}{8}\beta^3 + \mathcal{O}(\beta^5)\,, \tag{5.4}$$

$$\mathscr{R}^{(1)}_{1} = \frac{1}{2}\beta^3 - \frac{7}{20}\beta^5 + \mathcal{O}(\beta^7)\,. \tag{5.5}$$

The full Dirac rate is obtained as the sum $\mathscr{R}^{\mathrm{DI}}_1 = \mathscr{R}^{(0)}_1 + \mathscr{R}^{(1)}_1$, where the superscript s distinguishes the spin configurations. The rate for KG particles and the contribution from $s = 0$ both grow linearly in β, while the contribution from $s = 1$ is suppressed by an additional factor of β^2. Comparing the threshold behavior of the different rates, a rather simple picture emerges: The rate for Dirac particles is dominated by the contribution from $s = 0$ and twice as large as the production rate of (intrinsically spinless) KG pairs. In order to establish an intuitive approach, one may say that Dirac pairs are produced with vanishing total spin. Furthermore, the rate ratio $\zeta_1 = \mathscr{R}^{\mathrm{DI}}_1/\mathscr{R}^{\mathrm{KG}}_1 = 2$ coincides with the number of spin configurations which are included in the term with $s = 0$. In the following, we shall use this ratio as a measure for the spin sensitivity of the process.
This simple picture has to be treated with care, since it only holds close to threshold. For higher energies, the contribution from $s = 1$ becomes sizable, and, furthermore, also the rate ratio between the contribution from $s = 0$ and KG exceeds the factor 2.
A further complication emerges when we increase the number of absorbed laser photons, which affects the threshold behavior significantly. For the process involving two laser photons, we find

$$\mathscr{R}^{\mathrm{KG}}_{2} = \frac{13}{48}\beta^3 - \frac{133}{160}\beta^5 + \mathcal{O}(\beta^7)\,, \tag{5.6}$$

$$\mathscr{R}^{(0)}_{2} = \frac{1}{3}\beta^3 - \frac{77}{160}\beta^5 + \mathcal{O}(\beta^7)\,, \tag{5.7}$$

$$\mathscr{R}^{(1)}_{2} = \frac{1}{8}\beta - \frac{31}{48}\beta^3 + \mathcal{O}(\beta^5)\,. \tag{5.8}$$

Here, the production rate of Dirac particles is dominated by the contribution from $s = 1$. In comparison, the rate for KG particles is strongly suppressed with a relative factor of β^2. However, as before, the KG rate resembles the contribution from $s = 0$. Their numerical ratio is 16/13, which clearly differs from the factor 2 found for the one-photon process.
For the three-photon process, the threshold behavior resembles the one-photon process:

$$\mathscr{R}_3^{\mathrm{KG}} = \frac{9}{512}\beta - \frac{249}{1024}\beta^3 + \mathcal{O}(\beta^5)\,, \tag{5.9}$$

$$\mathscr{R}_3^{(0)} = \frac{9}{256}\beta - \frac{177}{512}\beta^3 + \mathcal{O}(\beta^5)\,, \tag{5.10}$$

$$\mathscr{R}_3^{(1)} = \frac{93}{128}\beta^3 - \frac{1155}{256}\beta^5 + \mathcal{O}(\beta^7)\,. \tag{5.11}$$

Again, the dominant contribution to the full Dirac rate stems from the term with $s = 0$. As for the one-photon process, the rate ratio is $\mathscr{R}_3^{\mathrm{DI}}/\mathscr{R}_3^{\mathrm{KG}} = 2$ for low-energy particles.
Further increasing the number of absorbed laser photons up to $N = 10$ has revealed that the described behavior continues to alternate between even and odd photon numbers. For even numbers N, the ratio $\mathscr{R}_N^{(0)}/\mathscr{R}_N^{\mathrm{KG}}$ between the production rates of low-energy particles can be described by the formula $\frac{4N^2}{2N^2+2N+1}$, which approaches the factor 2 in the limit of large photon numbers.
Several aspects of the described behavior can be understood by regarding the total-angular-momentum balance of the process.[3] Each participating photon carries one unit of angular momentum along the beam axis. The total incoming angular momentum thus depends on the number of absorbed photons and has to be compensated by the particles. When the particles are produced with small momenta, such that their total angular momentum is completely determined by their spin, this constraint imposes a selection rule which is particularly sensitive to the parity of the number of photons and to the spin configuration of the pair. For example in the one-photon process, the total incoming angular momentum is -2, 0, or 2. This gives an explanation for the suppression of the contribution from $s = 1$ close to the threshold, while the "spinless" configurations remain unaffected. Conversely, for the two-photon process, the total incoming angular momentum is an odd number. Accordingly, the contribution with $s = 1$ dominates the Dirac rate, while the "spinless" configurations are suppressed this time. For higher particle momenta, the suppression is generally mitigated since the incoming angular momentum may also be transferred to the orbital angular momentum of the pair. In order to obtain a significant orbital-angular-momentum component along the beam axis, the particles are preferably emitted in transverse directions.[4] In contrast, when the incoming angular momentum can be compensated by the particles' spin, their emission pattern remains unaffected by this consideration. Signatures of this selection rule are visible in the angular distributions and shall be presented below.
As a preparation for the discussion of spin effects in a laser pulse, we will now investigate the rate ratio ζ_N for $N = 1, 2, 3$ in the whole interval of β. In addition to the dependence on the parity of the number of photons, the spin sensitivity reveals an increasingly rich dependence on β as N grows. As the blue curve in Fig. 5.1 shows, the one-photon ζ_1 essentially grows with β. Conversely, for the two-photon process (see green curve), ζ_2 diverges with $1/\beta^2$ at the threshold and falls into a minimum at $\beta \sim 0.5$. For these

[3] In [IKS05], the angular-momentum balance was used in a similar context.

[4] We determine the pair-creation rates (or probabilities) in a plane-wave basis for the particle states in which the orbital angular momentum can hardly be accessed. Nevertheless, the process produces real particles with well-defined physical properties.

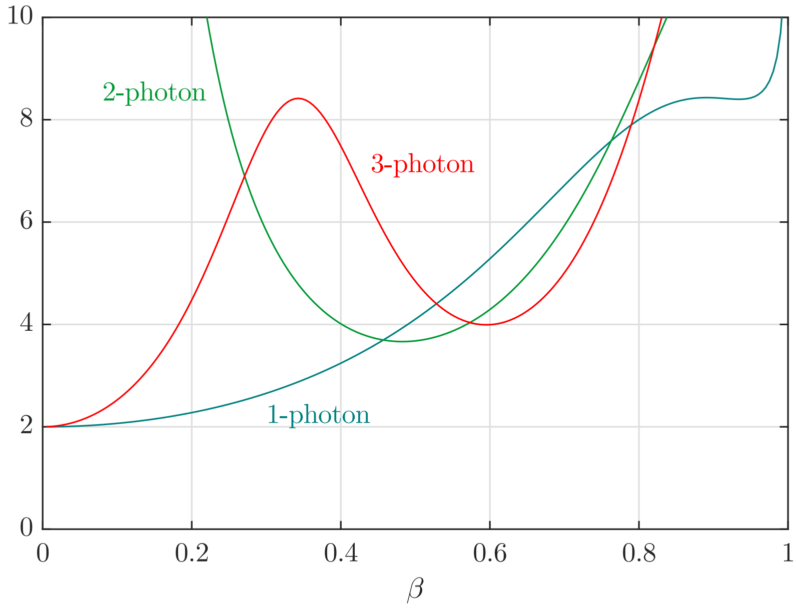

Figure 5.1: Ratio between the rates for Dirac and KG for different numbers of absorbed photons as a function of the velocity β of the particles. Originally published in [JKKM16].

momenta, the spin sensitivity is actually smaller than for the one-photon process. Finally the three-photon ζ_3 possesses a pronounced maximum and minimum (red curve). For all processes under investigation, we find $\zeta_N \geq 2$. Thus, the KG rate gives a lower limit for the full Dirac rate. Furthermore, despite the rich dependence on β, the rate ratio amounts to $\zeta_N \sim 4$ for intermediate momenta. In the limit of ultra-relativistic particles, the production rates generally vanish again. As can also be seen in Fig. 5.1, the asymptotic behavior reveals strong spin sensitivities. Nevertheless, these processes play only a minor role for the full pair-production probability obtained in a pulse.

In conclusion, the spin effects strongly depend on the kinematic conditions and can partially be understood in terms of the angular-momentum balance of the process. Strong spin effects arise close to threshold if the number of laser photons is even, and for ultrarelativistic particles. In contrast, moderate particle energies are generally accompanied with intermediate spin sensitivity.

5.2 Spin effects in short pulses

As a next step, we will investigate the influence of the pulse shape on the spin effects. To this end, we will compare pair-production processes in laser fields with a common central frequency ω_c but different spectral compositions. Beginning with a monochromatic field, we will proceed to pulses with various numbers of cycles N_{osc} and carrier-envelope phases χ, see Eq. (2.11). To begin with, the latter will be chosen as $\chi = 0$. As before, we will keep $\xi_{\max}$ constant. Furthermore, guided by our findings for monochromatic fields, we will regard kinematically different scenarios.

In particular for a long pulse or a monochromatic field, the kinematic situation is determined by the ratio $\omega_c\omega_\gamma/m_*^2$, which is invariant under Lorentz transformations along the beam axis. Here, m_* denotes the laser-dressed mass. Assuming a monochromatic field of linear polarization with amplitude parameter ξ, the dressed mass reads $m_* = m\sqrt{1+\xi^2/2}$.

The minimum number of required laser photons is given by the smallest integer which exceeds $m_*^2/(\omega_c\omega_\gamma)$. In the regime with $\xi \lesssim 1$, the production channel with smallest photon number usually gives the dominant contribution to the full process due to the perturbative intensity scaling. For a process involving N laser photons of frequency ω_c, the particles' center-of-mass energy reads $E_{p'} = \sqrt{N\omega_c\omega_\gamma}$. In order to establish a connection to our previous findings, we introduce the usual relativistic parameters β and $\gamma = (1-\beta^2)^{-1/2}$ and account for the laser dressing by means of $E_{p'} = \gamma m_*$, which leads to $\beta = \sqrt{1 - \frac{m_*^2}{N\omega_c\omega_\gamma}}$. The calculations are carried out in the c.m. frame of the leading-order process in the monochromatic field. We note that the ratios ζ_N from the previous section are invariant under Lorentz transformations along the beam axis.

5.2.1 Above the one-photon threshold

In this first scenario, we begin with a weak monochromatic laser field with $\xi = 0.02$ and photon frequencies $\omega_c = \omega_\gamma = 1.006m$. Hence, the absorption of one laser photon is sufficient to create a pair just above the threshold with $\beta \approx 0.11$. In accordance with Eqs. (5.3)-(5.5), the comparison of the particle creation rates yields a Dirac-to-KG ratio of $\zeta \approx 2.1$. In contrast, when an ultrashort pulse with $N_{\mathrm{osc}} = 2$ of the same central frequency is employed, we obtain a significantly larger ratio $\zeta \approx 3.5$. This is, the spin sensitivity is clearly enhanced in the pulse as compared to the monochromatic field.

The origin of this enhancement can be traced back to the broad spectrum of the short pulse, in particular to the availability of high-energy photons. While the monochromatic laser field produces pairs with fixed c.m. energy $E_{p'} \approx 1.006m$, the pulse produces pairs in a broad energy range. As can be seen from the corresponding momentum spectrum in Fig. 5.2, the positrons are typically produced with significantly higher momenta than in the monochromatic field, where $p_+ \approx 0.11m$. In the spirit of the P-Model, the momentum spectrum is determined by the interplay between the spectral energy density of the pulse and the energy dependence of the production rates [see. Eqs. (5.3)-(5.5)]. While the energy density generally falls off for higher photon energies, the production rates of the one-photon process essentially grows with β. As a result, the largest contributions stem from particles with an average c.m. velocity $\beta \approx 0.45$.[5] As we have seen in the previous section, these processes are also subject to stronger spin effects with $\zeta_1 \approx 3.6$ [see. Fig. 5.1] than the production of low-energy pairs.

Despite the strong spin sensitivity of the fully integrated probabilities, several similarities between Dirac and KG can be found in the differential probabilities. The momentum spectra as depicted in Fig. 5.2 exhibit qualitative resemblance for KG and Dirac particles. The dominant contribution to the latter stems from the term with $s = 0$, while the contribution from $s = 1$ shows the typical suppression at the threshold which is imposed by the angular momentum balance. The shapes of the high-energy tails are mostly determined by the fall-off of the spectral energy density and thus similar for all spin configurations.

As a next step, we regard the fully differential angular distributions for fixed positron momenta $p_+ = 0.15m$ in Fig. 5.3. The angular distribution of the contribution with $s = 0$ is almost homogenous yet moderately enhanced in the laser backward direction. In contrast, the angular distribution of the contribution with $s = 1$ is peaked around the polarization axis of the laser, while emission along the laser axis is suppressed. Comparing the two

[5] The typical average c.m. velocity can most easily be obtained as follows: Starting from the energy spectrum, the typical positron momentum p_+ can be deduced. The corresponding average absorbed laser energy E_L then replaces the product $N\omega_c$ in the above equations for β, where also the pulse-dressed mass enters.

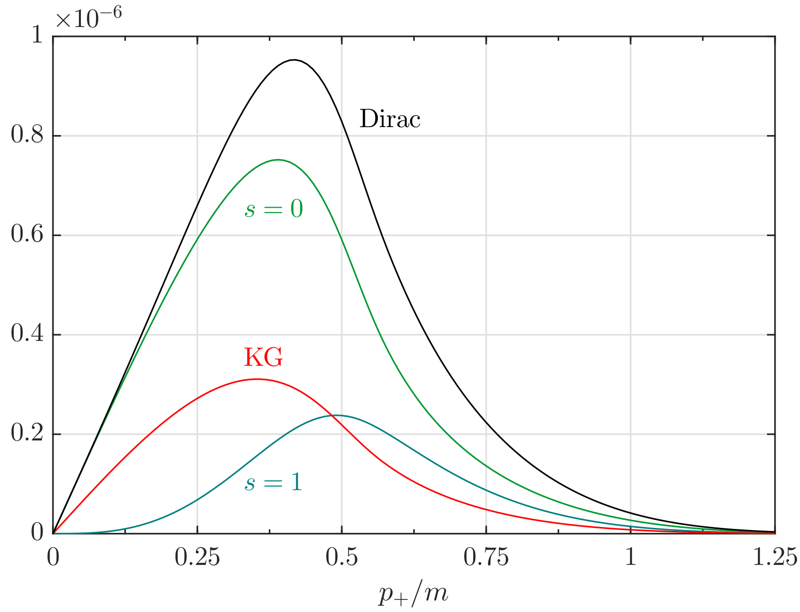

Figure 5.2: Angularly integrated probabilities $\frac{d\mathscr{P}}{dE_{p_+}}$ in units of $1/m$ as a function of p_+/m for $\omega_c = \omega_\gamma = 1.006m$, $N_{\text{osc}} = 2$, and $\xi_{\text{max}} = 0.02$. Originally published in [JKKM16].

distributions, the impact of the conservation of angular momentum (as discussed in the previous section) becomes obvious. The total Dirac distribution is essentially determined by the contribution with $s = 0$, while the smaller contribution with $s = 1$ appears as an azimuthal modulation. In comparison, the KG distribution appears qualitatively similar, but, here, the modulations are offset by $\pi/2$ as compared to the Dirac case. Employing the framework of quantum kinetic theory, a similar out-of-phase behavior is found in the momentum spectra of the particles being produced in a purely time-dependent field [HADG09, DD10, DD11].

Until now, we have compared the two extreme cases of a monochromatic laser field and of an ultrashort pulses with just two cycles. Increasing the number of cycles with $N_{\text{osc}} = 2, 4, 6$, and 9, the spin sensitivities were found to diminish with $\zeta = 3.5, 2.9, 2.6$, and 2.4. As N_{osc} grows, the spectral width of the pulse becomes narrower and the availability of high-energy photons is reduced. Accordingly, the pairs are produced within a narrower energy range and with smaller typical energy. This behavior will be depicted in the following section. Thus, the spin effects are reduced and the situation becomes increasingly similar to the case of a monochromatic field, where $\zeta \approx 2.1$.

5.2.2 Just below the one-photon threshold

In the next scenario, the frequencies $\omega_\gamma = 1.4m$ and $\omega_c = 0.7m$ are chosen just below the threshold of the one-photon process. With $\xi = 0.2$, the monochromatic field produces pairs by means of a two-photon process with $\beta \approx 0.69$ and strong spin effects as indicated by $\zeta \approx 5.8$. In contrast, the comparison of the pair-production probabilities in a two-cycle pulse yields $\zeta \approx 3.4$. Hence, for these parameters, the spin effects in the pulse are clearly reduced as compared to the monochromatic case.

The current scenario nicely illustrates that the sharp threshold behavior inherent to the pair-production process in a monochromatic field is smeared out when a pulse is regarded

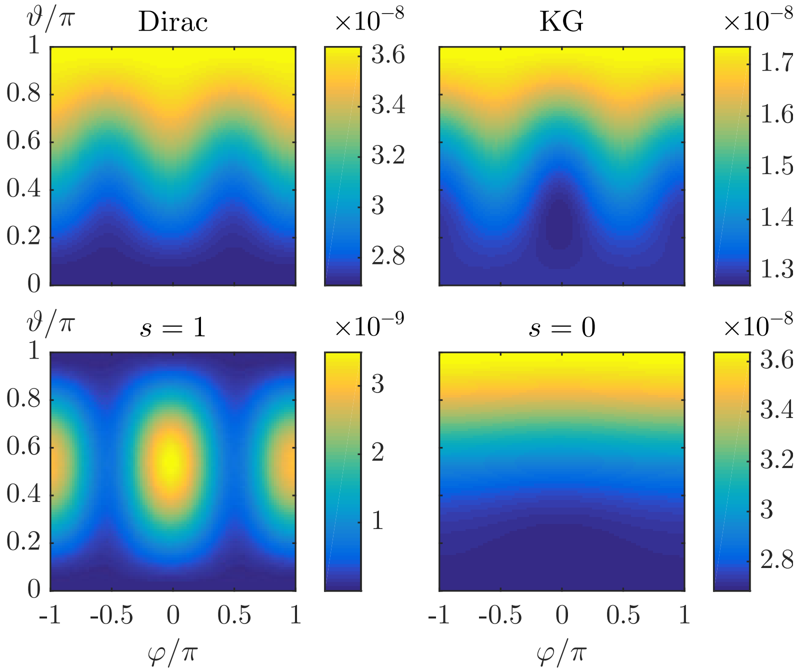

Figure 5.3: Fully differential probability $\frac{d^3\mathscr{P}}{dE_{p_+}d^2\Omega_{p_+}}$ in units of $1/m$ for $p_+ = 0.15m$, $\omega_c = \omega_\gamma = 1.006m$, $N_{\text{osc}} = 2$, and $\xi_{\max} = 0.02$. The angles ϑ and φ describe the positron emission direction and are measured with respect to the laser propagation and polarization directions, respectively. Originally published in [JKKM16].

instead. While the monochromatic field can only produce pairs via absorption of two or more laser photons, the high-energy part of the pulse spectrum facilitates pair production by one-photon processes. In particular, since the central frequency is chosen just slightly below the threshold, the spectral density at the required energy can still be significant, at least in a certain interval up to moderate particle energies. The perturbative intensity scaling additionally favors channels with smaller photon numbers. Accordingly, the full pair-production probability in the pulse is mostly determined by low-energy pairs created by one-photon processes, with average c.m. velocities $\beta \approx 0.45$ [see the momentum spectrum in Fig. 5.4]. These processes are accompanied with smaller spin sensitivity than the high-energy two-photon process driven in the monochromatic field and thus reduce the overall spin effects.

The described dominance of the production channel with lower photon number is referred to as subthreshold enhancement [TTKH12] and is induced by the intensity dependence of the pair-production rates. From the above line of argument, one may expect the reduced spin sensitivity to be a general accompanying feature if the dominant channel is driven by an odd number of laser photons.

As before, the momentum spectra for KG and Dirac are similar in shape, with the latter being determined by the contribution with $s = 0$. The small plateaus at $p_+ \approx m$ are caused by the two-photon process which eventually becomes dominant for higher energies, when the spectral density falls off. In particular, positrons with $p_+ \approx m$ require the energy $E_L \approx 1.4m$ to be absorbed from the pulse. The pulse spectrum, however, has its first zero at this energy, such that this process necessarily requires the absorption of two laser photons, just as in the monochromatic case.

When the pulse length is increased, the spin sensitivity in the present scenario exhibits

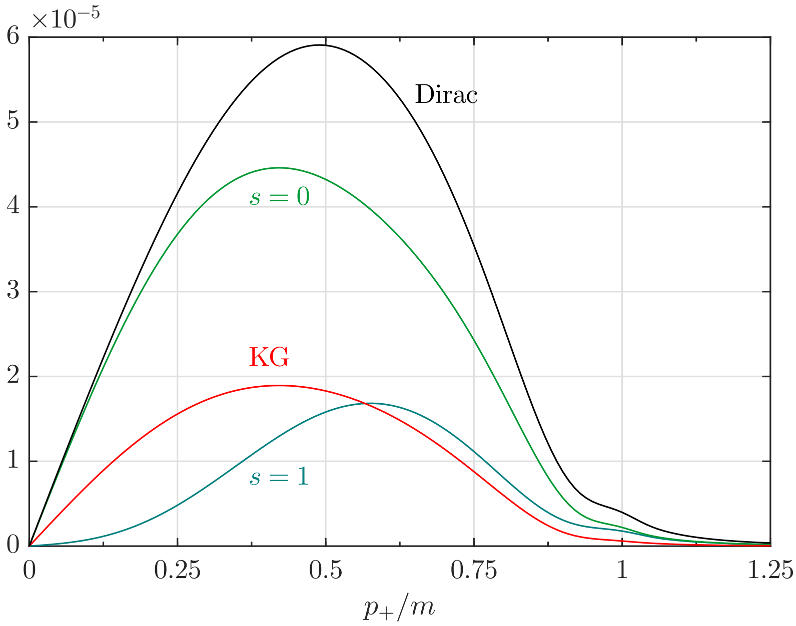

Figure 5.4: Same as Fig. 5.2 but for $\omega_\gamma = 1.4m$, $\omega_c = 0.7m$, and $\xi_{\max} = 0.2$. Originally published in [JKKM16].

a nonmonotonous behavior: First, for $N_{\text{osc}} = 2, 4, 6$, and 9, we find $\zeta = 3.4, 2.9, 2.7$, and 2.7. Thus, although the pulse spectrum becomes narrower, the difference with the monochromatic case is increased. Conversely, for $N_{\text{osc}} = 12, 15$, and 20, we obtain $\zeta = 2.7, 2.9$, and 3.3. Hence, the spin sensitivity eventually grows again and approaches the monochromatic case, where $\zeta \approx 5.8$. In the following, we shall investigate the influence of the pulse length in more detail. As before, the behavior can be understood by combining the P Model, which is based on the pulse spectrum, and the spin effects obtained in monochromatic fields.

In order to apply the P Model, the required photon energy E_L has to be determined. It depends on the positron energy as well as on its emission direction. For typical (absolute values of the) positron momenta, the relevant interval of energies E_L is depicted in the upper panels of Fig. 5.5 for two different pulses with $N_{\text{osc}} = 2$ (left) and $N_{\text{osc}} = 9$ (right). The extent of this interval, as indicated by the red and green curves in Fig. 5.5, is determined by the kinematics which are governed by the laser-dressed energy-momentum balance. For the current parameters, especially due to the moderate value of $\xi_{\max} = 0.2$, increasing N_{osc} only barely changes the interval. While the upper limit grows with p_+, the smallest overall required energy arises for $p_+ \approx 0.34m$. Production of positrons with $p_+ \approx 0.98m$ happens in a c.m. frame, such that the corresponding photon energy does not depend on the emission direction.

In contrast, strong effects due to the pulse length are present in the actual distributions of absorbed energies for fixed positron energies. Their shape is illustrated in Fig. 5.5 by means of the mean value and of the standard deviation obtained for the production of Dirac particles.[6] Increasing the pulse length, the interval of typically absorbed energies becomes generally narrower.

This behavior follows directly from the spectrum of the pulse, which is also depicted in the

[6]The energy distribution is asymmetric, and therefore the standard deviation exceeds the distance between the mean value and the lower or upper interval boundary for some positron momenta.

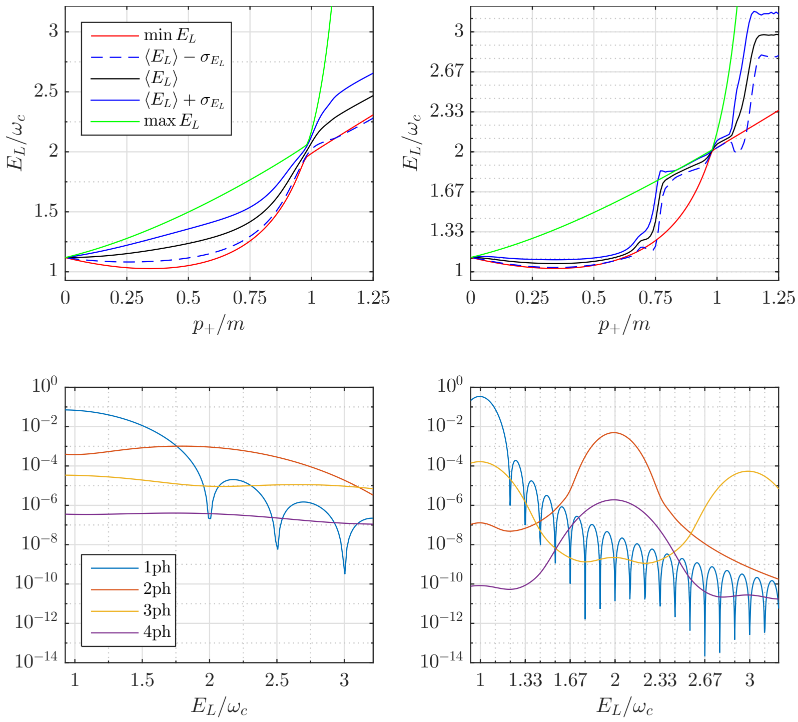

Figure 5.5: Analyzing the positron momentum spectra for $N_{\text{osc}} = 2$ (left) and $N_{\text{osc}} = 9$ (right): The required photon energy E_L depends on the positron energy and in general also on the emission direction. The plots in the upper row depict statistical information about E_L based on the pair-creation probability for Dirac particles. In particular, for a given positron momentum p_+, the relevant interval of photon energies can be read off. The second row depicts the P-Model estimates (in arb. units) for the probability of multiphoton processes as a function of the required energy E_L. Combining these information, for example the number of absorbed photons can be estimated. Comparing the plots for $N_{\text{osc}} = 2$ and $N_{\text{osc}} = 9$, the reduced spectral width of the pulse clearly restricts the available pair-production channels.

lower panels of Fig. 5.5. Here, the P-Model estimates (including emission processes) for the first photon-number channels are presented. Comparing $N_{\text{osc}} = 2$ (left) and $N_{\text{osc}} = 9$ (right), the effect of the reduced spectral width becomes clearly visible. The longer pulse supports processes in much narrower intervals centered around integer multiples of its central frequency.

Consequently, for positrons with $p_+ \lesssim 0.7m$ which require photon energies above the central frequency but sufficiently below the onset of the two-photon peak, increasing N_{osc} reduces the availability of high-energy photons and thus only processes requiring the smallest possible photon energies persist. This behavior is also reflected in the momentum spectra of Dirac particles, which are depicted in the upper panel of Fig. 5.6 for pulses with different numbers of cycles. As N_{osc} grows, a pronounced peak emerges around $p_+ \approx 0.34m$ due to the suppression of channels requiring increasingly unfavorable photon energies. The corresponding influence on the spin effects is illustrated by the ratio $\zeta(p_+)$ between the differential probabilities for Dirac and KG, respectively, in the lower panel of Fig. 5.6. Since the spin sensitivity of the one-photon process grows with E_L (at least close to the threshold), the above-described suppression leads to a minimum of $\zeta(p_+)$ at

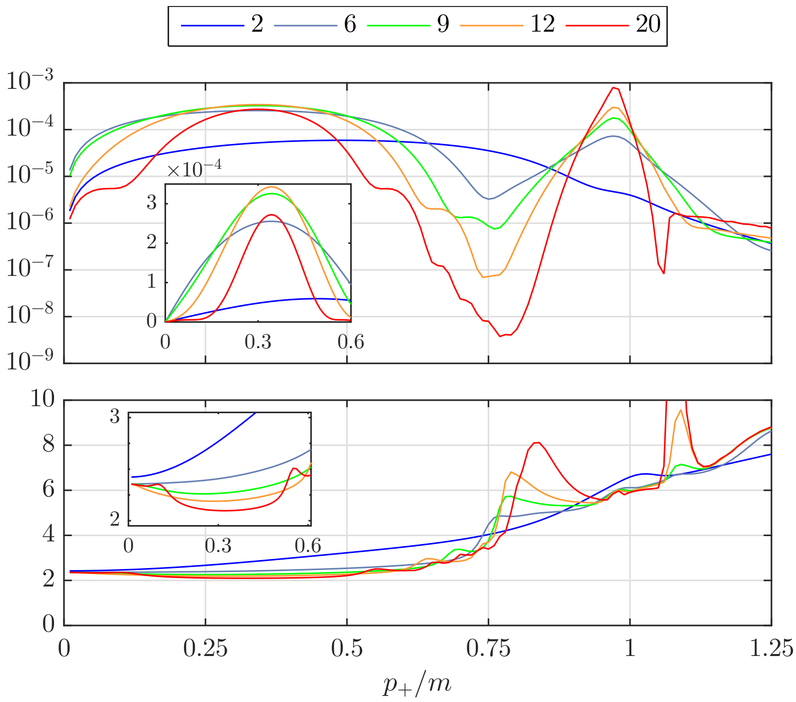

Figure 5.6: Positron momentum spectra for Dirac particles (upper panel) and spin effects as given by the ratio $\zeta(p_+)$ between the differential probabilities for Dirac and KG (lower panel) for various values of N_{osc} (as given in legend) and for $\omega_\gamma = 1.4m$, $\omega_c = 0.7m$, and $\xi_{\max} = 0.2$. Inlets show processes around $p_+ \approx 0.34$, where smallest overall spin sensitivity is found. Note different scales in the upper panel.

$p_+ \approx 0.34m$. Besides, this illustrates that the spin sensitivity is determined by the sum of the particle's momenta, which is encoded in E_L, rather than by the positron momentum alone. For short pulses with $N_{\text{osc}} < 9$, these processes with smallest E_L give the dominant contribution to the full pair-production probability and thus this development reduces the overall spin effects.

However, for longer pulses, the one-photon processes become increasingly unlikely and are eventually superseded by the high-energy two-photon processes, which are accompanied with significantly higher spin sensitivity. As depicted in the right column of Fig. 5.5, the required photon energy for positrons with momenta $p_+ \gtrsim 0.7m$ approaches the two-photon peak in the P Model. The upper right panel clearly shows the transitions between the one- and two-photon processes at $p_+ \approx 0.75m$, and between the two- and three-photon processes at $p_+ \approx 1.1m$. With Dirac and KG particles having different preferred angular directions, the transitions between the neighboring photon-number channels happen at slightly different positron energies and thereby enhance the corresponding spin effects visible in the lower panel of Fig. 5.6.

In particular positrons with $p_+ \approx 0.98m$ require photon energies of $2\omega_c$, which can most easily be provided by two photons of the central frequency, independent of the number of cycles. Thus, as N_{osc} grows, a corresponding maximum emerges in the positron energy spectra (see upper panel of Fig. 5.6). These processes increasingly resemble the process in a monochromatic field, while the first maximum at $p_+ \approx 0.34m$ deteriorates for $N_{\text{osc}} > 12$ (see inlet). Hence, the monochromatic situation is approached, and the threshold condition becomes more and more important. Note that for $p_+ \approx 0.98m$, the ratio between the

differential rates $\zeta(p_+) \approx 6$ can be read off the lower panel of Fig. 5.6 and almost coincides with the rate ratio obtained in the monochromatic field, see also Fig. 5.1.
In conclusion, we have seen how the pair-creation spectra react to the transition from an ultrashort pulse towards a significantly longer pulse in a rather complicated constellation of laser and radiation parameters. The P Model has proven helpful for the understanding of the positron momentum spectra obtained in pulses of various lengths. The accompanying spin effects could basically be understood from the behavior found in monochromatic fields. This finding provides further support for the underlying assumptions of the P Model.

5.2.3 Deeply below the one-photon threshold

As a final example where the pulse length has a particularly strong impact on the spin effects, we regard the frequencies $\omega_\gamma = 1.006m$ and $\omega_c = 0.503m$, which are deeply below the one-photon threshold. This scenario resembles the parameters of the above-threshold example, except that the laser frequency is halved. Hence, a weak monochromatic field with $\xi = 0.001$ can produce low-energy pairs with c.m. velocity $\beta \approx 0.11$ via absorption of two laser photons. As we have seen in Sec. 5.1, this process is quite sensitive to the particles' spin, with $\zeta \approx 39$. In contrast, the two-cycle pulse yields $\zeta \approx 2.9$ only, which means a reduction of one order of magnitude in the spin sensitivity.
As in the previous example, the pulse cannot provide photons of energy $2\omega_c$. Therefore, particles with $\beta \approx 0.11$ are produced via absorption of two laser photons. These processes occur with strong spin sensitivity, as in the monochromatic field. However, in addition, pairs with other energies are produced via absorption of one laser photon. Owing to the small value of ξ, these processes dominate the full pair-production probability, see Fig. 5.7 (a). The particles' typical average c.m. velocity $\beta \approx 0.32$ is greater than for the process in a monochromatic field, but – as can be anticipated from Fig. 5.1 – the corresponding spin effects are clearly smaller. Different to the above-threshold scenario, increasing the particle energy (and reducing the number of laser photons from two to one) thus reduces the spin effects in the present case. This is a consequence of the enormous spin sensitivity inherent to low-energy two-photon processes.
The particles' energy spectrum [see Fig. 5.7 (a)] contains several interesting details. Both the probabilities for KG and the contribution with $s = 0$ contain a pronounced dip at $\beta \approx 0.11$ which is caused by the spectral hole. In comparison, close to the threshold, the contribution with $s = 1$ is smaller by about two orders of magnitude, but it remains completely unaffected by the spectral hole. As we have seen before, these low-energy processes are suppressed when only one laser photon is absorbed. Here, the pulse spectrum also allows to deliver the required energy via two photons. Hence, the angular momentum balance can be fulfilled, but the intensity scaling limits the corresponding probability. In contrast to the one-photon processes, multiphoton processes are unaffected by the holes in the pulse spectrum.
The plateaus visible for higher positron momenta are further consequences of the spectral holes. As we have seen in the previous example (compare Fig. 5.5), for each positron momentum p_+, the spectral energy density is probed in a certain range of photon energies. In the current scenario, only the process with $\beta \approx 0.11$ happens in a c.m. frame, which explains the strength of the corresponding dip in the momentum spectrum. As p_+ grows, the range of photon energies is shifted to higher energies, becomes broader and comprises several spectral holes. Consequently, the effect of the spectral holes is soon washed out, but, in the current scenario, a plateau structure emerges instead: With the spectral energy density falling off for higher energies, the integrated probability drops significantly when

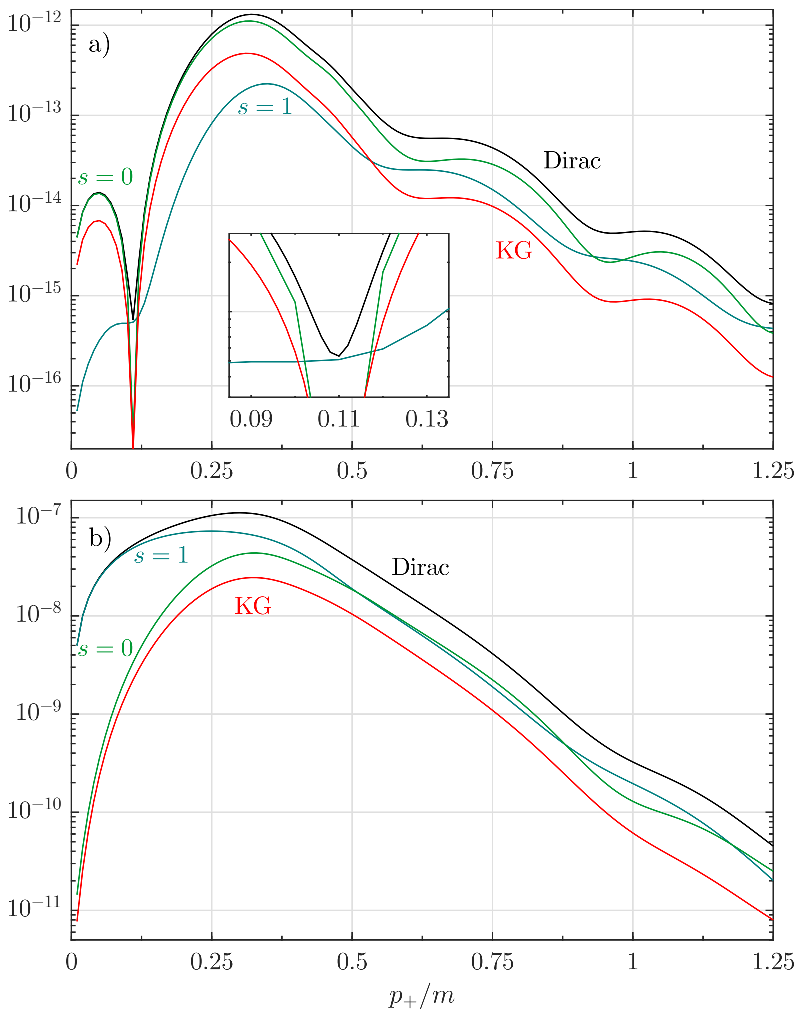

Figure 5.7: Same as Fig. 5.2 but for $\omega_\gamma = 1.006m$, $\omega_c = 0.503m$, and a) $\xi_{\max} = 0.001$, b) $\xi_{\max} = 0.1$. Originally published in [JKKM16].

the lower boundary of the interval passes one more local maximum in the pulse spectrum. Conversely, it remains almost constant when a hole is passed.

As a final step, we proceed to higher laser intensities with $\xi = 0.1$. The relative importance of multiphoton processes is thereby enhanced significantly, while the effects of the spectral holes disappear. Unlike in the previous scenarios, the P Model suggests that low-energy particles are predominantly produced via absorption of two laser photons, while higher total photon energies may also be delivered via three laser photons. Accordingly, the low-energy part of the momentum spectrum as depicted in Fig. 5.7 (b) is dominated by the contribution with $s = 1$. Close to the threshold, the "spinless" channels are clearly suppressed, since they are restricted to one- and, possibly, three-photon processes. As a consequence, the low-energy part of the particle spectrum reveals very strong spin effects, with a huge difference between Dirac and KG. However, as before, a higher degree of similarity is found in the behavior for intermediate and high positron momenta. Thus, the integrated probability exhibits only moderate spin sensitivity, with $\zeta \approx 4.6$. In contrast, the spin effects in the monochromatic field amount to $\zeta_2 \approx 66$ for the dominant two-photon process. In the present scenario, the laser dressing becomes noticeable and leads

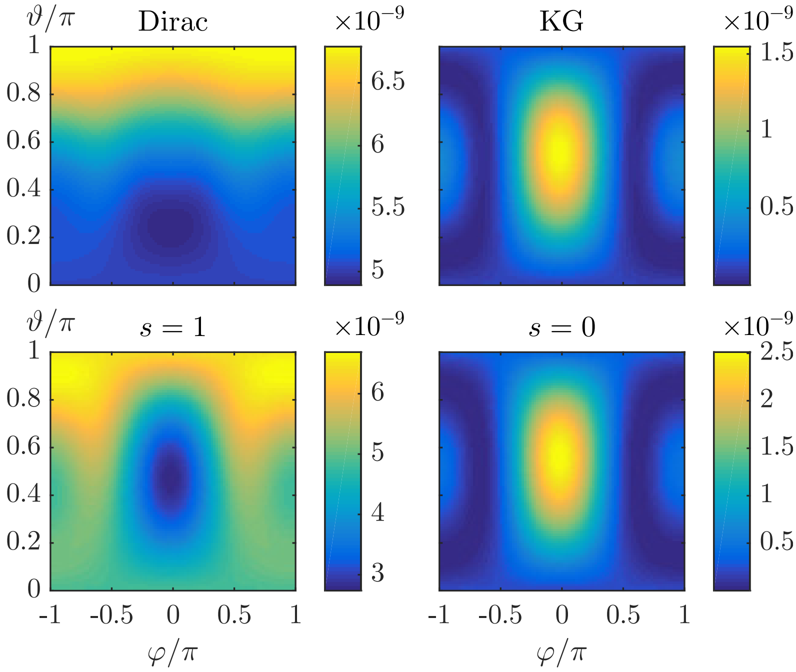

Figure 5.8: Same as Fig. 5.3 but for $\omega_\gamma = 1.006m$, $\omega_c = 0.503m$, and $\xi_{\max} = 0.1$. Originally published in [JKKM16].

to a reduction (as compared to the low-intensity case) of the particles' momenta ($\beta \approx 0.08$ as compared to $\beta \approx 0.11$), which, in turn, significantly increases the spin sensitivity. The contribution of the weaker three-photon process eventually reduces the overall spin sensitivity to $\zeta \approx 43$, which still exceeds the value found in the pulse by almost one order of magnitude. Thus, the strong impact of the pulse length on the spin effects persists also for these enhanced laser intensities.

Despite the striking differences between (total) Dirac and KG for small particle momenta, a close resemblance can be found between KG and the contribution with $s = 0$, even in the fully differential angular distributions. These are depicted for fixed positron momentum $p_+ = 0.15m$ in Fig. 5.8. At first glance, the emission patterns of the "spinless" channels look almost identical. The positron emission direction is centered around the polarization direction of the laser[7], with a numerical ratio less than two as expected for a low-energy two-photon process. Again, the restriction to transverse directions is a clear consequence of the angular momentum balance. The non-vanishing emission probabilities for longitudinal directions stem from processes with different photon numbers. In comparison, the emission pattern from $s = 1$ appears inverted, but with higher probabilities. As a result, the total angular distribution for Dirac particles is almost homogenous in transverse directions and thus entirely different to KG.

With the pair production being dominated by multiphoton processes, carrier-envelope-phase effects could be expected. Until now, we have kept the CEP $\chi = 0$ throughout. Next, we repeat the calculations for different values of the CEP while the maximum amplitude $\xi_{\max} = 0.1$ is fixed, as in the previous chapter. As a major difference to the previous chapter, the current investigation focuses on integrated probabilities. Since interference effects tend to disappear after integrating, we start our discussion with the ratio $\zeta(p_+)$,

[7]The asymmetry between the forward and backward direction along the polarization axis is related to the asymmetry of the vector potential, which can partially be controlled by the carrier-envelope phase.

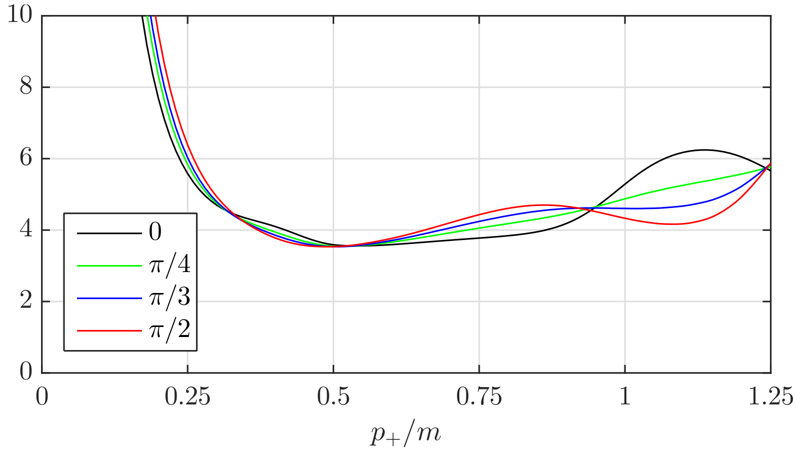

Figure 5.9: $\zeta(p_+)$ for various values of the CEP (as given in the legend) for $\omega_\gamma = 1.006m$, $\omega_c = 0.503m$, and $\xi_{\max} = 0.1$.

which does not include the last integration over the positron momenta. Despite being based on angle-integrated pair-production probabilities, this ratio exhibits clear CEP effects, which can be seen in Fig. 5.9 where $\zeta(p_+)$ is depicted for different values of χ. The CEP appears to modulate the rate ratio, with moderate enhancements and suppressions depending on the positron momentum. Particularly strong effects occur for high positron momenta with $p_+ \gtrsim m$, where also three-photon processes become relevant. Here, the rate ratio changes by several ten percent. In the other scenarios, the influence of the CEP on the spin sensitivities $\zeta(p_+)$ obtained in the pulse was found to be significantly smaller. There, the pairs were mostly produced via absorption of one laser photon. For these processes, $\zeta(p_+)$ is virtually invariant when χ changes. Finally, regarding the ratio ζ between the fully integrated probabilities, the CEP effects almost vanish and amount to $\lesssim 3\%$ only, for all examples.
As before, when the pulse length is increased, the reduced spectral width enhances the relative weight of processes induced by photons close to the central frequency. In the present scenario, this development amplifies the weight of the huge spin effects induced by the low-energy two-photon process leading to the pair with $\beta \approx 0.08$. Accordingly, the spin effects obtained in the pulse become much stronger than in the previous examples: For $N_{\text{osc}} = 2, 6, 12$, and 18, the rate ratios $\zeta = 4.6, 8.6, 14$, and 18 were found, approaching the monochromatic case, where $\zeta \approx 43$.

5.3 Summary and conclusion

To conclude this chapter, we have seen that the influence of the spin degree of freedom on the pair-production probabilities strongly depends on the kinematic situation under investigation. Predictions from Dirac and KG theory can be either quite similar, even with regard to the angular distributions of produced particles, or largely different. Hence, the spin plays a fundamental role for the process.
Beginning with multiphoton processes in monochromatic fields, the spin sensitivity, which was measured by the ratio ζ between the pair-production rates of Dirac and KG pairs, was found to depend on the energy of the produced particles and on the number of absorbed photons. The underlying behavior could basically be understood by regarding the conservation of the angular momentum which is carried by the incoming photons.

Accordingly, in particular close to the energetic threshold of the process, the spin effects depend on the parity of the total number of absorbed photons (i.e. the gamma quantum and the laser photons): Strong effects occur for odd total photon numbers, while $\zeta \sim 2$ for even total photon numbers. Conversely, production of particles with moderate energies is generally accompanied with intermediate spin sensitivity $\zeta \sim 4$, while ultrarelativistic particles are produced with strong spin effects with $\zeta \to \infty$. Especially in monochromatic fields (or long pulses) of moderate intensity ($\xi < 1$), these extreme cases can play a major role.

In contrast, increasing the spectral width (while keeping the central frequency constant) by reducing the pulse length generally enhances the weight of processes with moderate particle energies and thus induces intermediate spin sensitivity, which may be either larger or smaller than in the monochromatic case. This behavior was found despite the spectral holes present in our particular shape function, and may therefore be expected to arise in short pulses of other shapes, as well.

With regard to the theoretical investigation of the pair-production process, we note that despite the differences between the predictions from Dirac and KG theory, the general behavior reveals a high degree of similarity. This way, predictions from KG theory can be employed as an approximation to the full Dirac theory, which demands more involved computations. For example in the case of even higher laser intensities $\xi_{\text{max}} \gg 1$, when the process happens in the tunneling regime, an overall ratio $\zeta \approx 6$ was found in [VCM13]. Following the same philosophy, an S-matrix calculation for scalar particles was employed in [JM13] in order to investigate the enhancement of Schwinger-like pair production by adding a secondary high-frequency laser field.

We note that the present analysis provides information about the applicability of this approximation in the regime of moderate intensities $\xi_{\text{max}} \lesssim 1$. Furthermore, our approach based on the conservation of angular momentum supports an intuitive understanding of the role of spin.

Finally, our findings show that the pulse duration exhibits a profound influence on the SFBW process at moderate laser intensities. Following our multiphoton approach, this influence can be understood from the frequency spectrum of the pulse.

6 Two consecutive pulses

In this chapter, we regard the Strong-Field Breit-Wheeler process in the field of two consecutive laser pulses. We extend the laser field to two independent short pulses, which travel in the same direction but arrive with a variable time delay. These studies provide basic information about the pair-production process, in particular with regard to effects related to the shape of the driving laser field. In atomic physics, similar setups are employed to conduct experiments in a pump-probe manner, aiming at time-resolved information about the respective process.

6.1 The pair-creation probability

In the following, we will present the derivation of the pair-production probability for scalar particles due to the collision of a high-energy gamma quantum with two consecutive laser pulses. The latter can be described independently of each other, facilitating a derivation with a high degree of generality and flexibility. The field configuration is depicted in Fig. 6.1.

We will first introduce the combined vector field and the corresponding Gordon-Volkov states, and then derive the expressions for the S-matrix amplitude.

6.1.1 Scalar particles in the field of two consecutive pulses

The combined vector potential $\mathcal{A}^c$ reads

$$\mathcal{A}^c = \mathcal{A}_1 + \mathcal{A}_2 \tag{6.1}$$

where each pulse is of the form given by Eq. (2.10). In addition, we introduce phase-shift parameters δ_j which allow us to determine the timing of the pulses. The pulse parameters can be chosen almost independently, such that the vector potential of the individual pulses is introduced in the most general form as

$$\mathcal{A}_j^\mu = \mathcal{A}_j^\mu(\eta_j) = a_j f_j(\eta_j - \delta_j)\mathcal{X}_{[0,2\pi]}(\eta_j - \delta_j)\epsilon_j^\mu \tag{6.2}$$

with $\eta_j = k_j \cdot x$ for $j = 1, 2$. The notation employed in Eq. (6.2) treats the phase shifts δ_j as a part of the shape function, which simplifies the beginning of the following derivation. The pulses are restricted to the intervals

$$\eta_j \in [\delta_j, \delta_j + 2\pi]. \tag{6.3}$$

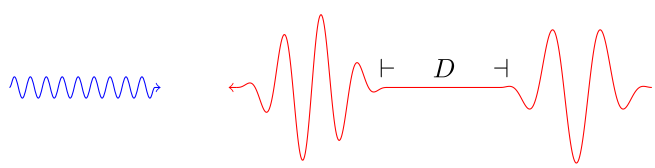

Figure 6.1: Schematic illustration of the field configuration: The gamma quantum collides with two consecutive laser pulses which are separated by a variable distance D. Originally published in [JM16b].

The pulses propagate in the same direction, and are polarized in transverse directions, i.e. $k_1 \cdot k_2 = 0$ and $\epsilon_i \cdot k_j = 0$ for $i, j \in \{1, 2\}$. In the following derivation, the phase shifts δ_j are understood to be chosen such that the pulses are strictly separated. Assuming pulse number one to arrive first with $\delta_1 = 0$, this condition implies $\frac{\delta_2}{\omega_2} > \frac{2\pi}{\omega_1}$.
Since the pulses have vanishing overlap, i.e. due to $\mathcal{A}_1 \cdot \mathcal{A}_2 = 0$, the Gordon-Volkov solutions of the corresponding Klein-Gordon equation can be written as

$$\Psi^c_{p_\pm} = \sqrt{\frac{m}{VE_{p_\pm}}} e^{i[\pm p_\pm \cdot x + \Lambda_1^\pm + \Lambda_2^\pm]} \tag{6.4}$$

where the contribution of the pulse $j = 1, 2$

$$\Lambda_j^\pm = \frac{1}{k_j \cdot p_\pm} \int_0^{\eta_j} \left[e p_\pm \cdot \mathcal{A}_j(\eta) \mp \frac{e^2}{2} \mathcal{A}_j^2(\eta) \right] d\eta \tag{6.5}$$

is of the same form as in the single-pulse case.

6.1.2 S-matrix amplitude

The S-matrix element for the pair-production process induced by the decay of the gamma quantum in the combined laser field $\mathcal{A}^c$ reads

$$\mathcal{S}^c_{p_+ p_-} = -i \int d^4x \, (\Psi^c_{p_-})^* \, \mathcal{H}^c_{\text{int}} \, \Psi^c_{p_+} \,, \tag{6.6}$$

with the interaction Hamiltonian

$$\mathcal{H}^c_{\text{int}} = \frac{-ie}{2m} \left(\mathcal{A}_\gamma \cdot \overrightarrow{\partial} - \overleftarrow{\partial} \cdot \mathcal{A}_\gamma \right) - \frac{e^2}{m} \mathcal{A}_\gamma \cdot \mathcal{A}^c \,. \tag{6.7}$$

Similar to the derivation in the single-pulse case, we introduce auxiliary functions allowing us to bring the S-matrix element in the convenient form

$$\mathcal{S}^c_{p_+ p_-} = S_0 \int d^4x \, C^c \, e^{-iQ \cdot x - iH^c} \tag{6.8}$$

with the same prefactor $S_0 = iem\sqrt{\frac{2\pi}{V^3 E_{p_+} E_{p_-} \omega_\gamma}}$ and combined momentum vector $Q^\mu = k^\mu_\gamma - \left(p^\mu_+ + p^\mu_-\right)$ as before. Differences occur in the reduced matrix element C^c, which now reads

$$C^c = C_0 + \sum_{j=1}^{2} C_j \tag{6.9}$$

with

$$\begin{aligned} C_0 &= \frac{p_- - p_+}{2m} \cdot \epsilon_\gamma \,, \\ C_j &= \frac{e\mathcal{A}_j(\eta_j)}{m} \cdot \epsilon_\gamma \,. \end{aligned} \tag{6.10}$$

Furthermore, the auxiliary function H^c is extended according to

$$H^c = H_1 + H_2 \tag{6.11}$$

with contributions stemming from the individual pulses

$$
\begin{aligned}
H_j &= \int_0^{\eta_j} h_j(\eta - \delta_j) \mathcal{X}_{[0,2\pi]}(\eta - \delta_j) d\eta \,, \\
h_j(\eta - \delta_j) &= \sum_{l=1}^{2} h_{lj} f_j^l(\eta - \delta_j) \,,
\end{aligned}
\tag{6.12}
$$

revealing the explicit dependence on the phase shifts. We finally introduce the abbreviations

$$
\begin{aligned}
h_{1,j} &= -e a_j \left[\frac{\epsilon_j \cdot p_+}{k_j \cdot p_+} - \frac{\epsilon_j \cdot p_-}{k_j \cdot p_-} \right] , \\
h_{2,j} &= -\frac{e^2 a_j^2}{2} \left[\frac{1}{k_j \cdot p_+} + \frac{1}{k_j \cdot p_-} \right] .
\end{aligned}
\tag{6.13}
$$

With regard to the space-time integration required in Eq. (6.8), we note that C^c and H^c depend only on the light-cone-minus coordinate x^-, since $\eta_j = k_j^0 x^-$. Accordingly, we begin with the integrals along x^+ and $\mathbf{x}^\perp$, which brings us to the familiar form

$$
\mathcal{S}^c_{p_+ p_-} = (2\pi)^3 S_0 \delta(Q^-) \delta^{(2)}(\mathbf{Q}^\perp) \int dx^- \, C^c \, e^{-iQ^0 x^- - iH^c} \,. \tag{6.14}
$$

Inspecting the reduced matrix element C^c, the terms C_1 and C_2 are recognized to be restricted to the phase interval of the respective pulse. In contrast, C_0 is not restricted. Concerning H^c, we regard the phase dependence of the contributions H_j, which can be summarized by accounting for the effect of the characteristic function $\mathcal{X}_{[0,2\pi]}(\eta - \delta_j)$ in the form

$$
H_j = \begin{cases} 0, & \text{for } \eta_j < \delta_j \\ \int_{\delta_j}^{\eta_j} h_j(\eta - \delta_j) d\eta, & \text{for } \eta_j \in (\delta_j, \delta_j + 2\pi) \\ H_j^\star = \int_{\delta_j}^{\delta_j + 2\pi} h_j(\eta - \delta_j) d\eta, & \text{for } \eta_j > \delta_j + 2\pi \,. \end{cases} \tag{6.15}
$$

For $\eta_j > \delta_j + 2\pi$, the value of H_j is constant and shall be denoted by $H_j^\star$.
The integral proportional to C_0 can now be regularized in analogy to the treatment presented for the single-pulse case in Sec. 2.2.1. For $\varepsilon > 0$, we introduce a damping factor $e^{-\varepsilon |x^-|}$ and integrate by parts according to

$$
\begin{aligned}
&\int dx^- e^{-iQ^0 x^- - iH^c - \varepsilon |x^-|} = \\
&= \left[\frac{e^{-iQ^0 x^- - iH^c - \varepsilon |x^-|}}{-iQ^0 - \varepsilon \,\mathrm{sign}(x^-)} \right]_{-\infty}^{\infty} - \int dx^- \frac{-i \frac{dH^c}{dx^-}}{-iQ^0 - \varepsilon \,\mathrm{sign}(x^-)} e^{-iQ^0 x^- - iH^c - \varepsilon |x^-|} \,.
\end{aligned}
\tag{6.16}
$$

As can be seen from Eq. (6.15), the derivatives $\frac{dH_j}{dx^-}$ vanish outside the pulse intervals, i.e.

$$
\frac{dH_j}{dx^-} = k_j^0 \, h_j(k_j^0 x^- - \delta_j) \, \mathcal{X}_{[0,2\pi]}(k_j^0 x^- - \delta_j) \,, \tag{6.17}
$$

which restricts the integration domain. Assuming weak damping $\varepsilon \ll |Q^0|$, we thus obtain the regularized integral

$$
\int dx^- e^{-iQ^0 x^- - iH^c} \equiv \sum_{j=1}^{2} \frac{-k_j^0}{Q^0} \int dx^- \frac{dH_j}{d\eta_j} e^{-iQ^0 x^- - iH^c} \,. \tag{6.18}
$$

Accordingly, we can define a reduced matrix element

$$\tilde{C}^c = \tilde{C}_1 + \tilde{C}_2 \tag{6.19}$$

where for each part $\tilde{C}_j$, the x^- integration is restricted to the phase interval of the respective pulse. They can be brought into the form

$$\tilde{C}_j = C_j - \frac{k_j^0}{Q^0}\frac{dH_j}{d\eta_j}C_0 = \sum_{l=1}^{2} \tilde{g}_{lj}\, f_j^l(\Phi_j)\mathcal{X}_{[0,2\pi]}(\Phi_j) \tag{6.20}$$

with $\Phi_j = k_j^0 x^- - \delta_j$ and constants

$$\begin{aligned} \tilde{g}_{1,j} &= \frac{ea_j}{m}\epsilon_j \cdot \epsilon_\gamma - \frac{k_j^0}{Q^0}\frac{(p_- - p_+)\cdot \epsilon_\gamma}{2m} h_{1,j}\,, \\ \tilde{g}_{2,j} &= -\frac{k_j^0}{Q^0}\frac{(p_- - p_+)\cdot \epsilon_\gamma}{2m} h_{2,j}\,, \end{aligned} \tag{6.21}$$

where h_{lj} was defined in Eq. (6.13) for $l = 1, 2$. This way, we can express the S-matrix element from Eq. (6.14) as

$$\mathcal{S}^c_{p_+p_-} = (2\pi)^3 S_0 \delta(Q^-)\delta^{(2)}(\mathbf{Q}^\perp) \int dx^-\, \tilde{C}^c\, e^{-iQ^0x^- - iH^c}\,. \tag{6.22}$$

The pair-creation probability can now be obtained in full analogy to the case of a single pulse by following the steps after Eq. (2.30). In the case of Dirac particles, similar structures arise.

6.2 General properties

In the following, we will inspect the structure of the pair-creation amplitude obtained in the combined laser field in more detail. In particular, we will focus on the question in which way the presence of an additional pulse affects the process. As a first step, we rearrange the S-matrix amplitude, allowing us to identify contributions from the individual pulses.

6.2.1 Identifying contributions from the individual pulses

Owing to the vanishing overlap between the two pulses, the S matrix in Eq. (6.22) can be decomposed into contributions from the individual pulses. To this end, we regard the separate parts

$$I_j = \int dx^- \tilde{C}_j e^{-iQ^0x^- - iH_j} \tag{6.23}$$

where we explicitly took H_j in the exponent. Due to the restriction of the integration domain, the contribution of the other pulse $H^c - H_j$ to the exponent is constant. Furthermore, recalling Eq. (6.15), we rewrite H_j inside the integration domain by means of a substitution as

$$H_j = \int_{\delta_j}^{\eta_j} \sum_{l=1}^{2} h_{lj} f_j^l(\eta - \delta_j)\, d\eta = \sum_{l=1}^{2} h_{lj} \int_0^{\Phi_j} f_j^l(\tilde{\Phi}_j)\, d\tilde{\Phi}_j \equiv H_j(\Phi_j) \tag{6.24}$$

with $\Phi_j = \eta_j - \delta_j$ as before.

Inspecting $\tilde{C}_j$ in Eq. (6.20), we reformulate the integral I_j via substituting $x^- = (\Phi_j + \delta_j)/k_j^0$ as

$$I_j = F_j\, e^{-iQ^0\delta_j/k_j^0} \tag{6.25}$$

with

$$F_j = \frac{1}{k_j^0}\sum_{l=1}^{2}\tilde{g}_{lj}\int_0^{2\pi} d\Phi_j\, f_j^l(\Phi_j)e^{-iQ^0\Phi_j/k_j^0 - iH_j(\Phi_j)}\,. \tag{6.26}$$

This way, the only dependence on δ_j is absorbed in the factor $e^{-iQ^0\delta_j/k_j^0}$, while F_j is entirely independent of δ_j.[1]
As a consequence, the S matrix describing the complete process can be written as

$$\mathcal{S}^c_{p_+p_-} = (2\pi)^3 S_0\,\delta(Q^-)\delta^{(2)}(\mathbf{Q}^\perp)\left(F_1 + F_2\, e^{-iH_1^\star - iQ^0\varDelta}\right) \tag{6.27}$$

for $\delta_1 = 0$, which can be chosen without loss of generality. The remaining phase-shift parameter δ_2 can now be employed to describe the distance $\varDelta = \delta_2/k_2^0$ between the fronts of the pulses.
The partial amplitudes F_j depend exclusively on the pulse with number j. Due to the substitution introduced in Eq. (6.25), both integrals F_j are effectively evaluated at phase zero. As we will see in the following, the phase factor $e^{-iH_1^\star - iQ^0\varDelta}$ adjusts the phases of the particles and of the gamma quantum in order to account for the temporal delay between the pulses. Before discussing further implications, we investigate this factor in more detail.

6.2.2 The phase factor

In order to understand the structure of the phase

$$\phi = H_1^\star + Q^0\varDelta \tag{6.28}$$

occurring in Eq. (6.27), we recall that $Q^\mu = k_\gamma^\mu - (p_+^\mu + p_-^\mu)$. Accordingly, the term $Q^0\varDelta$ describes the phase development of the free momenta $p_\pm$ and k_γ. The relative sign between the phases of the particles and of the gamma quantum follows from the structure of the S matrix, see Eq. (6.6). Furthermore, we note that H_j arises in Eq. (6.12) as $H_j = \Lambda_j^- - \Lambda_j^+$, where $\Lambda_j^\pm$ describes the effect of the laser pulse j on the phases of the Gordon-Volkov states [see Eq. (6.4)]. Hence, $H_1^\star$ contains the full effect of the first pulse on the phases of the charged particles.
Following a more intuitive approach, the phase ϕ can also be understood by employing the concept of laser-dressed states: To this end, we bring $H_j^\star$ into the form

$$H_j^\star = 2\pi\mu_j\,,\ \text{with } \mu_j = \sum_{l=1}^{2} h_{lj}\langle f_j^l\rangle\,. \tag{6.29}$$

As we have seen in Sec. 2.2.3, μ_j is a measure for the dressing of the particles due to the laser pulse j, i.e. $\mu_j = -w_j$, where w was introduced for a single pulse in Eq. (2.39). Denoting the length of the pulses by $L_j = 2\pi/k_j^0$ allows us to bring ϕ into the form

$$\phi = Q^0\varDelta + H_1^\star = (Q^0 + \mu_1 k_1^0)L_1 + Q^0(\varDelta - L_1)\,. \tag{6.30}$$

[1] In App. A.7, we briefly show how F_j can be Fourier expanded, which is the usual way of computing these expressions. However, taking advantage of the finite integration domain, we have actually computed F_j by means of a direct numerical integration.

The first term describes the phase development in the presence of the first pulse. The average action of the pulse on the charged particles is accounted for by means of the dressed states, which can be seen from

$$Q^0 + \mu_1 k_1^0 = k_\gamma^0 - \left(p_+^0 + p_-^0 + w_1 k_1^0\right) . \tag{6.31}$$

This expression can also be recognized as the (negative of the) absorbed photon energy E_L which was introduced for the case of a single pulse in Eq. (2.42). Since the particles are subject to the full length of the first pulse, the uncertainty inherent to the dressing approach is completely cured. The second term in Eq. (6.30) describes the phase development in the gap between the pulses. In the following, we will denote the extent of the gap by

$$D = \mathit{\Delta} - L_1 \, , \tag{6.32}$$

see Fig. 6.1.

Having understood the phase factor, we will now continue the discussion of the form of the combined S-matrix amplitude.

6.2.3 Conclusion

As we have seen before, the structure of the combined S-matrix element from Eq. (6.27) is of the form

$$\mathcal{S}^c_{p_+p_-} \sim F_1 + F_2 \, e^{-i\phi} \, , \tag{6.33}$$

where the F_j denote the individual contributions of the pulses. The amplitude of the combined process is subject to quantum two-pathway interferences between these contributions. The interference phase is determined by ϕ, which describes the development of the particles' phases between the pulse fronts. Despite ϕ being explicitly dependent on the properties of the first pulse, the effect of the first pulse on the contribution of the second pulse is limited to this phase factor. Nevertheless, as we shall see, this phase factor can induce a rich variety of effects.

6.3 Two-pulse interference

In the following, we will investigate the interference effects arising due to the presence of an additional pulse. Restricting ourselves to the production of scalar particles, the superscript "KG", which was introduced in Eq. (2.30), will be dropped. As we have seen in the previous chapter, the angular distributions of Dirac and KG particles can be vastly different. However, in this chapter, we rather focus on the influence of the second pulse. The main conclusions are independent of the actual shape of the angular distributions, such that these simplified KG calculations are sufficient to understand the behavior. We begin with the case of two identical pulses with a variable distance, allowing us to inspect and understand the basic properties and the general behavior in a simplified environment. Afterwards, the case of two different pulses will be addressed.

6.3.1 Two identical pulses

We begin with the case of two identical pulses with a distance $\mathit{\Delta}$ between their fronts, i.e. $F_2 = F_1 \equiv F$. The combined S matrix is of the form

$$\mathcal{S}^c_{p_+p_-} \sim F(1 + e^{-i\phi}) \text{ with } \phi = Q^0 \mathit{\Delta} + H_1^\star \,. \tag{6.34}$$

In comparison, if only one of the two pulses was present, the S matrix would contain only one term

$$\mathcal{S}_{p_+p_-} \sim F \,. \tag{6.35}$$

Accordingly, the presence of the second pulse induces a factor $(1+e^{-i\phi})$ in the amplitude. In the case of a double pulse, the absolute square reads

$$|\mathcal{S}^c_{p_+p_-}|^2 \sim 2\,|F|^2\,[1+\cos(\phi)] \ , \tag{6.36}$$

giving rise to the differential probability

$$\frac{d^3\mathscr{P}^c}{dp_+ d^2\Omega_{p_+}} = \frac{\alpha m^2}{16\pi^2\omega_\gamma}\sum_{\lambda_\gamma}\frac{|\mathbf{p}_+|^2}{E_{p_+}(k_\gamma^- - p_+^-)}\,2|F|^2\,[1+\cos(\phi)] = \frac{d^3\mathscr{P}}{dp_+ d^2\Omega_{p_+}}2\,[1+\cos(\phi)] \ , \tag{6.37}$$

where we recall that F and ϕ depend on the particle momenta. Here, we denote the absolute value of the positron momentum as $p_+ = |\mathbf{p}_+|$. On the level of the differential probability, the presence of the second pulse leads to a factor $2\,[1+\cos(\phi)]$. Accordingly, in the extreme cases, the process probability in the combined field can be completely suppressed, or amplified by a factor of four in comparison with the case of a single pulse. The effect of this factor on the resulting pair-creation spectra shall now be investigated further.

6.3.1.1 Angular distributions

Employing the same shape function [cp. Eq. (2.11)] as before, we begin with a single four-cycle pulse with moderate amplitude $\xi_{\max} = 0.1$ and regard the fully differential angular distributions for two different positron momenta p_+ in the two rows of Fig. 6.2. The first column depicts the angular distributions $\frac{d^3\mathscr{P}}{dp_+ d^2\Omega_{p_+}}$ obtained in a single pulse. For $p_+ = 0.33m$, the contribution is enhanced in the propagation direction of the gamma quantum, whereas for $p_+ = 0.53m$, the contribution is enhanced in the laser-propagation direction. The second column depicts the combined momentum spectrum obtained when a second,

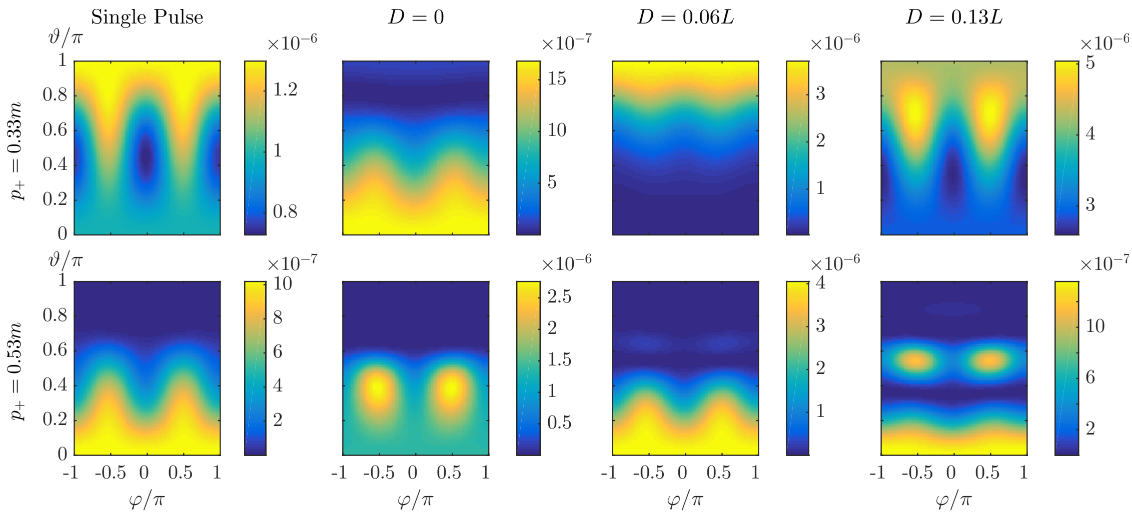

Figure 6.2: The first column depicts the fully differential angular distributions $\frac{d^3\mathscr{P}}{dp_+ d^2\Omega_{p_+}}$ (in units of $1/m$) for $p_+ = 0.33m$ (first row) and $p_+ = 0.53m$ (second row) obtained from a single pulse with $N_{\text{osc}} = 4$, $\omega_c = \omega_\gamma = 1.01m$, $\xi_{\max} = 0.1$, and $\chi = 0$. The remaining three columns show the combined momentum spectra $\frac{d^3\mathscr{P}^c}{dp_+ d^2\Omega_{p_+}}$ for the cases when a second, identical pulse follows shortly after the first pulse. From left to right, we increase the width D of the gap, which is indicated in units of the length $L = 2\pi N_{\text{osc}}/\omega_c$ of the individual pulses.

identical pulse follows directly after the first pulse, i.e. $D = 0$. For $p_+ = 0.33m$, main contributions are now obtained from the laser-propagation direction, and for $p_+ = 0.53m$, the emission pattern is peaked at $\vartheta \approx 0.4\pi$ and $\varphi \approx \pm 0.5\pi$.

The difference with the angular distributions of the single-pulse case is entirely induced by the factor $2\,[1 + \cos(\phi)]$, which shall be referred to as $q^{(3)}$. The latter can be understood as the ratio between the triple-differential angular distributions of the double pulse and the single pulse. With $D = 0$, the phase ϕ can be written as

$$-\phi = E_L L \tag{6.38}$$

where E_L denotes the energy which is required to produce the pair in one of the pulses, and $L = 2\pi N_{\text{osc}}/\omega_c$ denotes the length of the individual pulses. Thus, at this point, the laser-dressed energy E_L enters explicitly into the pair-creation probabilities. We recall that E_L generally depends both on the positron momentum and on the emission angles. For the present parameters, the process at $p_+ \approx 0.14m$ happens approximately in a c.m. system. Hence, for higher positron momenta, the width of the interval of relevant photon energies $E_L(\vartheta, \varphi)$ generally grows with p_+. While $q^{(3)}$ barely completes a half-cycle as ϑ is varied at $p_+ = 0.33m$, more than two full cycles are completed for $p_+ = 0.53m$. Concerning φ, we note that the laser dressing induces a small dependence in E_L, which leads to a modulation ($\Delta q^{(3)}/q^{(3)} \lesssim 25\%$ for the preferred directions), which is, however, smaller than the dominant modulations along ϑ.[2]

[2]The dressing affects E_L by less than one percent. However, with regard to the phase term, the relevant scale is given by the period length, such that these small effects in E_L can induce much stronger effects in $q^{(3)}$.

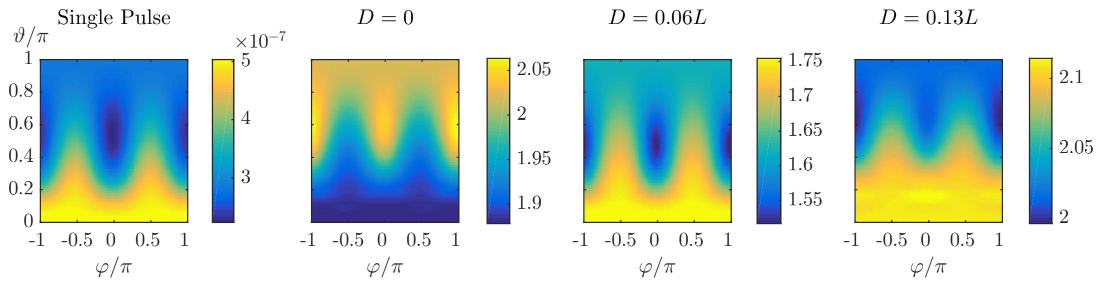

Figure 6.3: The first panel depicts the momentum-integrated angular distribution $d^2\mathscr{P}/d^2\Omega_{p_+}$ obtained for a single pulse. For a double pulse, the ratio $q^{(2)}$ [see Eq. (6.40)] is presented for various interpulse distances D in the remaining panels. The parameters are the same as in Fig. 6.2.

As a next step, we increase the interpulse distance D. The third and fourth columns in Fig. 6.2 depict the cases of $D = 0.06L$ and $D = 0.13L$, respectively. The angular distributions are found to be strongly sensitive to the interpulse distance: Both the emission directions and the emission patterns change entirely. For $p_+ = 0.53m$, a particularly pronounced emission pattern emerges at $\vartheta \approx \varphi \approx \pi/2$ for $D = 0.13L$.

When the second pulse arrives after a gap D, the phase ϕ receives the additional term $Q^0 D$. We note that Q^0 can be recognized as the (negative of the) photon energy E_0 which is required in order to produce the pair without dressing effects. Accordingly, we write the phase in the form

$$-\phi = E_L L + E_0 D \tag{6.39}$$

which helps to understand the dependence on the positron momentum. We see that increasing the gap width amplifies the momentum dependence of the phase and thereby enhances the modulating effects. As D grows, $q^{(3)}$ completes an increasing number of oscillations when ϑ is varied. The asymptotic behavior will be discussed below.

Next, we integrate the angular distributions over the absolute value of the positron momentum, i.e. we regard $d^2\mathscr{P}/d^2\Omega_{p_+}$. For the case of a single pulse, the resulting distribution is depicted in the first panel of Fig. 6.3. The dominant contributions are obtained in the laser-propagation direction, but also other directions are important. When the second pulse is included, the combined distribution $d^2\mathscr{P}^c/d^2\Omega_{p_+}$ appears qualitatively similar to the single-pulse case. In order to demonstrate the differences, we regard the ratio

$$q^{(2)} = \left[\frac{d^2\mathscr{P}^c}{d^2\Omega_{p_+}}\right] \Big/ \left[\frac{d^2\mathscr{P}}{d^2\Omega_{p_+}}\right], \tag{6.40}$$

which is depicted in the remaining three panels of Fig. 6.3 for various interpulse distances D. For a given value of D, the ratio $q^{(2)}$ varies both in ϑ and φ by $\lesssim 10\%$. The angular pattern and in particular the average values of $q^{(2)}$ clearly change as D is increased. However, these changes and the modulations along ϑ are weaker than those in $q^{(3)}$. Since the ratio $q^{(2)}$ is obtained after the integration over the absolute value of the positron momentum is carried out, $q^{(2)}$ can be regarded as an average of $q^{(3)}$, based on the underlying pair-production probabilities.

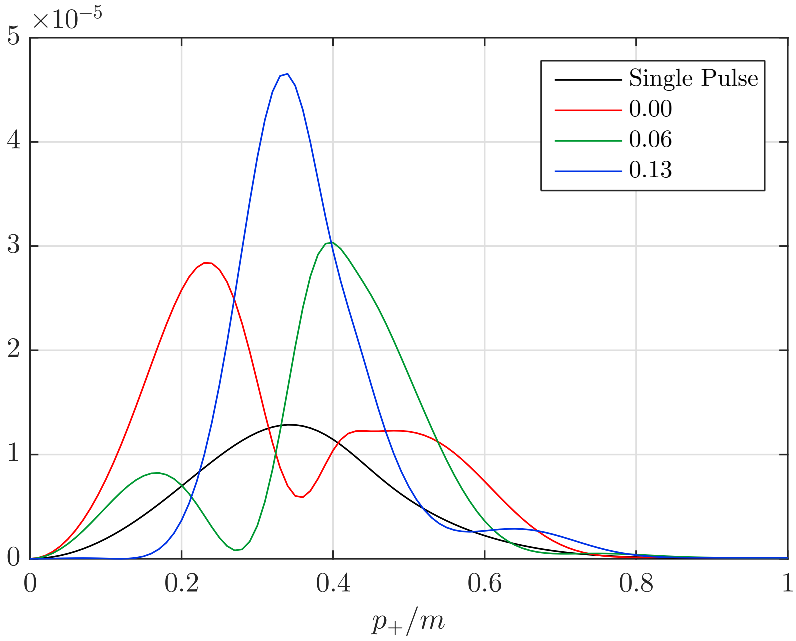

Figure 6.4: The black line shows the positron momentum spectrum $d\mathscr{P}/dp_+$ (in units of $1/m$) obtained from a single pulse. The colored lines show the combined momentum spectra $d\mathscr{P}^c/dp_+$ for the cases when a second, identical pulse follows shortly after the first pulse. The different colors refer to different gap widths D, which are indicated in the legend in units of the length L of the individual pulses. The parameters are the same as in Fig. 6.2. Originally published in [JM16b].

6.3.1.2 Momentum spectra

In this section, we discuss the momentum spectra of the produced particles, which are obtained after integrating the triply differential probabilities over the emission directions. Employing the same parameters as in the previous section, the momentum spectrum $d\mathscr{P}/dp_+$ obtained from a single pulse is presented as the black line in Fig. 6.4. It possesses a rather simple structure with a maximum at $p_+ \approx 0.34m$. When we add a second repetition of the same pulse, the resulting momentum spectrum becomes much more involved: The red line in Fig. 6.4 depicts the situation where the second pulse follows directly after the first, i.e. $D = 0$. The resulting momentum spectrum obtains a main maximum at $p_+ \approx 0.23m$, where the probability is approximately three times higher than in the single-pulse case. Conversely, at $p_+ \approx 0.36m$, just slightly off the position of the single-pulse maximum, the double-pulse distribution obtains a pronounced minimum, where the probability is smaller by a factor of two than for the single pulse. For $p_+ \approx 0.5m$, the double-pulse distribution possesses a plateau, where the probability is again substantially higher than for the single pulse.
From our previous discussion, we know that these effects are induced by the factor $q^{(3)} = 2[1 + \cos(\phi)]$, which is now averaged over the emission directions of the positron. For the present parameters, the process at $p_+ \approx 0.14m$ happens approximately in a c.m. system, such that all phase factors are approximately the same. In fact, the corresponding ratio between the double-pulse and the single-pulse probabilities is just slightly less than four, which is the maximum possible value. Especially for higher momenta, E_L becomes angle dependent and the oscillating terms tend to cancel. However, in comparison with $q^{(2)}$,

we note that the integration over the emission angles has a weaker damping effect than the integration over the absolute value of the positron momentum. The plateau structure arises when the factor $\cos(\phi)$ grows as a function of p_+, while the single-pulse probability drops.
In general, slightly increasing the gap width D allows a certain value of the phase ϕ to be achieved with slightly less energy (or momentum). Accordingly, the locations of the extrema in the momentum spectrum are shifted to smaller energies. In Fig. 6.4, this behavior can (still) be recognized by comparing the red and the green curves, where the latter is obtained for $D = 0.06L$. Overall, we see that the momentum spectrum depends very sensitively on the gap width. A particular case occurs for $D = 0.13L$, which is depicted as the blue curve. There, production of positrons with $p_+ \lesssim 0.15m$ is strongly suppressed, while the probability for positrons with $p_+ \approx 0.33m$ is enhanced by a factor of ≈ 3.6. The angular distribution of these positrons is depicted in the top right panel of Fig. 6.2, which is more pronounced than in the single-pulse case (see top left panel).
Comparing the angular distributions and the momentum spectra, one can see that the second pulse acts in some cases like a collimator for the produced particles. However, due to the strong momentum dependence of the phase ϕ, these collimating properties are restricted to a certain energy range. This can be seen by regarding the momentum-integrated angular distributions in Fig. 6.3, where the effect of the second pulse is damped.

6.3.1.3 Total probability

As a next step, we regard the effect of the second pulse on the total probabilities. Employing the same parameters as before, the ratio $q = \mathscr{P}^c/\mathscr{P}$ between the total probabilities for the double pulse and the single pulse is presented in Fig. 6.5. The ratio exhibits a damped, oscillatory behavior as the gap width grows. Starting with $q \approx 1.96$ for vanishing gap width, the ratio arrives at its minimum value close to $D \approx 0.06L$ where $q \approx 1.65$. The corresponding momentum spectrum was presented as the green line in Fig. 6.4, and the angular distributions were investigated in the previous figures. For $D = 0.13L$, a ratio $q \approx 2.07$ is found, while the maximum value $q \approx 2.3$ is achieved for $D \approx 0.18L$. These results clearly show that also the total probability is subject to pronounced interference effects, which are highly sensitive to the pulse distance.
In order to understand the characteristic dependence on the interpulse distance, we note that $\mathscr{P}^c$ is obtained as an integration of the form [cp. Eq. (6.37)]

$$\mathscr{P}^c = \int d^3\mathbf{p}_+ \, \varrho(\mathbf{p}_+) \, 2\left[1 + \cos(E_L L + E_0 D)\right] \tag{6.41}$$

where we use the single-pulse probability density

$$\varrho(\mathbf{p}_+) = \frac{d^3\mathscr{P}}{d^3\mathbf{p}_+} = \frac{\alpha m^2}{16\pi^2\omega_\gamma} \sum_{\lambda_\gamma} \frac{|F|^2}{E_{p_+}(k_\gamma^- - p_+^-)} \,. \tag{6.42}$$

With regard to Eq. (6.41), we recall that E_0 and E_L both depend on $\mathbf{p}_+$. For an analytical approach, these dependencies can in principle be expressed in closed form, but the probability density remains out of reach.
The integration in Eq. (6.41) is restricted to those particle momenta for which the probability density $\varrho(\mathbf{p}_+)$ gives significant contributions. In our previous examples, we have $|\mathbf{p}_+| \lesssim 1.5m$. When the momentum is varied, the phase factor induces oscillations. These oscillations become faster as the pulse distance grows. When D is sufficiently large, these

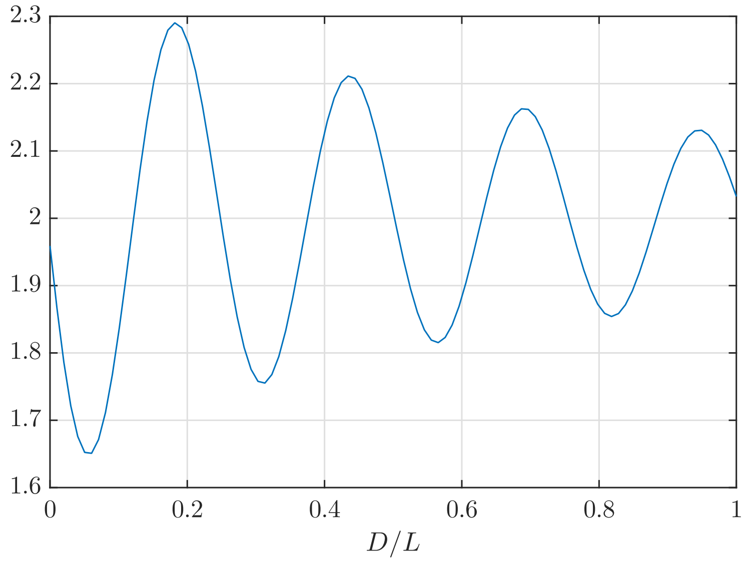

Figure 6.5: The ratio of the fully integrated pair-production probabilities $q = \mathscr{P}^c/\mathscr{P}$ as a function of the pulse distance for the same parameters as in Fig. 6.2.

oscillations are much faster than any variation in $\varrho(\mathbf{p}_+)$. As a consequence, in the limit of large pulse distances, the cosine term can well be approximated by its average and thus vanishes. Hence, we see that $q \to 2$ for large pulse distances, which means that the combined probability is simply obtained as the sum of the contributions of the single pulses.

When we regard the differential probabilities in Eq. (6.37), the phase factor remains also for large values of D. Nevertheless, any detection process is based on an integration over a certain energy range or angular region. In the limit of large pulse distances, based on the same argument as before, the angular distributions and the energy spectra of the detected particles thus approach the single-pulse patterns, with the probabilities being twice as large as in the single-pulse case.

A further understanding of the dependence of the ratio q on D can be gained within a simplified model approach. To this end, we note that q can be understood as the average of $2\,[1+\cos(E_L L + E_0 D)]$ with respect to the probability density ϱ, i.e. $q = 2+2\langle\cos(E_L L + E_0 D)\rangle_\varrho$. As a first simplification, we assume that $E_L \approx E_0$, which is valid when the dressing effects are small. The integration in Eq. (6.41) can then be expressed as an integral over the absorbed energy E_L

$$\mathscr{P}^c = \int dE_L\, \varrho(E_L)\, 2\,[1+\cos(E_L[L+D])] \tag{6.43}$$

where $\varrho(E_L)$ is obtained as the two-dimensional integral of $\varrho(\mathbf{p}_+)$ over those momenta with constant E_L. We denote the average absorbed energy by $\langle E_L\rangle$, and the width of the distribution $\varrho(E_L)$ by ΔE_L. Using only these information, we adopt the model assumption that $\varrho(E_L)$ can be described by a normal distribution

$$\varrho(E_L) = \frac{1}{\sqrt{2\pi(\Delta E_L)^2}} \exp\left(-\frac{(E_L - \langle E_L\rangle)^2}{2(\Delta E_L)^2}\right) \tag{6.44}$$

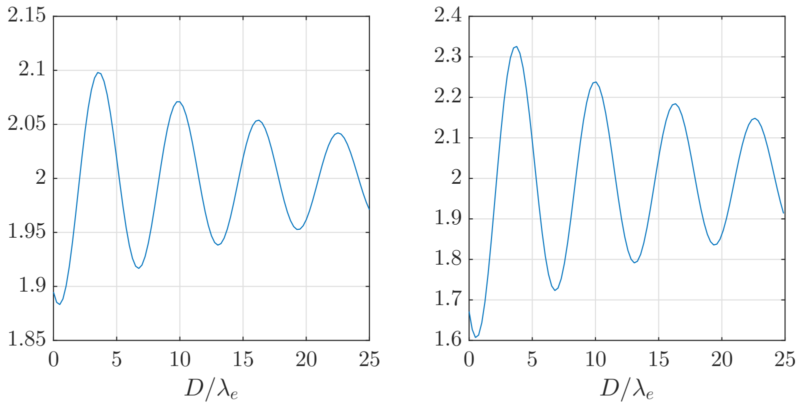

Figure 6.6: The ratio q as a function of the pulse distance D for similar parameters as in Fig. 6.5, where $\xi_{\max} = 0.1$, $\omega_c = 1.01m$ and $L \approx 24.8\lambda_e$. We recall that $\lambda_e = 1/m$ denotes the Compton wavelength. Here, we show the behavior for $\xi_{\max} = 0.1$ and $\omega_c = 0.505m$ (left) and for $\xi_{\max} = 0.5$ and $\omega_c = 1.01m$ (right). In both cases, the remaining parameters are the same as in Fig. 6.5.

and obtain[3]

$$q = 2 + 2\, e^{-(\Delta E_L [L+D]/2)^2} \cos\left(\langle E_L \rangle [L + D]\right) . \tag{6.45}$$

This expression illustrates in a semiquantitative manner how the ratio q depends on the pulse distance, and qualitatively reflects the numerically obtained result depicted in Fig. 6.5. For large distances D, q approaches the asymptotic value 2. The decay rate is determined by the width ΔE_L of the distribution of absorbed energies. Furthermore, q oscillates in D, with a periodicity being determined by the average absorbed energy $\langle E_L \rangle$. We note that $\langle E_L \rangle$ and ΔE_L depend on the pulse spectrum and on the details of the pair-production process, and that the distance between neighboring zeros of $q(D) - 2$ is actually not constant. The agreement between $q(D)$ and a numerical fit of the form suggested by Eq. (6.45) depends on the interaction parameters. Here, $q(D)$ decays slower than the Gaussian.

For the present parameters, the process is mostly driven via absorption of one laser photon of the central frequency. When we reduce[4] the central frequency to half of its original value, i.e. $\omega_c = 0.505m$, the process is dominated by two-photon absorption. Still, the ratio $q(D)$ exhibits a similar behavior with damped oscillations, albeit with a smaller amplitude, see left panel of Fig. 6.6. One reason for the stronger damping is certainly given by the increased length L of the pulses. We finally note that for the original $\omega_c = 1.01m$, but higher field strength $\xi_{\max} = 0.5$, the behavior remains similar, see right panel of Fig. 6.6.

Before we proceed to the case of two non-identical pulses, we remark that a related work was presented in [KK14], where the SFBW process was investigated in a scenario comprising a train of identical pulses, which followed each other without delay. There, the emphasis was put on the fully differential energy spectra of the produced particles, where a comb-like structure arises as the number of pulses is increased. Regarding laser-induced nonlinear Compton scattering, which exhibits similar properties as the pair-creation process, the effect of the time delay was briefly addressed in [KTK14]. The distance between

[3]Equation (6.45) is obtained when the integration domain in Eq. (6.43) is extended to the entire real axis. Due to the decay of the Gaussian distribution, this is a valid approximation when $\Delta E_L \ll \langle E_L \rangle$.

[4]The transition between $\omega_c = 1.01m$ and $\omega_c = 0.505m$ reveals complicated behavior of $q(D)$. In particular for $\omega_c = 0.707m$, the envelope of the oscillations is non-monotonous in D.

the combs in the (fully differential) energy spectra of the Compton photons were shown to be sensitive to the pulse distance.
Besides, some studies of pair production in purely time-dependent fields (employing the framework of quantum kinetic theory) have also investigated field configurations comprising several, not necessarily identical, pulses with a variable delay [AD12, KMvW$^+$13, LLX$^+$14]. The effects have some similarity to our case. In particular, after integrating the probabilities over one momentum component, a quasi-periodical dependence on the delay arises, as well, which can in principle be understood from our perspective.

6.3.2 Different pulses

In this section, we regard two different pulses that shall arrive with various distances D and in particular in different orders. We employ the same four-cycle pulse as before, and an additional stronger three-cycle pulse with a smaller central frequency. The parameters are

$$\begin{aligned} &\text{Pulse A:} \quad N_{\text{osc}} = 4, \quad \xi_{\max} = 0.1, \quad \omega_c = 1.01m, \\ &\text{Pulse B:} \quad N_{\text{osc}} = 3, \quad \xi_{\max} = 0.2, \quad \omega_c = 0.808m\,. \end{aligned} \tag{6.46}$$

If not stated otherwise, the CEP of both pulses is chosen as $\chi_A = \chi_B = 0$. The polarization vectors of both pulses are parallel. The gamma-quantum energy remains at $\omega_\gamma = 1.01m$. As in the previous section, we begin with the fully differential angular distributions.

6.3.2.1 Angular distributions

From Eq. (6.33), we expect that the process is sensitive to the order in which the two pulses arrive, since the phase factor depends exclusively on the first pulse. In Fig. 6.7, we depict the fully differential angular distributions for the individual pulses A and B in the first and second panel, respectively. The comparison once more reveals the sensitivity of the process to the laser parameters. Next, we regard the case when pulse A arrives first, and B follows immediately, with vanishing distance D. The resulting angular distribution is depicted in the third panel of Fig. 6.7. The emission pattern qualitatively resembles the distribution obtained in pulse A, which is the dominant one. Still, the combined probability is clearly not just given by the sum of the individual contributions, but subject to interference processes, which can most clearly be seen by comparing the probabilities along the collision axis ($\vartheta \approx 0, \pi$).

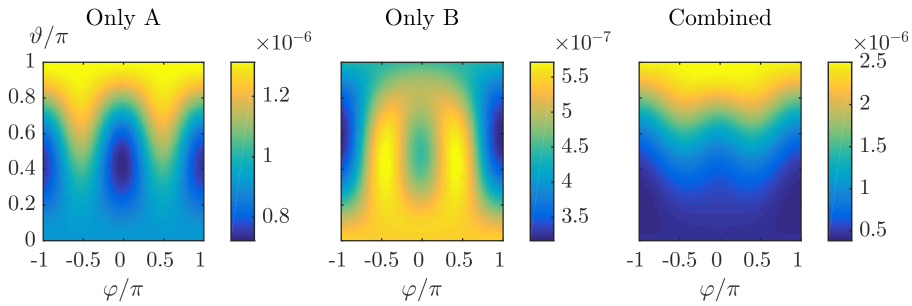

Figure 6.7: Fully differential angular distributions $\frac{d^3\mathscr{P}}{dp_+ d^2\Omega_{p_+}}$ (in units of $1/m$) for $p_+ = 0.31m$. The first two panels depict the probabilities obtained in the individual pulses A and B [see Eq. (6.46)]. The third panel shows the combined probability obtained when both pulses arrive immediately after each other. For the present parameters with $\chi_A = \chi_B = 0$, the process remains invariant when the pulses arrive in inverted order.

Now, we interchange the order in which the pulses arrive, i.e. pulse B arrives first, and pulse A follows immediately. Still, we find the same angular distribution as in the original ordering. This result is quite striking, since Eq. (6.27) [or (6.33)] clearly suggests an asymmetry between the two pulses.

In order to investigate the situation further, we change the CEP of the pulses. In Fig. 6.8, we present the angular distributions for the same parameters as before, but with $\chi_B = \pi/2$ for pulse B. The individual contribution of pulse B is only moderately affected by this change. The combined distributions, however, are now clearly sensitive to the ordering of the pulses. As can be seen by comparing the third and fourth panel of Fig. 6.8, the temporal ordering strongly affects the emission patterns and the magnitude of the probabilities. In the case when pulse B arrives first (fourth panel), the combined distribution resembles the distribution obtained in pulse A. However, when the gap width D is changed, the emission patterns change completely again. This can be seen by comparing with Fig. 6.9, where the combined angular distributions are depicted for $D = 3\lambda_e$, which is $\sim 10\%$ of the pulse lengths.

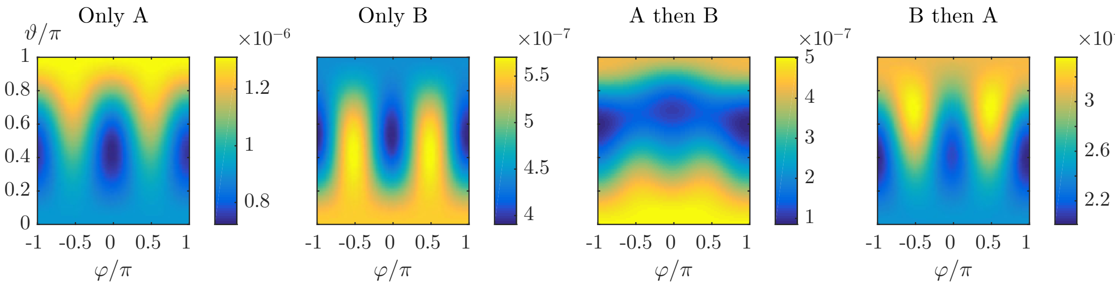

Figure 6.8: Fully differential angular probabilities for the same parameters as in Fig. 6.7, except $\chi_B = \pi/2$. Here, the ordering of the pulses clearly affects the process.

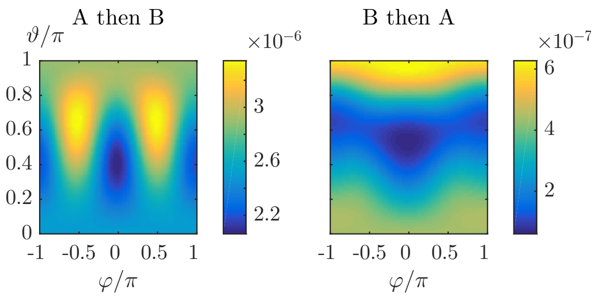

Figure 6.9: Fully differential angular probabilities for the same parameters as in Fig. 6.8 but with a gap width of $D = 3\lambda_e$.

These examples show that the sensitivity of the process to the temporal ordering of the pulses is connected to the CEP. Accordingly, this effect can only be understood from Eq. (6.27) when we regard it at a level where the CEP appears explicitly. From a more distanced perspective, the CEP affects the symmetry properties of the pulses and thus of the combined field. Numerical evaluations have motivated the conjecture that two different laser fields being described by different shape functions $f(\eta)$ and $g(\eta)$ give rise to the same fully differential probabilities, when the shape functions fulfill the relation $f'(-\eta) = -g'(\eta)$. We recall that these derivatives of the shape functions are proportional to the electric and magnetic fields. One may speculate that this conjecture can be proven by employing the CPT invariance of QED. A similar relation was also found in [LLX+14]. Applying this approach to the combined field $f = f_1 + f_2$, the fully differential probabilities can thus be expected to be invariant under the exchange of the order of the pulses, if the shape functions f_j of both individual pulses fulfill $f_j'(-\eta) = -f_j'(\eta)$. For our family of shape functions, this condition is only fulfilled for $\chi = 0$ and $\chi = \pi$. Finally, we note that pulses with $\chi = \pi/2$ and $\chi = 3\pi/2$ are related via this symmetry, i.e. they induce the same pair-production probabilities. This is compatible with the interference phase

$\cos((N - N')\chi)$ which was introduced in the context of the multiphoton-CEP effects in Chapter 4.
When we integrate the angular distributions over the positron momentum, the influence of the temporal ordering is weaker than for the fully differential probabilities, but still visible. We present the original case of pulses A and B (with $\chi_A = \chi_B = 0$) in Fig. 6.10, and for $\chi_B = \pi/2$ in Fig. 6.11. Comparing the contributions of pulse B, the CEP has only a marginal influence on the integrated angular distribution here. Also the distributions obtained in the combined field appear qualitatively similar in all cases, yet clear quantitative differences exist.

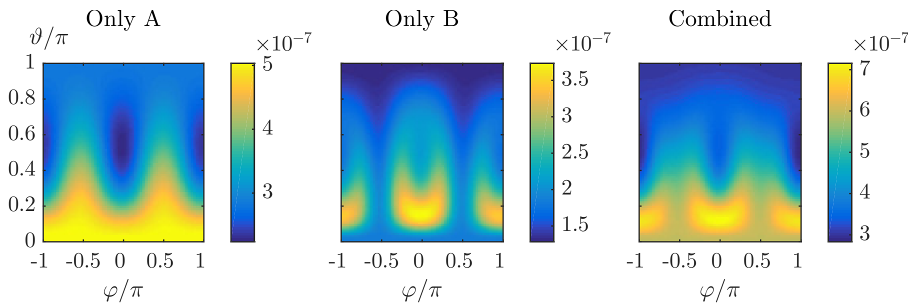

Figure 6.10: Momentum integrated angular distributions $\frac{d^2\mathscr{P}}{d^2\Omega_{p_+}}$ for the same parameters as in Fig. 6.7, i.e. $\chi_A = \chi_B = 0$, and $D = 0$.

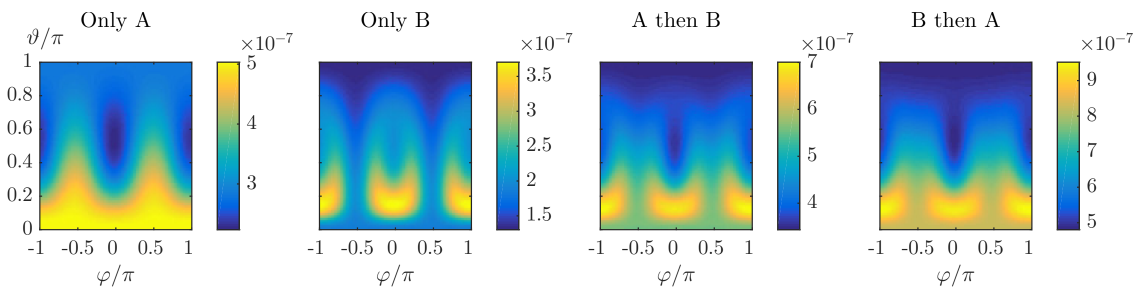

Figure 6.11: Same as Fig. 6.10, except $\chi_B = \pi/2$.

Again, the gap width D has a distinct influence. The combined distributions for $D = 3\lambda_e$ are depicted in Fig. 6.12. In comparison with $D = 0$ (see third and fourth panel of Fig. 6.11), the effect of the temporal ordering almost appears to be inverted.

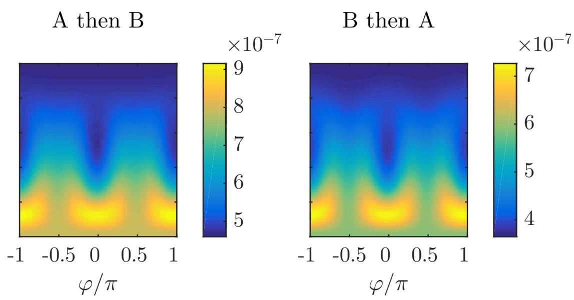

Figure 6.12: Same as Fig. 6.11, except $D = 3\lambda_e$.

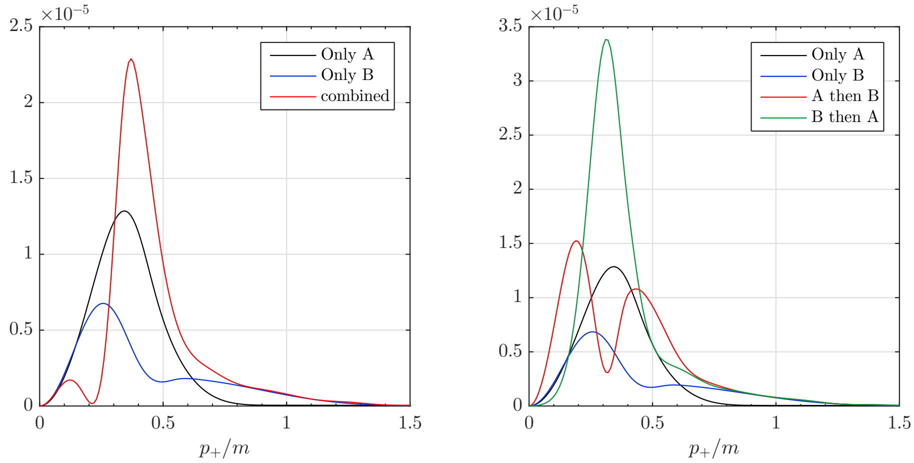

Figure 6.13: Momentum spectra $\frac{d\mathscr{P}}{dp_+}$ (in units of $1/m$) for the pulses A and B with $D = 0$. The left panel depicts the situation when $\chi_A = \chi_B = 0$. In the right panel, the CEP of pulse B is changed according to $\chi_B = \pi/2$.

6.3.2.2 Momentum spectra

In Fig. 6.13, we inspect the momentum spectra $\frac{d\mathscr{P}}{dp_+}$ for the pulses A and B in the case when $\chi_A = \chi_B = 0$ (left) and for $\chi_B = \pi/2$ (right). Again, the CEP plays only a minor role for the individual contribution of pulse B, but the momentum spectra obtained in the combined fields exhibit pronounced differences. When $\chi_A = \chi_B = 0$, the combined momentum spectrum possesses a sharply peaked maximum at $p_+ \approx 0.37m$. When $\chi_B = \pi/2$, the momentum spectrum deeply depends on the temporal order of the pulses. When pulse B arrives first, a sharp maximum is located at $p_+ \approx 0.31m$, where the probability is significantly higher than the maximum value obtained with $\chi_B = 0$. In contrast, when pulse A arrives first, the momentum spectrum has a pronounced minimum at $p_+ \approx 0.32m$.

6.3.2.3 Total probability

Finally, we regard the total probabilities and in particular the influence of the distance D between the pulses. In Fig. 6.14, we present the total probabilities obtained in the combined field of the pulses A and B, normalized to the sum of the individual probabilities. We begin with $\chi = 0$ for both pulses, where the individual probabilities amount to $\mathscr{P}_A \approx 4.1 \times 10^{-6}$ and $\mathscr{P}_B \approx 2.6 \times 10^{-6}$. As depicted in the left panel of Fig. 6.14, the combined probability exhibits a damped oscillatory behavior as the pulse distance grows. For small distances, pronounced interference effects enhance or decrease the total probability by up to 20% in comparison with the direct summation of the individual probabilities. When the pulse distance grows, these interference effects soon become smaller. Overall, the behavior closely resembles the case of two identical pulses, as depicted for example in Fig. 6.5, where a different normalization was employed. In principle, the interferences are in both cases subject to a similar mechanism. As a major difference, the interference terms arising from the non-identical pulses are not only determined by the phase ϕ, but also by the complex values of the contributions F_j of the individual pulses [see, e.g., Eq. (6.33)].
Next, we change the CEP of pulse B according to $\chi_B = \pi/2$. As expected from the momentum spectra in Fig. 6.13, the corresponding probability is only mildly affected and now amounts to $\mathscr{P}_B \approx 2.7 \times 10^{-6}$. With the symmetry of the combined field being partially

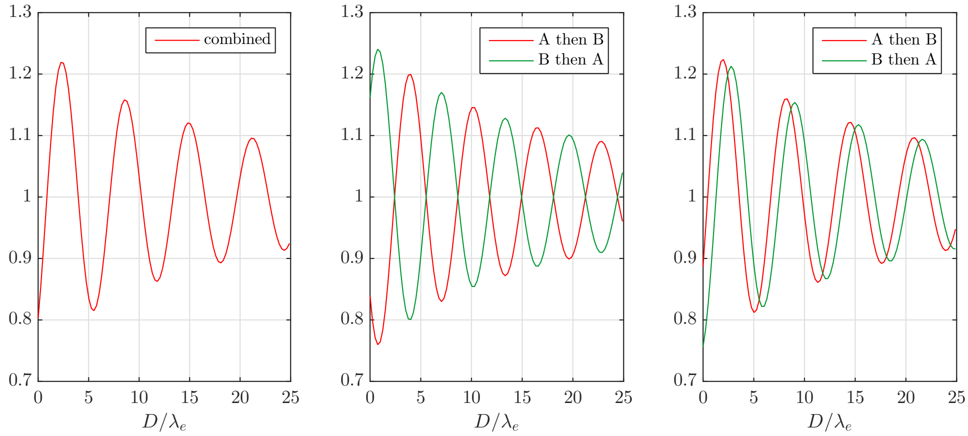

Figure 6.14: The plots show the probabilities obtained in the combined fields of the pulses A and B as a function of the pulse distance, normalized by the sum of the individual probabilities. Left: $\chi_A = \chi_B = 0$. Center: $\chi_A = 0$ and $\chi_B = \pi/2$. Right: $\chi_A = \pi/3$ and $\chi_B = \pi/5$.

broken, the resulting probability is now sensitive to the temporal order of the pulses. The normalized probabilities are depicted for the two nonequivalent field configurations in the center panel of Fig. 6.14. For both configurations, the dependence on the pulse distance exhibits qualitatively similar behavior as in the symmetric case. Most strikingly, the total probabilities obtained in the two different configurations appear to be offset by a phase of π and we find

$$\frac{1}{2}\left[\mathscr{P}_{AB}(D) + \mathscr{P}_{BA}(D)\right] \approx \mathscr{P}_A + \mathscr{P}_B \tag{6.47}$$

for any given pulse distance D. Upon close inspection, we find that an analogous relation holds (approximately) for the momentum-integrated angular distributions (see Figs. 6.11 and 6.12) and for the momentum spectra[5] (see right panel of Fig. 6.13), but it does not hold for the fully differential probabilities (see Fig. 6.8). These findings imply that at least one integration is required for a relation of the type as in Eq. (6.47).

We emphasize that this relation arises due to the special choices of the CEP. When $\chi_A = \chi_B = 0$, it does not hold, as can be seen from the left panels of Figs. 6.13 and 6.14. Finally we present the total probabilities for $\chi_A = \pi/3$ and $\chi_B = \pi/5$ in the right panel of Fig. 6.14, with $\mathscr{P}_A \approx 4.4 \times 10^{-6}$ and $\mathscr{P}_B \approx 2.6 \times 10^{-6}$. Equation (6.47) is not fulfilled, since the total probabilities obtained in the two nonequivalent field configurations are offset by a relatively small phase.

6.4 Conclusion

In this chapter, we have extended the laser field by a second short pulse which arrives with a variable delay. Assuming the pulses to arrive strictly after each other, the S-matrix approach allows us to separate the process amplitude into contributions from the individual pulses. The combined process is subject to pronounced interferences between these contributions, which can either suppress the differential probability completely or enhance it by a factor of four in the case of two identical pulses. The interference phase depends on the absorbed photon energy and on the interpulse distance. When the total probability

[5]For higher momenta, the accuracy decreases, even when the angular resolution is increased.

is regarded, the interference phases tend to cancel due to the underlying integration over different absorbed energies. However, when the pulse distance is on the order of the pulse length or smaller, distinct interference effects remain visible.

We have addressed the question to which extent the order of the two pulses affects the process. The answer to that question was found to be determined by the CEP of the pulses. In particular, for certain (special) constellations of the CEP χ, the process is invariant under the exchange of the order of the pulses, even with regard to the fully differential probabilities. In contrast, for (most) other choices of χ, the process is sensitive to the order. The differences were traced back to the symmetry properties of the laser fields. From a classical viewpoint, and also with regard to pump-probe experiments, the sensitivity to the temporal order seems natural and satisfies the expectation. However, this property can be affected by changing the continuous parameter χ. Hence, instead of a two-stage process, the SFBW process induced by these consecutive pulses can rather be understood as one single process driven by the combined field composed of the individual pulses. The two pulses act like two (asymmetrically structured) slits in a double-slit experiment. Similar interpretations of the pair-creation process induced by pulse trains can also be found in [HIM10, KK14]. One may ask what happens when the gamma quantum is restricted to a finite temporal extent as well. In the present scenario, the gamma quantum is infinitely extended, such that it interacts with both pulses simultaneously, which is the key explanation to our findings. The temporal ordering of the laser pulses presumably becomes even more relevant when the gamma quantum is described as a wave packet with a well-defined beginning. Furthermore, the role of the interference effects may be determined by the temporal extent of this wave packet, which could either be longer or much shorter than the laser pulses and the gap distance.

Regarding the two pulses as the constituents of a combined field, the results presented in this chapter further emphasize the strong sensitivity of the process to the properties of the driving field.

With regard to an experimental observation of Schwinger-like pair production via dynamical assistance [SGD08], we conclude that the two pulses need to arrive simultaneously in order to enhance the probability by reducing the tunneling distance. This can also be deduced from Fig. 5 in [LLX$^+$14]. We note that the case of two simultaneously arriving laser pulses could also be computed in our framework by using the Volkov states for the combined field. This way, the individual contributions cannot necessarily be separated analytically, but the integrals can (at least in principle) be evaluated numerically.

7 | Conclusion

We have studied in detail the SFBW process induced by short laser pulses of medium intensity. With regard to the influence of the properties of the laser pulses, particular emphasis has been placed on the spectral properties, the CEP, and the pulse duration. In the regime of moderate intensities, the SFBW process in a (short) pulse can be understood in terms of multiphoton processes being induced by individual photons stemming from the pulse. This approach has been incorporated into a new quantitative model, which has provided important analytical support for this work.

Our results show that the process is very sensitive to the properties of the driving laser field. Furthermore, for example the focusing of a short pulse was recently found to affect the SFBW probabilities substantially [DP16]. Consequently, the angular distributions obtained in experiments may differ strongly from the theoretical predictions unless exactly the same pulse shape is employed. Hence, rather than aiming at actual predictions for experimental measurements, our work enhances the fundamental understanding of the process. In addition, we note that the process under investigation is closely related to other laser-induced strong-field (QED) processes, such as multiphoton Compton scattering. Some of the insights found in this work, in particular related to the multiphoton approach, can therefore be applied to these processes, as well.

Owing to its quantum nature, the SFBW process is subject to interference effects, which have been studied in detail, in particular with respect to the question how they are affected by the broad spectrum inherent to a short pulse. The spectra of the produced particles were found to exhibit clear signatures of interference effects, even when short pulses are employed. In addition to the interferences between production channels comprising different photon combinations, our investigation of a double-pulse scenario shows that interferences also arise between processes which originate from different parts of the driving laser field. This latter approach can in particular be applied in order to reproduce the particle spectra in the regime of $\xi_{\max} \gg 1$, as has been shown in [MKDP16]. These subpulse interferences and the multiphoton interferences are two complementary approaches to the interference processes. In both cases, the interferences can be controlled by the CEP. This way, the optical phase (CEP) offers a means to control the quantum phase of the SFBW process.

We have seen that the SFBW process exhibits a non-trivial dependence on the spin of the particles. The underlying behavior could be understood to some extent by regarding the angular-momentum balance, but the details remain elusive. The spin plays a fundamental role, which should be taken into account for theoretical calculations aiming at precise predictions.

With regard to an experimental observation of the SFBW process under investigation, we note that the requirements concerning the optical laser ($\sim 10^{18}$ W/cm^2) are well within reach of contemporary facilities. In contrast, the generation of the high-frequency photon with $\sim$ 100 GeV is more challenging. These photons could be generated by Compton backscattering off an ultrarelativistic electron beam, which could be created by a conventional accelerator (like SLAC), possibly in combination with a subsequent laser-plasma-based accelerator [BCD$^+$07]. A similar scheme is currently under development at XCELS. In order to observe the effect with less energetic photons, the coherent radiation may be obtained from an X-ray free-electron laser with a substantially higher central frequency. Employing 0.2 keV as provided by SASE3 at DESY, the required intensity is 10^{21} W/cm^2,

which is about one order of magnitude beyond the performance goals formulated in the year 2002 [DES]. In addition, the original x-ray pulse needs to be shortened, which could be achieved by various methods [SSY04, Tan15, PR15]. This way, the required photon energy is substantially reduced and amounts to 4 GeV for the parameters employed in the first example of Chap. 3. These energies are accessible via state-of-the art laser-plasma based accelerators [LNG$^+$06]. Both approaches to the SFBW process are technologically challenging and require, among others, very powerful laser systems on the PW scale, such as the Diocles laser (US) [Dio], or the laser system planned for ELI-NP (Rumania).
We finally note that also the original Breit-Wheeler process, which comprises only two highly energetic photons, attracts significant attention with regard to a refined experimental observation [PMHR14, RdJ$^+$16], even in the general media.[1]
Turning light into matter is a fascinating prospect. The process itself is accompanied by a multitude of physical phenomena which are still waiting for experimental observation and further theoretical investigation. In view of the latest technological developments, one may hope for dedicated experiments in the near future.

[1]See, e.g., `http://www.bbc.com/news/science-environment-27470034`, and `http://www.faz.net/aktuell/wissen/physik-mehr/quantenverwandlung-es-werde-das-licht-zur-materie-12969264.html`.

A Appendix

A.1 Classical motion of a charged particle in a laser field

For this calculation, which is adapted from [IZ85], we assume the vector potential to be given in the form

$$A^\mu(\eta) = f(\eta)\epsilon^\mu \tag{A.1}$$

where ϵ^μ is a real polarization vector with $\epsilon^2 = -1$ and $k \cdot \epsilon = 0$.
The dynamics of a particle with mass m and charge $-e$ are governed by the equation of motion

$$m\frac{du^\mu}{d\tau} = -eF^\mu{}_\nu u^\nu \tag{A.2}$$

with the particle's four velocity $u^\mu = dx^\mu/d\tau$ and proper time τ. The right-hand side is determined by the field-strength tensor $F^{\mu\nu} = (k^\mu\epsilon^\nu - k^\nu\epsilon^\mu)f'(\eta)$.
Since $k^2 = 0$ and hence $k_\mu F^\mu{}_\nu = 0$, multiplying Eq. (A.2) with k_μ reveals the first constant of motion $k \cdot u(\tau) = k \cdot u(0) = \text{const.}$ Consequently, the phase variable η can be expressed as a linear function of τ. For simplicity, we assume the particle to be initially at the origin, allowing us to write $\eta = k \cdot u(0)\tau$ and to bring Eq. (A.2) into the form

$$\frac{du^\mu}{d\eta} = -\frac{e}{m}\left(\frac{\epsilon \cdot u(\eta)}{k \cdot u(0)}k^\mu - \epsilon^\mu\right) f'(\eta)\,. \tag{A.3}$$

Multiplying by ϵ_μ and integrating yields

$$\epsilon \cdot u(\eta) = \epsilon \cdot u(0) - \frac{e}{m}\left[f(\eta) - f(0)\right] \tag{A.4}$$

which can be inserted in Eq. (A.3)

$$\frac{du^\mu}{d\eta} = -\frac{e}{m}\left(\frac{k^\mu}{k \cdot u(0)}\left[\epsilon \cdot u(0) - \frac{e}{m}\left[f(\eta) - f(0)\right]\right] - \epsilon^\mu\right) f'(\eta)\,. \tag{A.5}$$

With the right-hand side of this equation being independent of $u(\eta)$, it can directly be integrated and yields

$$u^\mu(\eta) = u^\mu(0) - \frac{e}{m}\left[f(\eta) - f(0)\right]\left(\frac{\epsilon \cdot u(0)}{k \cdot u(0)}k^\mu - \epsilon^\mu\right) + \frac{e^2}{2m^2}\left[f(\eta) - f(0)\right]^2\frac{k^\mu}{k \cdot u(0)}\,. \tag{A.6}$$

Assuming the laser field to be of finite extent, with $f(0) = 0$, the kinetical momentum $p^\mu(\eta) = mu^\mu(\eta)$ of the particle in the laser field can be expressed as

$$p^\mu(\eta) = p_0^\mu + eA^\mu(\eta) - \left(ep_0 \cdot A(\eta) + \frac{e^2}{2}A^2(\eta)\right)\frac{k^\mu}{k \cdot p_0} \tag{A.7}$$

where p_0^μ denotes the particle's initial four momentum.

A.2 Dirac γ matrices

The following section contains some helpful details of the Dirac γ matrices.
The γ matrices are defined by the anti-commutation relation

$$\gamma^\mu \gamma^\nu + \gamma^\nu \gamma^\mu = 2g^{\mu\nu}\mathbb{I}_4 \tag{A.8}$$

with the metric tensor $g^{\mu\nu} = \mathrm{diag}(1, -1, -1, -1)$ and with $\mathbb{I}_N$ denoting the $N \times N$ unit matrix. Employing the Pauli σ matrices

$$\sigma_1 = \begin{pmatrix} 0 & 1 \\ 1 & 0 \end{pmatrix}, \quad \sigma_2 = \begin{pmatrix} 0 & -i \\ i & 0 \end{pmatrix}, \quad \sigma_3 = \begin{pmatrix} 1 & 0 \\ 0 & -1 \end{pmatrix}, \tag{A.9}$$

the Dirac γ matrices can be represented in the form

$$\gamma^0 = \begin{pmatrix} \mathbb{I}_2 & 0 \\ 0 & -\mathbb{I}_2 \end{pmatrix}, \quad \gamma^k = \begin{pmatrix} 0 & \sigma_k \\ -\sigma_k & 0 \end{pmatrix}. \tag{A.10}$$

The γ matrices fulfill the properties

$$\begin{aligned} (\gamma^0)^2 &= 1\,, \quad (\gamma^0)^\dagger = \gamma^0 \\ (\gamma^k)^2 &= -1\,, \quad (\gamma^k)^\dagger = -\gamma^k\,. \end{aligned} \tag{A.11}$$

We employ Feynman slash notation to indicate four-products between the gamma matrices and a four vector a^μ

$$\not{a} = a_\mu \gamma^\mu \tag{A.12}$$

Products of slashed quantities can be reordered via

$$\not{a}\not{b} = a_\mu b_\nu \gamma^\mu \gamma^\nu = a_\mu b_\nu (2g^{\mu\nu} - \gamma^\nu \gamma^\mu) = 2a \cdot b - \not{b}\not{a} \tag{A.13}$$

where a^μ and b^ν are assumed to be composed of complex numbers. In particular, this implies $\not{k}\not{k} = k \cdot k = 0$ for a wave four-vector $k^\mu = (|\mathbf{k}|, \mathbf{k})$.
It is furthermore convenient to employ the Dirac adjoint, which is defined for a four-spinor w via

$$\overline{w} = w^\dagger \gamma^0 \tag{A.14}$$

and for an operator acting on the spinors via

$$\overline{\not{a}} = \gamma^0 (\not{a})^\dagger \gamma^0\,. \tag{A.15}$$

The γ matrices are invariant under the Dirac adjoint $\overline{\gamma^\mu} = \gamma^\mu$.
Properties concerning the traces are presented in App. A.4.2.

A.3 Spinors

In the following, we will present the spinors employed in the Dirac-Volkov states and revisit their properties [Gre00, Gre03]. In particular, we will show how the spinor products occurring in the S-matrices can be evaluated analytically by means of the trace technique.
The Dirac-Volkov states Eq.(2.9) are solutions of the full Dirac equation Eq.(2.8), when the spinors $w_{p_\pm s_\pm}$ are solutions of the free Dirac equation

$$\left(i\not{\partial} - m\right) \Psi_r(\mathbf{p}) = 0 \tag{A.16}$$

with a wave function $\Psi_r(\mathbf{p})$ of the form

$$\Psi_r(p) = e^{-i\varepsilon_r p\cdot x} w_r(\mathbf{p}) \tag{A.17}$$

with $p^\mu = (E_p, \mathbf{p})$, $E_p = \sqrt{m^2+\mathbf{p}^2}$ and a spinor $w_r(\mathbf{p})$. The index r distinguishes different states, which shall be classified below. We define $\varepsilon_r = +1$ for $r = 1, 2$, and $\varepsilon_r = -1$ for $r = 3, 4$. This sign affects the energy $\varepsilon_r E_p$ and the canonical momentum $\varepsilon_r \mathbf{p}$.
Inserting this ansatz into the Dirac equation yields the algebraic equation

$$\left(\varepsilon_r \not{p} - m\right) w_r(\mathbf{p}) = 0\,. \tag{A.18}$$

It is fulfilled by the following spinors $w_r(\mathbf{p})$ which are presented in the r'th column of the matrix

$$\sqrt{\frac{E_p+m}{2m}}\left[\begin{pmatrix} 1 \\ 0 \\ \frac{p_z}{E_p+m} \\ \frac{p_x+ip_y y}{E_p+m}\end{pmatrix}, \begin{pmatrix} 0 \\ 1 \\ \frac{p_x-ip_y}{E_p+m} \\ \frac{-p_z}{E_p+m}\end{pmatrix}, \begin{pmatrix} \frac{p_z}{E_p+m} \\ \frac{p_x+ip_y}{E_p+m} \\ 1 \\ 0\end{pmatrix}, \begin{pmatrix} \frac{p_x-ip_y}{E_p+m} \\ \frac{-p_z}{E_p+m} \\ 0 \\ 1\end{pmatrix}\right]. \tag{A.19}$$

For $\mathbf{p} \to p_z \mathbf{e}_z$, these are Eigenspinors of the spin operator $\frac{1}{2}\Sigma_z = \frac{1}{2}\begin{pmatrix}\sigma_z & 0 \\ 0 & \sigma_z\end{pmatrix}$, with Eigenvalues $+\frac{1}{2}$ for $r = 1, 3$ and $-\frac{1}{2}$ for $r = 2, 4$.
They are normalized according to

$$w_r^\dagger(\mathbf{p}) w_r(\mathbf{p}) = \frac{E_p}{m} \tag{A.20}$$

and fulfill the closure relation

$$\sum_{r=1}^{4} \varepsilon_r w_\alpha^r(\mathbf{p}) \overline{w}_\beta^r(\mathbf{p}) = \delta_{\alpha\beta}\,, \tag{A.21}$$

which is needed for the trace technique presented in the following.
The orthogonality can be expressed as

$$\overline{w}^r(\mathbf{p}) w^{r'}(\mathbf{p}) = \delta_{rr'}\varepsilon_r\,, \quad w_r^\dagger(\varepsilon_r\mathbf{p}) w_{r'}(\varepsilon_{r'}\mathbf{p}) = \delta_{rr'}\frac{E_p}{m}\,. \tag{A.22}$$

The spinors $w_r(p)$ with $r = 3, 4$ describe electrons with negative energy $-E_p$ and canonical momentum $-\mathbf{p}$, which serve as initial states for our treatment of the pair-production process. When an electron has left this state, this empty state corresponds to a positron with energy $+E_p$ and momentum $+\mathbf{p}$. Furthermore, also the spin projection is inverted, which can formally be seen when a charge conjugation is applied. Therefore, we define the spinors $w_{p_\pm s_\pm}$ employed in the Dirac-Volkov states as

$$\begin{aligned} w_{p_-,+1/2} &= w_1(\mathbf{p}_-)\,, \\ w_{p_-,-1/2} &= w_2(\mathbf{p}_-)\,, \\ w_{p_+,+1/2} &= w_4(\mathbf{p}_+)\,, \\ w_{p_+,-1/2} &= w_3(\mathbf{p}_+)\,. \end{aligned} \tag{A.23}$$

A.4 Trace technique

In this appendix, we first revisit the trace technique [Gre03], which allows to express spin-summed matrix elements independent of the actual representation of the spinors. We begin with a presentation of the general concept, which is then refined and explicitly applied to our calculation of the pair-production probability in a single pulse.
In order to increase the readability of the following section, we introduce the notation $u(p_-, s_-) = w_{p_- s_-}$ and $v(p_+, s_+) = w_{p_+ s_+}$ for the spinors introduced in App. A.3. Furthermore, we denote four-products in the form $a \cdot b = (ab)$.

A.4.1 General concept

When we regard the spin-summed pair-production probability, we have to look at expressions of the form

$$\begin{aligned}\mathcal{M}(p_+, p_-) &= \sum_{s_+, s_-} |\overline{u}(p_-, s_-)\Gamma\, v(p_+, s_+)|^2 \\ &= \sum_{s_+, s_-} \overline{u}(p_-, s_-)\Gamma\, v(p_+, s_+)\overline{v}(p_+, s_+)\overline{\Gamma}\, u(p_-, s_-)\end{aligned} \tag{A.24}$$

with a general matrix Γ acting on the spinors.
In order to treat this expression analytically, it is helpful to define energy projection operators

$$\Lambda_\pm(p) = \frac{\pm \not{p} + m}{2m} \tag{A.25}$$

which are sensitive to the sign of the energy, i.e.

$$\begin{aligned}&\Lambda_+(p)u(p, s) = u(p, s) \\ &\Lambda_-(p)v(p, s) = v(p, s) \\ &\Lambda_+(p)v(p, s) = 0 = \Lambda_-(p)u(p, s)\,.\end{aligned} \tag{A.26}$$

The expression $\mathcal{M}(p_+, p_-)$ contains the matrix $\sum_{s_+} v(p_+, s_+)\overline{v}(p_+, s_+)$, which will be regarded first. Dropping the explicit momentum dependence (each spinor and the projection operator is evaluated at p_+), the α, β entry of this matrix can be written as

$$\begin{aligned}\sum_{s_+} v_\alpha(p_+, s_+)\overline{v}_\beta(p_+, s_+) &= \sum_{r=3}^{4} w^r_\alpha \overline{w}^r_\beta = \sum_{r=1}^{4} (\Lambda_+ w^r)_\alpha\, \overline{w}^r_\beta = -\sum_{r=1}^{4} \varepsilon_r\, (\Lambda_+ w^r)_\alpha\, \overline{w}^r_\beta \\ &= -\sum_\gamma (\Lambda_+)_{\alpha\gamma} \sum_{r=1}^{4} \varepsilon_r w^r_\gamma \overline{w}^r_\beta = -\sum_\gamma (\Lambda_+)_{\alpha\gamma}\, \delta_{\gamma\beta} = \left(\frac{\not{p}_+ - m}{2m}\right)_{\alpha\beta}\end{aligned} \tag{A.27}$$

where the closure relation Eq.(A.21) has been used in the second-to-last step. Effectively, the spinors have thus been eliminated.
The analogue expression for the electronic spinors reads

$$\sum_{s_-} u_\alpha(p_-, s_-)\overline{u}_\beta(p_-, s_-) = \left(\frac{\not{p}_- + m}{2m}\right)_{\alpha\beta}\,. \tag{A.28}$$

Temporarily abbreviating $u \equiv u(p_-, s_-)$ and $v \equiv v(p_+, s_+)$, the matrix element $\mathcal{M}(p_+, p_-)$ can finally be rewritten as

$$\begin{aligned}\mathcal{M}(p_+, p_-) &= \sum_{s_+, s_-} \overline{u}\,\Gamma\, v\, \overline{v}\,\overline{\Gamma}\, u = \sum_{s_-} \overline{u}\,\Gamma \left(\frac{\not{p}_+ - m}{2m}\right) \overline{\Gamma}\, u \\ &= \sum_{s_-} \sum_{\alpha\beta} \overline{u}_\alpha \left(\Gamma \left(\frac{\not{p}_+ - m}{2m}\right) \overline{\Gamma}\right)_{\alpha\beta} u_\beta = \sum_{\alpha\beta} \left(\Gamma \left(\frac{\not{p}_+ - m}{2m}\right) \overline{\Gamma}\right)_{\alpha\beta} \sum_{s_-} u_\beta \overline{u}_\alpha \\ &= \sum_{\alpha\beta} \left(\Gamma \left(\frac{\not{p}_+ - m}{2m}\right) \overline{\Gamma}\right)_{\alpha\beta} \left(\frac{\not{p}_- + m}{2m}\right)_{\beta\alpha} = \mathrm{Tr}\left[\Gamma \left(\frac{\not{p}_+ - m}{2m}\right) \overline{\Gamma} \left(\frac{\not{p}_- + m}{2m}\right)\right].\end{aligned} \tag{A.29}$$

Accordingly, traces over products of γ matrices have to be evaluated.

A.4.2 Traces over products of γ matrices

Several helpful properties are [Gre03]

1. The γ matrices have vanishing trace
$$\mathrm{Tr}(\gamma^\mu) = 0\,. \tag{A.30}$$
2. However, for a product of two γ matrices, the trace reads
$$\mathrm{Tr}(\not{a}\not{b}) = 4(ab)\,. \tag{A.31}$$
3. Products comprising several gamma matrices can be iteratively reduced via
$$\begin{aligned}\mathrm{Tr}(\not{a}_1 \dots \not{a}_n) = &(a_1 a_2)\,\mathrm{Tr}(\not{a}_3 \dots \not{a}_n) - (a_1 a_3)\,\mathrm{Tr}(\not{a}_2 \not{a}_4 \dots \not{a}_n) + \\ &+ \dots + (a_1 a_n)\,\mathrm{Tr}(\not{a}_2 \dots \not{a}_{n-1})\,.\end{aligned} \tag{A.32}$$
As a consequence, the trace of a product of an uneven number of gamma matrices vanishes.
4. The order of products can be inverted
$$\mathrm{Tr}(\not{a}_1 \dots \not{a}_n) = \mathrm{Tr}(\not{a}_n \dots \not{a}_1)\,. \tag{A.33}$$

A.4.3 Refinement

When the matrix operator Γ is composed of various terms $\Gamma = \sum_j \Gamma_j$ containing different products of γ matrices, the following refinement is helpful. For $\mathcal{M}(p_+, p_-) = \sum_{i,j} \mathcal{M}_{ij}(p_+, p_-)$, we can write

$$\begin{aligned}\mathcal{M}_{ij}(p_+, p_-) &= \sum_{s_+, s_-} \overline{u}(p_-, s_-)\Gamma_i\, v(p_+, s_+)\, [\overline{u}(p_-, s_-)\Gamma_j\, v(p_+, s_+)]^* \\ &= \sum_{s_+, s_-} \overline{u}(p_-, s_-)\Gamma_i\, v(p_+, s_+) \overline{v}(p_+, s_+) \overline{\Gamma}_j\, u(p_-, s_-) \\ &= \mathrm{Tr}\left[\Gamma_i \left(\frac{\not{p}_+ - m}{2m}\right) \overline{\Gamma}_j \left(\frac{\not{p}_- + m}{2m}\right)\right] \equiv \mathrm{Tr}\,(\Gamma_i, \Gamma_j)\end{aligned} \tag{A.34}$$

in close analogy to the steps presented in Eq. (A.29). Note that $\mathrm{Tr}\,(\Gamma_i, \Gamma_j)^* = \mathrm{Tr}\,(\Gamma_j, \Gamma_i)$. Furthermore, when the γ matrices are multiplied with purely real four-vectors, like in our case, the resulting traces are entirely real, allowing us to drop the complex conjugation and thus to interchange the order of the arguments.

A.4.4 Explicit application to our calculation

Starting from Eq.(2.58), the trace technique has to be applied to

$$\mathfrak{M} = \sum_{s_+,s_-} \left|\tilde{\mathfrak{b}} I_1 + \tilde{\mathfrak{c}} I_2\right|^2 . \tag{A.35}$$

With $\tilde{\mathfrak{b}}$ and $\tilde{\mathfrak{c}}$ being usual complex numbers, the expression can be written as

$$\mathfrak{M} = |I_1|^2 \Bigg(\sum_{s_+,s_-} \tilde{\mathfrak{b}}\tilde{\mathfrak{b}}^* \Bigg) + 2\Re \left[I_1 I_2^* \Bigg(\sum_{s_+,s_-} \tilde{\mathfrak{b}}\tilde{\mathfrak{c}}^* \Bigg) \right] + |I_2|^2 \Bigg(\sum_{s_+,s_-} \tilde{\mathfrak{c}}\tilde{\mathfrak{c}}^* \Bigg) . \tag{A.36}$$

We inspect $\tilde{\mathfrak{b}}$ as defined in Eq. (2.50) and introduce abbreviations in order to separate the slashed quantities in the form

$$\begin{aligned} \tilde{\mathfrak{b}} &= \mathfrak{b} - \frac{k^0}{Q^0} h_1 \mathfrak{a} \\ &= \overline{w}_{p_- s_-} \Bigg[\underbrace{-\frac{eA_0}{2c(kp_-)}}_{=:m_-} \not\epsilon \not k \not\epsilon_\gamma + \underbrace{\frac{eA_0}{2c(kp_+)}}_{=:m_+} \not\epsilon_\gamma \not k \not\epsilon \underbrace{- \frac{k^0}{Q^0} h_1}_{=:m_1} \not\epsilon_\gamma \Bigg] w_{p_+ s_+} . \end{aligned} \tag{A.37}$$

This sum contains two products of three γ matrices, which can be combined by rewriting the central term via

$$\not\epsilon_\gamma \not k \not\epsilon = - \not\epsilon \not k \not\epsilon_\gamma - 2 \not k (\epsilon_\gamma \epsilon) , \tag{A.38}$$

which leads to

$$\tilde{\mathfrak{b}} = \overline{w}_{p_- s_-} \Bigg[\underbrace{(m_- - m_+)}_{=:m_3} \not\epsilon \not k \not\epsilon_\gamma \underbrace{-2m_+(\epsilon_\gamma \epsilon)}_{=:m_k} \not k + m_1 \not\epsilon_\gamma \Bigg] w_{p_+ s_+} . \tag{A.39}$$

Conversely, $\tilde{\mathfrak{c}}$ can straight-forwardly be structured as

$$\tilde{\mathfrak{c}} = -\frac{k^0}{Q^0} h_2 \mathfrak{a} = \overline{w}_{p_- s_-} \Bigg[\underbrace{-\frac{k^0}{Q^0} h_2}_{=:m_2} \not\epsilon_\gamma \Bigg] w_{p_+ s_+} . \tag{A.40}$$

Employing the refined trace technique [see Eq. (A.34)], we can approach the terms in Eq. (A.36). We begin with the last term, which has the simplest structure. We obtain

$$\sum_{s_+,s_-} \tilde{\mathfrak{c}}\tilde{\mathfrak{c}}^* = |m_2|^2 \operatorname{Tr} \left[\not\epsilon_\gamma \left(\frac{\not p_+ - m}{2m} \right) \overline{\not\epsilon_\gamma} \left(\frac{\not p_- + m}{2m} \right) \right] = |m_2|^2 \operatorname{Tr}(\not\epsilon_\gamma, \not\epsilon_\gamma) . \tag{A.41}$$

For the central term, we regard

$$\begin{aligned} \sum_{s_+,s_-} \tilde{\mathfrak{c}}\tilde{\mathfrak{b}}^* =& \operatorname{Tr} \left[m_2 \not\epsilon_\gamma \left(\frac{\not p_+ - m}{2m} \right) \left(m_3^* \overline{\not\epsilon \not k \not\epsilon_\gamma} + m_k^* \overline{\not k} + m_1^* \overline{\not\epsilon_\gamma} \right) \left(\frac{\not p_- + m}{2m} \right) \right] \\ =& m_2 m_3^* \operatorname{Tr}(\not\epsilon_\gamma, \not\epsilon \not k \not\epsilon_\gamma) + m_2 m_k^* \operatorname{Tr}(\not\epsilon_\gamma, \not k) + m_2 m_1^* \operatorname{Tr}(\not\epsilon_\gamma, \not\epsilon_\gamma) , \end{aligned} \tag{A.42}$$

since $\tilde{\mathfrak{b}}\tilde{\mathfrak{c}}^* = \left(\tilde{\mathfrak{c}}\tilde{\mathfrak{b}}^*\right)^*$. Furthermore, note that all values $m_{\ldots}$ are real, as well as the traces. Accordingly, we drop the complex conjugation for the remaining term, which reads

$$\begin{aligned} \sum_{s_+,s_-} \tilde{\mathfrak{b}}\tilde{\mathfrak{b}}^* =& |m_3|^2 \operatorname{Tr}(\not\epsilon \not k \not\epsilon_\gamma, \not\epsilon \not k \not\epsilon_\gamma) + |m_k|^2 \operatorname{Tr}(\not k, \not k) + |m_1|^2 \operatorname{Tr}(\not\epsilon_\gamma, \not\epsilon_\gamma) \\ &+ 2m_3 m_k \operatorname{Tr}(\not\epsilon \not k \not\epsilon_\gamma, \not k) + 2m_3 m_1 \operatorname{Tr}(\not\epsilon \not k \not\epsilon_\gamma, \not\epsilon_\gamma) + 2m_k m_1 \operatorname{Tr}(\not k, \not\epsilon_\gamma) . \end{aligned} \tag{A.43}$$

The traces are presented in the following section.

A.4.5 Explicit traces

In our calculation, we need the following traces, which can be evaluated using the properties presented in App. A.4.2

$$\mathrm{Tr}(\not{\epsilon}_\gamma, \not{\epsilon}_\gamma) = \frac{1}{m^2}\left[2(\epsilon_\gamma p_+)(\epsilon_\gamma p_-) + (p_+ p_-) + m^2\right] \tag{A.44}$$

$$\mathrm{Tr}(\not{\epsilon}_\gamma, \not{\epsilon}\not{k}\not{\epsilon}_\gamma) = \frac{1}{(2m)^2}\left[-8(kp_-)(\epsilon\epsilon_\gamma)(p_+\epsilon_\gamma) - 4(kp_-)(\epsilon p_+) + 4(kp_+)(\epsilon p_-)\right] \tag{A.45}$$

$$\mathrm{Tr}(\not{\epsilon}_\gamma, \not{k}) = \frac{1}{(2m)^2}\left[4(kp_-)(\epsilon_\gamma p_+) + 4(kp_+)(\epsilon_\gamma p_-)\right] \tag{A.46}$$

$$\mathrm{Tr}(\not{\epsilon}\not{k}\not{\epsilon}_\gamma, \not{\epsilon}\not{k}\not{\epsilon}_\gamma) = \frac{1}{(2m)^2}\left[8(kp_+)(kp_-)\right] \tag{A.47}$$

$$\mathrm{Tr}(\not{k}, \not{k}) = \frac{1}{(2m)^2}\left[8(kp_+)(kp_-)\right] \tag{A.48}$$

$$\mathrm{Tr}(\not{\epsilon}\not{k}\not{\epsilon}_\gamma, \not{k}) = \frac{1}{(2m)^2}\left[-8(kp_+)(kp_-)(\epsilon\epsilon_\gamma)\right] \tag{A.49}$$

A.5 Dealing with squares of δ functions

When transition amplitudes are calculated in a plane-wave basis, the space-time integration yields δ functions. The corresponding probability is then obtained as the absolute square of this expression. In this context, the question arises how to treat squares of δ functions.

We first present the usual treatment, followed by an illustration of the problems arising when coordinate transformations are involved. As a next step, we present our first attempt to treat the squares of δ functions being formulated in light-cone coordinates. This approach, however, includes a subtle shortcoming, which shall be illustrated. The issue is finally resolved in App. A.5.4 by treating the incoming gamma quantum as a wave packet.

A.5.1 Standard treatment

The standard treatment can be summarized as follows: Starting with

$$2\pi\delta(k) = \int_{-\infty}^{\infty} dx\, e^{ikx} \tag{A.50}$$

the original integration domain is understood to be limited to a finite extent L, motivating to replace

$$2\pi\delta(k) \to \int_{-L/2}^{L/2} dx\, e^{ikx} = \frac{2}{k}\sin(kL/2)\,. \tag{A.51}$$

This way, the integral of a square of δ functions can readily be assigned the value

$$\int_{-\infty}^{\infty} dk\, [2\pi\delta(k)]^2 \to \int_{-\infty}^{\infty} dk \left[\frac{2}{k}\sin(kL/2)\right] = 2\pi L\,. \tag{A.52}$$

Furthermore, from Eq. (A.51), we can deduce

$$2\pi\delta(k=0) \to L\,. \tag{A.53}$$

Accordingly, the expression for the probability containing $\delta(k)^2$ and an arbitrary function $f(k)$ is usually treated as

$$\int_{-\infty}^{\infty} dk\,[2\pi\delta(k)]^2\, f(k) = 2\pi\;[2\pi\delta(k=0)]\,f(k=0) \to 2\pi L\, f(0)\,. \tag{A.54}$$

A.5.2 Coordinate transforms

When a coordinate transform is involved, the above treatment has to applied with great care, as shall be demonstrated in the following. As a general rule, δ functions with their argument being given by a function $g(k)$ can be recast according to

$$\delta\,[g(k)] = \sum_{k_0} \frac{1}{|g'(k)|}\delta(k-k_0) \tag{A.55}$$

for $g'(k_0) \neq 0$, where k_0 is iterated through the simple zeros of $g(k)$.
Let us introduce a real number $a > 0$ and regard

$$\int_{-\infty}^{\infty} d(ak)\,[2\pi\delta(k)]^2 = a\int_{-\infty}^{\infty} dk\,[2\pi\delta(k)]^2 \to 2\pi a\, L \tag{A.56}$$

according to Eq. (A.52). Here, L is the extent of the integration domain which has led to $\delta(k)$. Likewise, we may follow a different procedure by employing Eq. (A.55), which yields $2\pi\delta(k) = 2\pi a\,\delta(ak)$. Accordingly, we obtain

$$\begin{aligned}\int_{-\infty}^{\infty} d(ak)\,[2\pi\delta(k)]^2 = \int_{-\infty}^{\infty} d(ak)\,[2\pi a\,\delta(ak)]^2 &= a^2\int_{-\infty}^{\infty} d(ak)\,[2\pi\delta(ak)]^2 \\ &= 2\pi a^2\;[2\pi\delta(ak=0)]\end{aligned} \tag{A.57}$$

where the comparison with Eq. (A.56) shows that $2\pi\delta(ak=0) = L/a$. Hence, when squares of δ functions have to be evaluated, it is crucial to know the original integration domain.
In our case of a finite laser pulse, the δ functions naturally arise in light-cone coordinates, such that the corresponding volume factors have to be determined carefully.

A.5.3 A first attempt

Inspecting the S-matrix element, the square of the δ functions needs to be compensated by the normalization factor V of the incoming gamma quantum, where V denotes a usual Cartesian normalization volume. While the transverse δ functions are expressed in Cartesian coordinates, we have to find the correct volume factor associated with $\delta(Q^-)$. As a first attempt, we restrict the integration along $x^\|$ to the finite range $L^\|$, i.e. the longitudinal extent of the normalization volume V. Likewise, also the interaction time is restricted to a finite duration. This way, the partial integration applied in the Boca-Florescu transform can initially be carried out without the explicit need for a damping. Regarding the (unrestricted) integrals along x^+ and x^-, one obtains

$$\begin{aligned}2\pi\delta(Q^-)I_0 \equiv &\frac{e^{iQ^-L_l^\|} - e^{-iQ^-L_u^\|}}{iQ^-}\frac{-k^0}{Q^0}\int_0^{2\pi/k^0} dx^- h(k^0x^-)e^{-iH(k^0x^-)-iQ^0x-} + \\ &+\frac{e^{iQ^\|L_u^\|} - e^{-iQ^\|L_l^\|}}{iQ^\|}\frac{e^{iQ^0L_l^0} - e^{-iQ^0L_u^0-iH(2\pi)}}{iQ^0}\end{aligned} \tag{A.58}$$

where I_0 was introduced in Eq. (2.23), and $L_l^{\parallel}$ and $L_u^{\parallel}$ describe the lower and upper limits, respectively, of the integration domain along $x^{\parallel}$. Similarly, the temporal extent is given by $L_u^0 - L_l^0$.

The second line corresponds to the surface term which vanishes due to the damping included in our version of the Boca-Florescu transformation. Here, we may also argue that in the limit[1] of a large volume, the first factor of the second line restricts $Q^{\parallel} = 0$. In combination with $\mathbf{Q}^{\perp} = 0$, this condition can be ruled out from a kinematical consideration.

The first factor of the remaining first line is easily recognized as $2\pi\delta(Q^-)$, while the second factor is already familiar from the Boca-Florescu transform. With the volume factors at hand, one feels tempted to conclude that $2\pi\delta(Q^- = 0) \to L^{\parallel} = L_u^{\parallel} - L_l^{\parallel}$.

However, this conclusion turns out to be wrong. This approach (seems to) overestimate the interaction time, i.e. the time in which the laser pulse actually interacts with the gamma quantum. With the laser pulse being truly limited to a short finite duration, the interaction time is only $L^{\parallel}/2$.

In order to obtain a more straightforward derivation, it is helpful to treat the gamma quantum as a wave packet. This way, squares of light-cone δ functions can be avoided, and we can apply the usual treatment.

A.5.4 Treating the gamma quantum as a wave packet

In the context of Breit-Wheeler pair production, a similar procedure was first presented in [MHKDP15]. We present our own version.

We describe the gamma quantum as a wave packet with a continuous distribution of momentum components along the beam axis $\eta(\kappa^{\parallel})$, allowing us to express the effective scattering potential in the form

$$\mathcal{A}_\gamma^\mu = \sqrt{\frac{2\pi}{V\omega_\gamma}} \int d\kappa^{\parallel}\, \eta(\kappa^{\parallel}) e^{-i\kappa\cdot x} \epsilon_\gamma^\mu \tag{A.59}$$

with $\kappa^\mu = (|\kappa^{\parallel}|, 0, 0, \kappa^{\parallel})$. For the pair-production process, we need $\kappa^{\parallel} < 0$.

This way, with the only difference being the presence of the wave-packet function $\eta(\kappa^{\parallel})$ and the modified momentum vector κ^μ, starting from Eq. (2.21), the S matrix can be expressed as

$$\mathcal{S}_{p_+p_-} = \int d\kappa^{\parallel}\, \eta(\kappa^{\parallel}) \mathcal{S}(\kappa^{\parallel}) \tag{A.60}$$

with

$$\mathcal{S}(\kappa^{\parallel}) = (2\pi)^3 S_0\, \delta(R^-) \delta^{(2)}(\mathbf{P}^{\perp}) I(\kappa^{\parallel}) \tag{A.61}$$

where the former momentum vector Q^μ is replaced by $R^\mu = \kappa^\mu - P^\mu$, with $P^\mu = p_+^\mu + p_-^\mu$. Furthermore, we have $I(\kappa^{\parallel}) = \int dx^- C(k^0 x^-) e^{-iR^0 x^- - iH(k^0 x^-)}$. The latter depends on $\kappa^{\parallel}$ only via R^0.

The integration along $\kappa^{\parallel}$ can be used to eliminate $\delta(R^-)$, inducing a factor

$$\left| \frac{d\kappa^-}{d\kappa^{\parallel}} \right|^{-1} = \left(\frac{\kappa^-}{\kappa^0} \right)^{-1} > 0\,. \tag{A.62}$$

Since $\kappa^- = -2\kappa^{\parallel} > 0$, the condition $R^- = 0$ leads to $\kappa^{\parallel} = -P^-/2$.

---

[1] To be precise, expression Eq.(A.58) was derived under the assumptions $L_u^0 > L_u^{\parallel} + 2\pi/k^0$ and $L_l^0 > L_l^{\parallel}$. However, also in this approach we could introduce a damping factor, such that the surface terms strictly disappear.

The S-matrix element thus reads

$$\mathcal{S}_{p_+p_-} = (2\pi)^3 S_0 \, \frac{\kappa^0}{\kappa^-} \delta^{(2)}(\mathbf{P}^\perp)\eta(\kappa^\|)I(\kappa^\|)\bigg|_{\kappa^\|=-P^-/2} . \tag{A.63}$$

The absolute square of the S matrix shall now be obtained from this expression[2].
As a next step, we contract the wave packet via

$$\eta(\kappa^\|) = \delta(\kappa^\| - k_\gamma^\|) \, . \tag{A.64}$$

This δ function, as well as $\delta^{(2)}(\mathbf{P}^\perp)$, is based on usual Cartesian coordinates. Thus, with regard to the absolute square, we deduce

$$|2\pi\delta(\kappa^\| - k_\gamma^\|)|^2 = 2\pi L^\| \, \delta(\kappa^\| - k_\gamma^\|) \tag{A.65}$$

where $L^\|$ is the longitudinal extent of the normalization volume V. The latter was introduced in Eq. (A.59) and is now included in the prefactor $S_0 \sim 1/\sqrt{V}$. Similarly, we have

$$|(2\pi)^2\delta^{(2)}(\mathbf{P}^\perp)|^2 = (2\pi)^2 V^\perp \, \delta^{(2)}(\mathbf{P}^\perp) \, , \tag{A.66}$$

where $V^\perp$ is the perpendicular extent of the normalization volume, such that $V = L^\| V^\perp$. This way, the square of the S-matrix amplitude reads

$$|\mathcal{S}_{p_+p_-}|^2 = |S_0|^2 \left(\frac{\kappa^0}{\kappa^-}\right)^2 (2\pi)^3\delta(\kappa^\| - k_\gamma^\|)\delta^{(2)}(\mathbf{P}^\perp) \, |I(\kappa^\|)|^2 V \bigg|_{\kappa^\|=-P^-/2} . \tag{A.67}$$

After the contraction, we have $I(k_\gamma^\|) = I$ from Eq. (2.22), $R^\mu = Q^\mu$ and $k_\gamma^0/k_\gamma^- = 1/2$. Finally, the δ functions are expressed in the original form, such that one factor of $1/2$ is absorbed into $\delta(Q^-)$, yielding

$$|\mathcal{S}_{p_+p_-}|^2 = \frac{1}{2} \, |S_0|^2 \, (2\pi)^3\delta(Q^-)\delta^{(2)}(\mathbf{Q}^\perp)|I|^2 \, V \, . \tag{A.68}$$

This way, the squares have been resolved, and we can derive the prescription

$$(2\pi)^3\delta(Q^- = 0)\delta^{(2)}(\mathbf{Q}^\perp = 0) \to \frac{k_\gamma^0}{k_\gamma^-} V \, . \tag{A.69}$$

We note that the scale factor $k_\gamma^0/k_\gamma^- = 1/2$ gives the ratio between the interaction time and the temporal extent of the gamma quantum.
In the context of Compton scattering, an analogous procedure can be applied, where the incoming electron is treated as a wave packet and determines the scaling factor [IT13]. The resulting expression was shown to reproduce the classical limit in [Mac14], which provided an important argument in favor of the wave-packet approach and indicated a shortcoming in our first attempt.

[2] The treatment presented in [MHKDP15] follows a slightly different approach by regarding the two amplitudes (which are multiplied in order to obtain the probability) simultaneously. This way, one arrives at $|\mathcal{S}_{p_+p_-}|^2 \sim 2\pi \int d\kappa^\| \, |\eta(\kappa^\|)|^2 \, \frac{\kappa^0}{\kappa^-}(2\pi)^3|S_0|^2 \, \delta(R^-)\delta^{(2)}(\mathbf{P}^\perp)|I(\kappa^\|)|^2$. In principle, we could have followed a similar procedure, yet the resulting expression additionally contains $V^\perp$ [see Eq.(A.66)] due to our definition of the wave packet. Our wave packet is introduced with smallest possible deviation from the original calculation, aiming at an early contraction.

A.6 Properties of the pulse shape

In the following, we briefly review the properties of the pulse shape used for our numerical examples, which reads (cp. Eq. (2.11))

$$f'(\eta) = \sin^2(\eta/2)\sin(N_{\text{osc}}\eta + \chi)\,. \tag{A.70}$$

Using trigonometric identities, it can directly be written as a Fourier series

$$\begin{aligned} f'(\eta) &= \frac{1}{2}\sin(N_{\text{osc}}\eta + \chi) - \frac{1}{4}\sin([N_{\text{osc}} - 1]\eta + \chi) - \frac{1}{4}\sin([N_{\text{osc}} + 1]\eta + \chi) \\ &= \sum_{n=N_{\text{osc}}-1}^{N_{\text{osc}}+1} a'_n \sin(n\eta + \chi) \end{aligned} \tag{A.71}$$

with $a'_n = 1/2$ for $n = N_{\text{osc}}$, and $a'_n = -1/4$ for $n = N_{\text{osc}} \pm 1$.
We note that this way, the vector potential being proportional to $f(\eta)$ can easily be determined analytically. Similarly, also $f(\eta)^2$, which appears in the Volkov phases, can be expressed as a Fourier series comprising generally ten terms (and one constant term). Accordingly, the Volkov states can be expanded into a product of about ten ordinary Bessel functions, see App. A.7. However, this approach is numerically much more expensive than a direct integration of the corresponding integrals comprising the Volkov phases.
With regard to the electric field associated with f', we have to account for the characteristic function $\mathcal{X}_{[0,2\pi]}(\eta)$. Accordingly, the Fourier transform of the electric field is of the form

$$\begin{aligned} \widehat{f'\mathcal{X}_{[0,2\pi]}}(\nu) &= \sum_{n=N_{\text{osc}}-1}^{N_{\text{osc}}+1} a'_n \int_0^{2\pi/\omega_b} \sin(n\omega_b t + \chi) e^{i\nu t} dt \\ &= \frac{1}{2i\omega_b} \sum_{n=N_{\text{osc}}-1}^{N_{\text{osc}}+1} a'_n \left[e^{i\chi} I_n(\nu/\omega_b) - e^{-i\chi} I_{-n}(\nu/\omega_b) \right] \,, \end{aligned} \tag{A.72}$$

with

$$I_n(x) = \int_0^{2\pi} e^{i(x+n)\phi} d\phi = \frac{e^{2\pi i x} - 1}{i(x+n)} = 2e^{i\pi x}\frac{\sin(\pi x)}{x+n}\,. \tag{A.73}$$

We note that these integrals are crucially determined by the characteristic function, which is used in order to model the finite length of the pulse. As a first and most important effect, the finite extent of the integration domain broadens the spectral peaks induced by $f'(\eta)$. Nevertheless, we see that I_n vanishes for integer values of x except $x = -n$. These zeros remain in the Fourier transform of the electric field [see Eq. (A.72) and Eq. (A.74) below] at most integer values of ν/ω_b except $\pm\nu/\omega_b \in \{N_{\text{osc}}, N_{\text{osc}} \pm 1\}$ and determine the appearance of the one-photon-finding probability, which is depicted in Fig. 3.1.
The spectral phase discussed in Chap. 4 is introduced at the level of the vector potential, which is proportional to $f(\eta)$. Since $f'(\eta) = \frac{1}{\omega_b}\frac{d}{dt}f(\eta)$, the Fourier transforms are related according to $\hat{f}'(\nu) = -\frac{i\nu}{\omega_b}\hat{f}(\nu)$. The corresponding spectral phases are the same except for an overall offset, such that it is sufficient to regard the spectral phase induced by $\hat{f}'(\nu)$.
To this end, we abbreviate $x = \nu/\omega_b$ and simplify the Fourier transform of the electric field [see Eq. (A.72)] according to

$$\widehat{f'\mathcal{X}_{[0,2\pi]}} = \frac{e^{i\pi x}}{i\omega_b}\sin(\pi x)\sum_{n=N_{\text{osc}}-1}^{N_{\text{osc}}+1} a'_n \left(\frac{e^{i\chi}}{x+n} - \frac{e^{-i\chi}}{x-n} \right)\,. \tag{A.74}$$

For high energies with $x > N_{\mathrm{osc}}+1$, the zeros induced by $\sin(\pi x)$ are accompanied by phase jumps of π, which induce the characteristic behavior of the interference terms involving one high-energy photon. Conversely, in the central peak where $\nu/\omega_b \in (N_{\mathrm{osc}}-2, N_{\mathrm{osc}}+2)$, the zeros of $\sin(\pi x)$ are compensated by one of the $1/(x-n)$ terms, and the phase remains continuous.[3] Furthermore, as discussed in Sec. 4.1, for energies within the central peak, we may neglect the terms with $1/(x+n)$. Hence, we can deduce that the spectral phase approximately scales as $-\chi + \pi\nu/\omega_b$. We note that the frequency-dependent term is irrelevant for the interference phase, since it is compensated by the analogous term from the interference partner. In fact, as mentioned in Sec. 4.1, one can simplify the analysis of the interference phase by transforming the pulse into a time interval which is symmetric about $t = 0$. This way, the continuous frequency dependence induced by $e^{i\pi x}$ vanishes directly:
We briefly sketch the procedure required to transform the pulse into the interval $[-\pi, \pi]$. Introducing $\phi = \eta - \pi$, the shape function reads

$$f'(\phi) = \sum_{n=N_{\mathrm{osc}}-1}^{N_{\mathrm{osc}}+1} a'_n \sin(n\phi + n\pi + \chi)\,. \tag{A.75}$$

Now we can proceed in close analogy to the above treatment, except that the integral in $I_n(x)$ extents from $-\pi$ to π and temporarily contains the additional phase term $e^{in\pi}$, yielding

$$I_n(x) = e^{in\pi}\int_{-\pi}^{\pi} e^{i(x+n)\phi} d\phi = 2\frac{\sin(x\pi)}{(x+n)}\,, \tag{A.76}$$

which is more compact than the prior version of I_n in Eq. (A.73). This way, we arrive at the original expression in Eq. (A.74) but without the factor $e^{i\pi x}$.

A.7 Fourier expanding the integrals

Employing the notation introduced in Chap. 6 for a double pulse, we separate oscillatory and growing terms in $H_j(\Phi_j)$ [see Eq. (6.24)] via

$$H_j = \underbrace{\sum_{l=1}^{2} h_{lj}\int_0^{\Phi_j}\left(f_j^l(\eta) - \langle f_j^l\rangle\right) d\eta}_{=:G_j} + \Phi_j \underbrace{\sum_{l=1}^{2} h_{lj}\langle f_j^l\rangle}_{=:\mu_j} \tag{A.77}$$

with the phase average

$$\langle f_j^l\rangle = \frac{1}{2\pi}\int_0^{2\pi} f_j^l(\eta) d\eta\,. \tag{A.78}$$

This way, G_j can be regarded as a periodic function in Φ_j, with period length 2π. As can be seen from Eq. (6.20), the same holds for $\tilde{C}_j$. As a consequence, $\tilde{C}_j e^{-iG_j}$ can be expanded into a Fourier series. Bringing the shape function into the form of Eq. (A.71), the key step is to replace each harmonic term in the exponent by employing the Jacobi-Anger expansion [AS72]

$$e^{iz\sin(\theta)} = \sum_{n=-\infty}^{\infty} J_n(z) e^{in\theta}\,, \tag{A.79}$$

[3] We note, however, that the relation between the coefficients a'_n has to be taken into consideration in order to show that no further zeros (with corresponding phase jumps) are induced by the summation.

where the $J_n(z)$ denote ordinary Bessel functions.
Following this path, one can derive the expansion coefficients $D_j(n_j)$ and arrives at the form

$$\tilde{C}_j e^{-iG_j} = \sum_{n_j=-\infty}^{\infty} D_j(n_j) e^{in_j\Phi_j} \,. \tag{A.80}$$

Accordingly, the integrand of F_j from Eq. (6.26) can be written as

$$\sum_{l=1}^{2} \tilde{g}_{lj} f_j^l(\Phi_j) e^{-i(Q^0\Phi_j/k_j^0 + G_j + \Phi_j\mu_j)} = \sum_{n_j=-\infty}^{\infty} D_j(n_j) e^{-i(Q^0+\mu_j k_j^0 - n_j k_j^0)\,\Phi_j/k_j^0} \,. \tag{A.81}$$

Despite the suggestive form of Eq. (A.81), one should keep in mind that the integration is restricted to $\Phi_j \in [0, 2\pi]$. Accordingly, the exponent does not deliver a fourth δ function. In particular, the numbers n_j should be treated with care. They cannot be interpreted as the number of absorbed photons with frequency k_j^0.
The term $\mu_j k_j^0$ describes the dressing of the particle states due to the interaction with the j-th laser pulse, with $\mu_j = -w_j$, where w was introduced for a single pulse in Eq. (2.39), see also Sec. 6.2.2. We note that this Fourier expansion can be applied to the case of a single pulse, too.

Bibliography

[AB65] A. I. Akhiezer and V. B. Berestetskii: *Quantum Electrodynamics*, 2nd ed. (John Wiley & Sons, New York, 1965).

[AD12] E. Akkermans and G. V. Dunne: *Ramsey Fringes and Time-Domain Multiple-Slit Interference from Vacuum*, Phys. Rev. Lett. **108**, 030401 (2012).

[AM13] S. Augustin and C. Müller: *Interference effects in Bethe-Heitler pair creation in a bichromatic laser field*, Phys. Rev. A **88**, 022109 (2013).

[AS72] M. Abramowitz and I.A. Stegun: *Handbook of Mathematical Functions with Formulas, Graphs, and Mathematical Tables*, 10th ed. (National Bureau of Standards, Washington D.C., 1972).

[AVCM14] I. Akal, S. Villalba-Chávez, and C. Müller: *Electron-positron pair production in a bifrequent oscillating electric field*, Phys. Rev. D **90**, 113004 (2014).

[BCD+07] I. Blumenfeld, C. E. Clayton, F.-J. Decker, M. J. Hogan, C. Huang, R. Ischebeck, R. Iverson, C. Joshi, T. Katsouleas, N. Kirby, W. Lu, K. A. Marsh, W. B. Mori, P. Muggli, E. Oz, R. H. Siemann, D. Walz, and M. Zhou: *Energy doubling of 42 GeV electrons in a metre-scale plasma wakefield accelerator*, Nature **445**, 741 (2007).

[BF09] M. Boca and V. Florescu: *Nonlinear Compton scattering with a laser pulse*, Phys. Rev. A **80**, 053403 (2009).

[BF10] M. Boca and V. Florescu: *The Completeness of Volkov Spinors*, Rom. Journ. Phys. **55**, 511 (2010).

[BFHS+97] D. L. Burke, R. C. Field, G. Horton-Smith, J. E. Spencer, D. Walz, S. C. Berridge, W. M. Bugg, K. Shmakov, A. W. Weidemann, C. Bula, K. T. McDonald, E. J. Prebys, C. Bamber, S. J. Boege, T. Koffas, T. Kotseroglou, A. C. Melissinos, D. D. Meyerhofer, D. A. Reis, and W. Ragg: *Positron Production in Multiphoton Light-by-Light Scattering*, Phys. Rev. Lett. **79**, 1626 (1997).

[BLP80] W. B. Berestetzki, E. M. Lifschitz, and L. P. Pitajewski: *Relativistische Quantentheorie*, 4., bearb. Aufl. (Akademie Verlag, Berlin, 1980).

[Boc11] M. Boca: *On the properties of the Volkov solutions of the Klein-Gordon equation*, J. Phys. A: Math. Theor. **44**, 445303 (2011).

[BV80] J. Bergou and S. Varro: *Wavefunctions of a free electron in an external field and their application in intense field interactions. II. Relativistic treatment*, J. Phys. A **13**, 2823 (1980).

[BV81] J. Bergou and S. Varro: *Nonlinear scattering processes in the presence of a quantised radiation field. II. Relativistic treatment*, J. Phys. A **14**, 2281 (1981).

[BW34] G. Breit and J. A. Wheeler: *Collision of Two Light Quanta*, Phys. Rev. **46**, 1087 (1934).

[DD10] C. K. Dumlu and G. V. Dunne: *Stokes Phenomenon and Schwinger Vacuum Pair Production in Time-Dependent Laser Pulses*, Phys. Rev. Lett. **104**, 250402 (2010).

[DD11] C. K. Dumlu and G. V. Dunne: *Interference effects in Schwinger vacuum pair production for time-dependent laser pulses*, Phys. Rev. D **83**, 065028 (2011).

[DES] For current information, see http://xfel.desy.de.

[Dio] See http://unlcms.unl.edu/physics-astronomy/fuchs-group/research.

[DP16] A. Di Piazza: *Nonlinear Breit-Wheeler Pair Production in a Tightly Focused Laser Beam*, Phys. Rev. Lett. **117**, 213201 (2016).

[DPMHK12] A. Di Piazza, C. Müller, K. Z. Hatsagortsyan, and C. H. Keitel: *Extremely high-intensity laser interactions with fundamental quantum systems*, Rev. Mod. Phys. **84**, 1177 (2012).

[EKK09] F. Ehlotzky, K. Krajewska, and J. Z. Kamiński: *Fundamental processes of quantum electrodynamics in laser fields of relativistic power*, Rep. Prog. Phys. **72**, 046401 (2009).

[ELI] For current information, see https://eli-laser.eu.

[Gib96] P. Gibbon: *Harmonic Generation by Femtosecond Laser-Solid Interaction: A Coherent "Water-Window" Light Source?*, Phys. Rev. Lett. **76**, 50 (1996).

[Gre00] W. Greiner: *Relativistic Quantum Mechanics. Wave Equations*, 3rd ed. (Springer, Berlin, 2000).

[Gre03] W. Greiner: *Quantum Electrodynamics*, 3rd ed. (Springer, Berlin, 2003).

[GT16] F. Gelis and N. Tanji: *Schwinger mechanism revisited*, Prog. Part. Nucl. Phys. **87**, 1 (2016).

[HADG09] F. Hebenstreit, R. Alkofer, G. V. Dunne, and H. Gies: *Momentum Signatures for Schwinger Pair Production in Short Laser Pulses with a Subcycle Structure*, Phys. Rev. Lett. **102**, 150404 (2009).

[HE36] W. Heisenberg and H. Euler: *Folgerungen aus der Diracschen Theorie des Positrons*, Z. Phys. **98**, 714 (1936).

[Hib] For current information, see http://www.hibef.eu.

[HIM10] T. Heinzl, A. Ilderton, and M. Marklund: *Finite size effects in stimulated laser pair production*, Phys. Lett. B **692**, 250 (2010).

[HMK10] H. Hu, C. Müller, and C. H. Keitel: *Complete QED Theory of Multiphoton Trident Pair Production in Strong Laser Fields*, Phys. Rev. Lett. **105**, 080401 (2010).

[IKS05] D. Yu. Ivanov, G. L. Kotkin, and V. G. Serbo: *Complete description of polarization effects in e^+e^- pair production by a photon in the field of a strong laser wave*, Eur. Phys. J. C (2005) **40**, 27 (2005).

[IT13] A. Ilderton and G. Torgrimsson: *Scattering in plane-wave backgrounds: Infrared effects and pole structure*, Phys. Rev. D **87**, 085040 (2013).

[IZ85] C. Itzykson and J.-B. Zuber: *Quantum Field Theory*, 1st ed. (McGraw-Hill Book Co., Singapore, 1985).

[Jan13] M. Jansen: *Elektron-Positron-Paarerzeugung in zweifarbigen Laserfeldern*, Master's thesis, Heinrich-Heine-Universität Düsseldorf, 2013.

[JKKM16] M. J. A. Jansen, J. Z. Kamiński, K. Krajewska, and C. Müller: *Strong-field Breit-Wheeler pair production in short laser pulses: Relevance of spin effects*, Phys. Rev. D **94**, 013010 (2016).

[JM13] M. J. A. Jansen and C. Müller: *Strongly enhanced pair production in combined high- and low-frequency laser fields*, Phys. Rev. A **88**, 052125 (2013).

[JM15] M. J. A. Jansen and C. Müller: *Pair Creation of Scalar Particles in Intense Bichromatic Laser Fields*, J. Phys. Conf. Ser. **594**, 012051 (2015).

[JM16a] M. J. A. Jansen and C. Müller: *Strong-field Breit-Wheeler pair production in short laser pulses: Identifying multiphoton interference and carrier-envelope-phase effects*, Phys. Rev. D **93**, 053011 (2016).

[JM16b] M. J. A. Jansen and C. Müller: *Strong-Field Breit-Wheeler Pair Production in Two Consecutive Laser Pulses with Variable Time Delay*, arXiv:1612.07137 (2016). This article was published in Phys. Lett. B **766**, 71 (2017).

[JSL+12] M. Jiang, W. Su, Z. Q. Lv, X. Lu, Y. J. Li, R. Grobe, and Q. Su: *Pair creation enhancement due to combined external fields*, Phys. Rev. A **85**, 033408 (2012).

[KGA14] C. Kohlfürst, H. Gies, and R. Alkofer: *Effective Mass Signatures in Multiphoton Pair Production*, Phys. Rev. Lett. **112**, 050402 (2014).

[KK12a] K. Krajewska and J. Z. Kamiński: *Breit-Wheeler process in intense short laser pulses*, Phys. Rev. A **86**, 052104 (2012).

[KK12b] K. Krajewska and J. Z. Kamiński: *Compton process in intense short laser pulses*, Phys. Rev. A **85**, 062102 (2012).

[KK12c] K. Krajewska and J. Z. Kamiński: *Phase effects in laser-induced electron-positron pair creation*, Phys. Rev. A **85**, 043404 (2012).

[KK14] K. Krajewska and J. Z. Kamiński: *Coherent combs of antimatter from nonlinear electron-positron-pair creation*, Phys. Rev. A **90**, 052108 (2014).

[KMvW+13] C. Kohlfürst, M. Mitter, G. von Winckel, F. Hebenstreit, and R. Alkofer: *Optimizing the pulse shape for Schwinger pair production*, Phys. Rev. D **88**, 045028 (2013).

[KTK14] K. Krajewska, M. Twardy, and J. Z. Kamiński: *Global phase and frequency comb structures in nonlinear Compton and Thomson scattering*, Phys. Rev. A **89**, 052123 (2014).

[LLX+14] Z. L. Li, D. Lu, B. S. Xie, L. B. Fu, J. Liu, and B. F. Shen: *Enhanced pair production in strong fields by multiple-slit interference effect with dynamically assisted Schwinger mechanism*, Phys. Rev. D **89**, 093011 (2014).

[LNG+06] W. P. Leemans, B. Nagler, A. J. Gonsalves, Cs. Toth, K. Nakamura, C. G. R. Geddes, E. Esarey, C. B. Schroeder, and S. M. Hooker: *GeV electron beams from a centimetre-scale accelerator*, Nature Physics **2**, 696 (2006).

[Mac14] K. F. Mackenroth: *Quantum Radiation in Ultra-Intense Laser Pulses*, Springer International Publishing, 2014.

[MHKDP15] S. Meuren, K. Z. Hatsagortsyan, C. H. Keitel, and A. Di Piazza: *Polarization-operator approach to pair creation in short laser pulses*, Phys. Rev. D **91**, 013009 (2015).

[MKDP16] S. Meuren, C. H. Keitel, and A. Di Piazza: *Semiclassical picture for electron-positron photoproduction in strong laser fields*, Phys. Rev. D **93**, 085028 (2016).

[NF00] N. B. Narozhny and M. S. Fofanov: *Quantum processes in a two-mode laser field*, J. Exp. Theor. Phys. **90**, 415 (2000).

[NNR65] N. B. Narozhny, A. I. Nikishov, and V. I. Ritus: *Quantum Processes in the Field of a Circularly Polarized Electromagnetic Wave*, Sov. Phys. JETP **20**, 622 (1965).

[NR64a] A. I. Nikishov and V. I. Ritus: *Quantum Processes in the Field of a Plane Electromagnetic Wave and in a Constant Field. I*, Sov. Phys. JETP **19**, 529 (1964).

[NR64b] A. I. Nikishov and V. I. Ritus: *Quantum Processes in the Field of a Plane Electromagnetic Wave and in a Constant Field*, Sov. Phys. JETP **19**, 1191 (1964).

[NR67] A. I. Nikishov and V. I. Ritus: *Pair Production by a Photon and Photon Emission by an Electron in the Field of an Intense Electromagnetic Wave and in a Constant Field*, Sov. Phys. JETP **25**, 1135 (1967).

[NSKT12] T. Nousch, D. Seipt, B. Kämpfer, and A. I. Titov: *Pair production in short laser pulses near threshold*, Phys. Lett. B **715**, 246 (2012).

[PMHR14] O. J. Pike, F. Mackenroth, E. G. Hill, and S. J. Rose: *A photon-photon collider in a vacuum hohlraum*, Nature Photonics **8**, 434 (2014).

[PR15] E. Prat and S. Reiche: *Simple Method to Generate Terawatt-Attosecond X-Ray Free-Electron-Laser Pulses*, Phys. Rev. Lett. **114**, 244801 (2015).

[RadBB+12] C. Rödel, D. an der Brügge, J. Bierbach, M. Yeung, T. Hahn, B. Dromey, S. Herzer, S. Fuchs, A. Galestian Pour, E. Eckner, M. Behmke, M. Cerchez, O. Jäckel, D. Hemmers, T. Toncian, M. C. Kaluza, A. Belyanin, G. Pretzler,

O. Willi, A. Pukhov, M. Zepf, and G. G. Paulus: *Harmonic Generation from Relativistic Plasma Surfaces in Ultrasteep Plasma Density Gradients*, Phys. Rev. Lett. **109**, 125002 (2012).

[RdJ+16] X. Ribeyre, E. d'Humières, O. Jansen, S. Jequier, V. T. Tikhonchuk, and M. Lobet: *Pair creation in collision of γ-ray beams produced with high-intensity lasers*, Phys. Rev. E **93**, 013201 (2016).

[Rei62] H. R. Reiss: *Absorption of Light by Light*, J. Math. Phys. (N.Y.) **3**, 59 (1962).

[Rei80] H. R. Reiss: *Effect of an intense electromagnetic field on a weakly bound system*, Phys. Rev. A **22**, 1786 (1980).

[Rei09] H. R. Reiss: *Special analytical properties of ultrastrong coherent fields*, Eur. Phys. J. D **55**, 365 (2009).

[Rit85] V. I. Ritus: *Quantum effects of the interaction of elementary particles with an intense electromagnetic field*, J. Sov. Laser Res. **6**, 497 (1985).

[Sau31] F. Sauter: *Über das Verhalten eines Elektrons im homogenen elektrischen Feld nach der relativistischen Theorie Diracs*, Z. Phys. **69**, 742 (1931).

[Sch51] J. Schwinger: *On Gauge Invariance and Vacuum Polarization*, Phys. Rev. **82**, 664 (1951).

[SGD08] R. Schützhold, H. Gies, and G. Dunne: *Dynamically Assisted Schwinger Mechanism*, Phys. Rev. Lett. **101**, 130404 (2008).

[SHMB16] D. Seipt, T. Heinzl, M. Marklund, and S. S. Bulanov: *Depletion of intense fields*, arXiv:1605.00633 (2016).

[SSY04] E. L. Saldin, E. A. Schneidmiller, and M. V. Yurkov: *A new technique to generate 100 GW-level attosecond X-ray pulses from the X-ray SASE FELs*, Opt. Commun. **239**, 161 (2004).

[Tan15] T. Tanaka: *Proposal to Generate an Isolated Monocycle X-Ray Pulse by Counteracting the Slippage Effect in Free-Electron Lasers*, Phys. Rev. Lett. **114**, 044801 (2015).

[TTKH12] A. I. Titov, H. Takabe, B. Kämpfer, and A. Hosaka: *Enhanced Subthreshold e^+e^- Production in Short Laser Pulses*, Phys. Rev. Lett. **108**, 240406 (2012).

[VCM13] S. Villalba-Chávez and C. Müller: *Photo-production of scalar particles in the field of a circularly polarized laser beam*, Phys. Lett. B **718**, 992 (2013).

[Wol35] D. M. Wolkow: *Über eine Klasse von Lösungen der Diracschen Gleichung*, Z. Physik **94**, 250 (1935).

[WX14] Y.-B. Wu and S.-S. Xue: *Nonlinear Breit-Wheeler process in the collision of a photon with two plane waves*, Phys. Rev. D **90**, 013009 (2014).

[XCE] For current information, see http://www.xcels.iapras.ru.

[Zak05] S. Zakowicz: *Square-integrable wave packets from the Volkov solutions*, J. Math. Phys. **46**, 032304 (2005).